Jet Measurements at the LHC with the TRD-Trigger in ALICE

Jet Messungen am LHC mit dem TRD-Trigger in ALICE

Christopher Rittmeier

Westhusen 8, 59073 Hamm; Matrikelnummer: 343053

Masterarbeit im Rahmen des MSc Physik

Westfälische Wilhelms-Universität Münster

Institut für Kern- und Teilchenphysik

Themensteller: PD Dr. Christian Klein-Bösing

zweiter Gutachter: Prof. Dr. Anton Andronic

20th of december 2018

Contents

1 Theoretical background

The Standard Model (SM) of particle physics is a theoretical model which describes the elementary particles. These elementary particles are given in the following table (cf. [Gri10]):

		family I	family II	family III	electric charge
Fermions	Leptons	$\begin{pmatrix} e \\ \nu_e \end{pmatrix}$	$\begin{pmatrix} \mu \\ \nu_\mu \end{pmatrix}$	$\begin{pmatrix} \tau \\ \nu_\tau \end{pmatrix}$	$\begin{pmatrix} +1 \\ 0 \end{pmatrix}$
	Quarks	$\begin{pmatrix} u \\ d \end{pmatrix}$	$\begin{pmatrix} c \\ s \end{pmatrix}$	$\begin{pmatrix} t \\ b \end{pmatrix}$	$\begin{pmatrix} +\frac{2}{3} \\ -\frac{1}{3} \end{pmatrix}$

Gauge Bosons	electroweak interaction	W^{+-}, Z^0, γ
	strong interaction	$g_1, ..., g_8$ (Gluons)
and		H (Higgs-Boson)

The quarks and the massless gluons carry colour charge. The possible states of the colour charge are labeled with red, green, blue or its respective anticolour. Up to today there is no single free quark or other colour charged object measured directly. Only colour neutral objects like baryons, containing three valence quarks carrying each colour once, or mesons, consisting of two valence quarks, where one carries a colour and the other its anitcolour, could be observed up to today. This phenomenon is called confinement. It results from the fact that gluons, the mediators of the strong interaction, in contrast to the photons, the mediators of the electromagnetic force, carry charge itself. In fact the Quantum Chormodynamics (QCD) potential compared to the electromagnetic is very similar:

$$V_{QCD} = -\frac{4}{3}\frac{\alpha_s \hbar c}{r} + kr \tag{1.0.1}$$

$$V_{EM} = -\frac{\alpha \hbar c}{r} \tag{1.0.2}$$

whereby α and α_s are the respective coupling constants, cf. [Gri10]. Apart from a constant factor in the first term the QCD potential only differs from the electromagnetic one through an additional linear term. This term appears due to the mentioned selfinteraction of the gluons. Whereas in QED in vacuum there appear virtual electron positron pairs and thus the vacuum itself acts like a dielectricum and screens two charged point particles from each other. In QCD an anti-screening effect occurs since next to quark anti-quark pairs, screening the original particles, also gluon-gluon interaction appears which causes an increase of the coupling due to their self-interaction.

Consequently, the QCD potential diverges for increasing distance r.

1.1 The bag model and a quick estimate of the critical temperature for the QGP

One current area of research that is expected to enlight the understanding of the particle physics are the properties of the Quark-Gluon Plasma (QGP). The QGP is a state of matter that existed in the very early universe around 10^{-5} s after the Big Bang and still today is expected in superdense stars like neutron and quark stars. The QGP is a state of matter that consists of deconfined quarks and gluons. This state can be reached in a super hot and/or dense environment (see fig. 1).
For that, one can imagine that in a hotter becoming environment more and more hadrons are thermally excited from the vacuum. Now from a critical temperature T_C on the hadrons of a certain diameter of about 1 fm begin to overlap and dissolve in a soup of quarks and gluons. Analogously, one can reach the QGP state through compressing matter till a critical density of several times the normal one is reached. In figure 1 there is depicted the phase diagram of the QGP. The baryon chemical potential μ_B is a measure for the baryonic density. The potential of normal baryonic matter is about 0.93 GeV[1] and corresponds to the proton/neutron mass times c^2. To estimate the critical temperature T_C first the bag model shall be quickly introduced. With its help one can easily estimate T_C.

The bag model (cf. [Won94]) describes colour neutral objects as a bag with radius R in which quantum chromodynamics can be described pertubatively. Now the bag constant B is introduced which gives a quantitiy for the energy which is necessary to create a pertubative environment embedded in a non-pertubative vacuum. The following equation

$$E = \frac{2.04N}{R} + \frac{4\pi R^3}{3} B \tag{1.1.1}$$

gives a rough estimate for the total energy of a bag. B then has the the size of energy per volume which also can be interpreted as pressure. The first term gives the kinetic energy, where N is the number of quarks. The energetic most favourable radius can be calculated via $dE/dR = 0$, so one gets

$$\frac{dE}{dR} = -\frac{2.04N}{R^2} + 4\pi R^2 B = 0 \Leftrightarrow B^4 = \frac{2,04N}{4\pi} \frac{1}{R^4}. \tag{1.1.2}$$

[1] In this thesis is $\hbar = c = k_B = 1$.

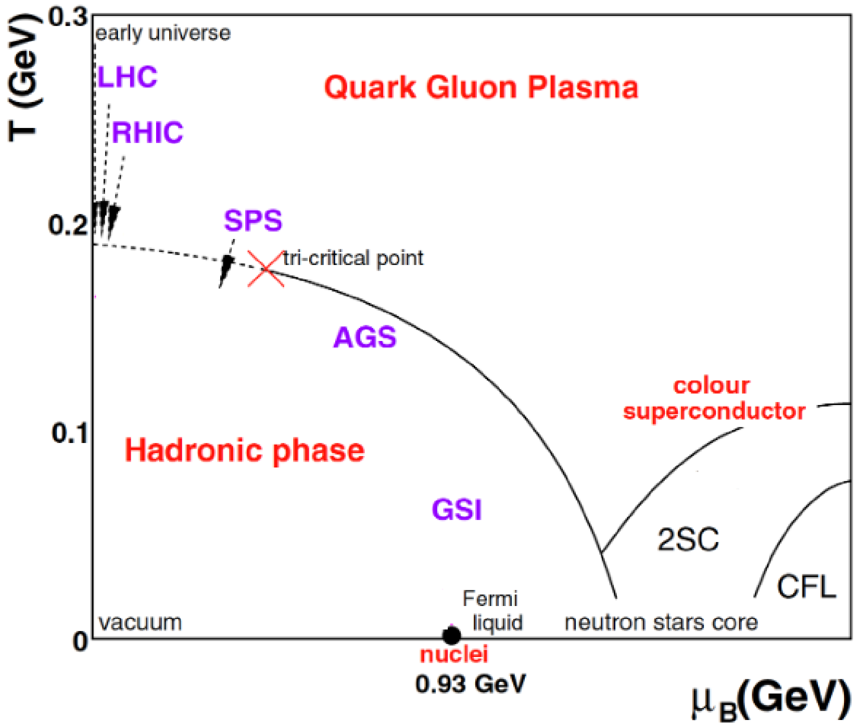

Figure 1: Schematic phase diagram in terms of the temperature T and baryon-chemical potential μ_B; as well areas some colliders reach are depicted. [PŠ17]

For R we can take a confinement radius of 0.8 fm for a 3 quark system so we get

$$B = (206\,\text{MeV})^4. \tag{1.1.3}$$

One can imagine now a spherical bag which confines the quarks and gluons. B gives the potential difference between the vacuum and its bag. The potential acts as an insurmountable obstacle for the quarks to leave the bag. The more the temperature increases the lower is the obstacle for the quarks and gluons to leave the bag. As soon as the obstacle disappears the particles are free. From statistical physics one can derive an equation for the energy density of the quark-gluon-matter which is given as

$$\epsilon = g_{tot}\frac{\pi^2}{30}T^4 \tag{1.1.4}$$

with $g_{tot} = g_g + \frac{7}{8}(g_q + g_{\bar{q}})$. g_g, g_q nad $g_{\bar{q}}$ are the degeneracy numbers of gluons, quarks and antiquarks. Since there are 8 gluons with two spin polarizations one obtains $g_g = 8 \cdot 2 = 16$.
Now if one takes two quark flavours into account consider that three colour charges and two spin states are possible one obtains $g_q = g_{\bar{q}} = 3 \cdot 2 \cdot 2 = 12$. The factor $\frac{7}{8}$

appears because fermi-dirac statistic has to be applied for fermions. So one gets

$$g_{tot} = g_g + \frac{7}{8}(g_q + g_{\bar{q}}) = 16 + \frac{7}{8} \cdot 2 \cdot 12 = 37. \tag{1.1.5}$$

Now one can calculate the critical temperature T_C. In this case the energy density of the quark-gluon matter must be equal to that one of the bag. So the condition is

$$3 \cdot B = 37 \frac{\pi^2}{30} T_C^4 \Leftrightarrow T_C = \left(\frac{90}{\pi^2} \frac{B}{g_{tot}} \right)^{\frac{1}{4}}. \tag{1.1.6}$$

The factor 3 originates from the fact that B is a quantity for the pressure and the energy pressure relation of massles fermion and boson gas is $P = \frac{1}{3}\frac{E}{V}$. With 1.1.3 and 1.1.5 one obtains

$$T_C = 145\, MeV. \tag{1.1.7}$$

1.2 QGP in heavy-ion collisions

1.2.1 Basics of heavy-ion collisions

The LHC at the European Organization for Nuclear Research (CERN) laboratory is able to accelerate ions, small ones such like protons till large ones like lead nuclei. Also the LHC accelerator able to reach energies up to 7 TeV per nucleon. During the collision of two ions nucleons are decelerated. The energy loss of the colliding particles is called nuclear stopping power and especially for large nucleons also dependent on the overlap region of the nuclei. In such high energy collisions like they happen at the LHC the nuclei are highly Lorentz contracted in the longitudinal direction and can be assumed as infinitely thin discs. Directly after the collision energy is deposited around the collision point and can be transformed in other degrees of freedom like new particles. The evolution of the medium around the collision point will be shortly discussed later. As a measure of the longitudinal momentum along the beam axis z the quantities rapidity and pseudorapidity are used.

The rapidity y is given through the equation

$$y = \frac{1}{2} \ln \frac{E + p_z}{E - p_z}, \tag{1.2.1}$$

where p_z is the momentum in beam direction and E the total energy of the particle. Since $E = \gamma m$ and $p = \gamma \beta m$ one gets an alternative equal expression for the rapidity to

$$y = \frac{1}{2} \ln \frac{1 + \beta}{1 - \beta}. \tag{1.2.2}$$

Now the particle velocity v is the only not constant expression. So the rapidity can be interpreted as a dimensionless quantity for the particle velocity. Another quantity, easier to measure is the pseudorapidity.

The pseudorapidity is defined as

$$\eta = -\ln \tan \frac{\theta}{2}, \tag{1.2.3}$$

where θ is the angle between the particle direction an the beam axis. In a two dimensional space where p_z is the particle momentum in beam direction and $|p|$ the total momentum, one gets $\cos(\theta) = \frac{p_z}{|p|}$. Besides applying the addition theorem $\cos(\theta) = \frac{1-\tan(\theta/2)}{1+\tan(\theta/2)}$ one comes to the alternative expression for the pseudorapidity

$$\eta = \frac{1}{2} \ln \frac{|p| + p_z}{|p| - p_z}. \tag{1.2.4}$$

Considering that $|p| = \gamma\beta m$ and for very high velocities ($E \gg m$) β tends to unity one gets the relation $E \approx |p|$ and herewith also $\eta \approx y$, compare equation 1.2.1. The pseudorapidity is so attractive since only the angle has to be determined, as it follows from equation 1.2.3.

The particle distribution after a collision is measured in dependence of the (pseudo-)rapidity for instance. An example of the net proton distribution for several accelerators is given in fig. 2. One can easily see that the distributions broadens and flattens for higher energies. Apart from that the peak shape with its only peak at mid-rapidity in the lowest energy case turns for higher energies into a double peak shape symmetric to the mid-rapidity-axis with its peak positions drifting apart. This phenomen is interpreted as a processing of becoming transparent. For lower energy collisions the stopping and its regarded energy loss is described by the Fermi-Landau model [Sle95]. This model assumes that the nucleons stopped completely. But with further increase of the kinetic energy, the energy loss of the traversing nuclei becomes too low to absorb all the particles kinetic energy. So they punch throug their opponents still carrying (large) kinetic energy and the opponent nuclei appear to become transparent. That also means that the Fermi-Landau model loses its validity since the preconditions are not fulfiled anymore.

The latter scenario was essentially described by Dean McLerran and James Bjorken and is thus called the Bjorken-McLerran model, cf. [Sle95]. It is based on the parton model, which means that nucleons are not only formed of its three valence quarks, but also sea-quarks and gluons are part of the nucleon which are finally responsible for the major part of the nucleon mass and for the binding of the valence quarks. In this model the energy of the colliding is deposited in a zone around the collision point (cf.

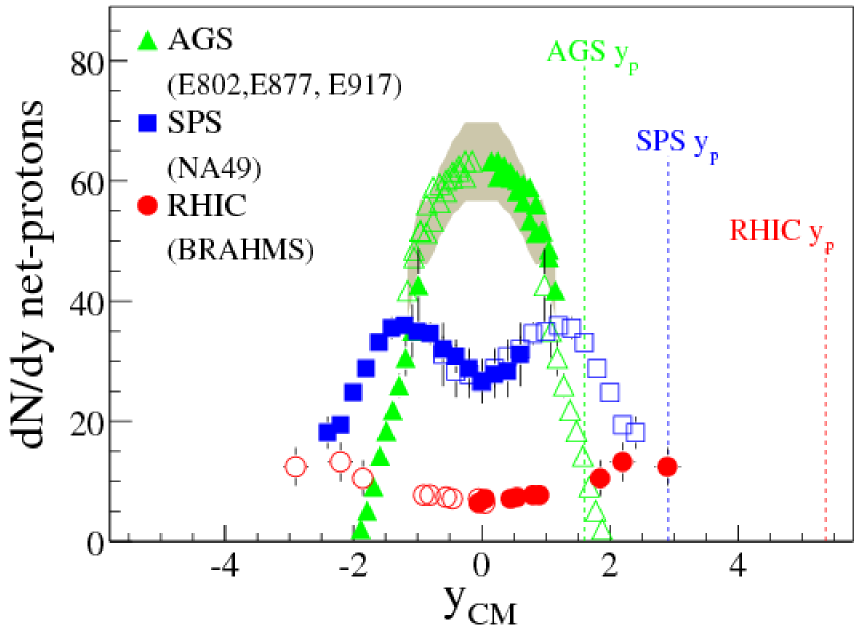

Figure 2: Net proton rapidity distribution at AGS($\sqrt{s} = 5GeV$, Au+Au), at SPS ($\sqrt{s} = 17GeV$, Pb+Pb) and at RHIC ($\sqrt{s} = 200GeV$, Au+Au) [Bea04].

Figure 3: Two nuclei approach each other with ultrarelavistic velocity, punching through each other and leave highly excited matter behind after the collision [YHM05].

fig.3) and also the creation of matter takes place there while the incident particles still might have enough energy to proceed. In this zone several states of matter might be undergone, one of them, the Quark-Gluon Plasma state, might be formed.

1.2.2 Space-Time evolution of a collision

Assuming the collision takes place at certain point in time, labeled with $\tau = 0$. First the scattering of partons would lead to a production of more interacting particles. But these particles are not in thermal equilibrium yet. After a time of about $\tau_f = 1\,\mathrm{fm}$ after the collision the particle system is in thermal equilibrium, which implies the particles momenta are distributed according to the Boltzmann distribution. The system now might be in a state of deconfined matter, the quark-gluon plasma. The required energy densities are about 0,2-1 GeV/ fm^3 [CNRS17], [YHM05].

Now one expects the QGP to expand adiabatically and due to the expansion it will cool

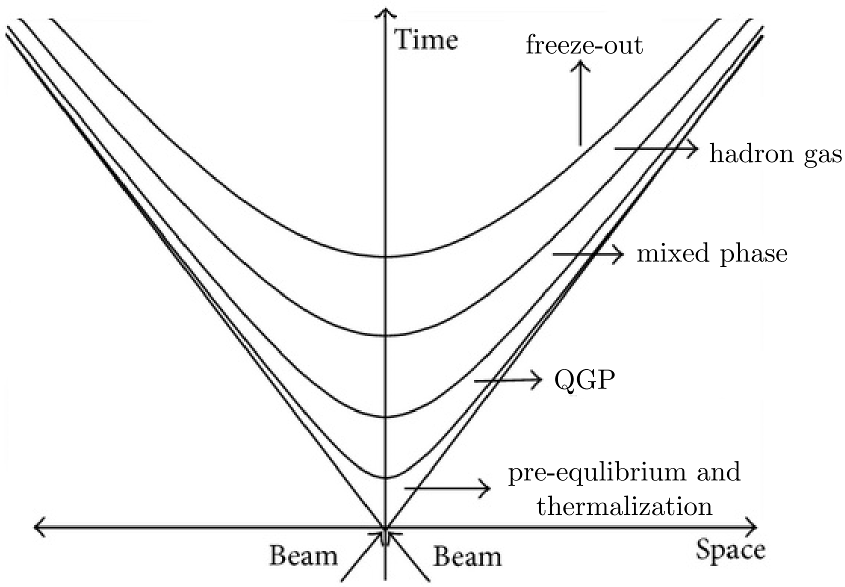

Figure 4: Light- cone diagram showing the space time evolution of an ultrarelavistic nucleus-nucleus collision.[Tiw]

down. Depending on the initial temperature the lifetime of the state might be between 1-10 fm. When the critical temperature $T_c \approx 150 - 200\,\mathrm{MeV}$ (cf. [YHM05]) is reached the system will turn into a mixed state where the quarks recombine to hadrons. Here the latent heat keeps the system on temperature so that the system expands isotherm. When the hadronization is completed, finally the hadrons keep interacting in a gas-like medium till the density of the matter system is low enough and the hadrons free path length is large enough to escape. Here the hadrons freeze out and evolve independently. Since the system behaves relativistically the proper time τ of each particle is Lorentz dilated, following the equation

$$\tau = \sqrt{t^2 - z^2}, \tag{1.2.5}$$

where t is the time in the laboratory system and z the distance to the collision point. Due to this effect particles in further regions undergo the above described evolution delayed. This effect is called inside-outside cascade and is finally the reason for the hyperbolic shape of figure 4.

2 Reconstructed jets and jet observables

2.1 Jets

An excellent phenomenon that occurs during scattering processes to probe the quark-gluon plasma are jets. During hard scattering processes high energetic partons are produced that fragment into a spray of particles. Though an unambiguous defintiton of a jet is difficult to formulate, their modification through the evolving medium on the shape of the jets is used as an indicator for the QGP. Essentially, jets are a collection of particles bearing away the momentum of the parent parton, when its daughter particles transverse matter they interact with it and so modify the jets shape.
With the appearence of quark-gluon plasma, a medium of free colour charges, also an increasing energy loss of transversing particles is expected, which is followed by a suppression of high momentum jets. This phenomenon is known as jet quenching. Besides this the jets itself are able to provide us with information of their mother particle. Further the influence of the traversed medium on the jets and the properties of the parent parton might influence the jet and its shapes.
In this thesis jets showing up in pp-collisions are investigated. In this collisions one does not expect the creation of a QGP state, but later on one can compare these jets with those of high energetic lead-lead collisions where such a state is expected and so derive informations regarding the QGP phase. One should consider that the measured constituents of the jet do not consist of partons anymore. They reach the detector as hadrons, final state particles that already passed the hadronization.
In this thesis the influence through the experimental realization of triggers on measurements, in particular on the jet shapes, shall be discussed in more detail. But before we come to the triggers itself. First the jet definition through the experimental set up shall be discussed and the jet shapes relevant in this thesis shall be presented.

2.2 The anti-k_t algorithm

Jet finder algorithms try to reconstruct the jets and consequently the properties of the mother particle through evaluating recorded particle signals. In this thesis the data contains information about particles, e.g. their particle track properties, theit charge, recorded by the ALICE detector at CERN, which will be presented in the next chapter. The anti-k_t jet finder algorithm tries to trace back the particle branching initiated by a parental particle. In the following the performance of this algorithm will be depicted.

1. For each particle i the geometrical closest particle V_i shall be calculated.
2. The particle with the smallest distance value d_{i,V_i} or $d_{i,B}$ may be identified, whereas
   (a)
   $$d_{i,j} = \min(p_{t,i}^{-2}, p_{t,j}^{-2}) \cdot \frac{\Delta_{i,j}}{R^2} \tag{2.2.1}$$
   with $\Delta_{i,j} = \sqrt{(\eta_i - \eta_j)^2 + (\phi_i - \phi_j)^2}$.
   Here R is a predefined constant and similar to a cone radius, but there might be jets annexing constituents with a larger distance than R.
   (b) $d_{i,B}$ is the distance to the beam axis and predefined as $d_{i,B} = p_{t,i}^{-2}$.
3. Now if
   (a) $d_{i,V_i} < d_{i,B}$ the two particles are combined to a single jet candidate/pseudo particle.
   (b) $d_{i,V_i} > d_{i,B}$ the particle is designed as jet candidate and removed from the list.
4. Continue with step 2 until all particles are removed. (cf. [Bat12])

The combination of the pseudorapidity η and the azimuthal angle ϕ of two (pseudo-) particles to a new pseudoparticle takes place under respect of those quantities weighted by their transversal momentum:

$$p_{t,p} = p_{t,i} + p_{t,j}, \tag{2.2.2}$$
$$y_p = \frac{p_{t,i}\eta_i + p_{t,j}\eta_j}{p_{t,i} + p_{t,j}}, \tag{2.2.3}$$
$$y_p = \frac{p_{t,i}\phi_i + p_{t,j}\phi_j}{p_{t,i} + p_{t,j}}. \tag{2.2.4}$$

2.2.1 Properties and general behaviour of the anti-k_t algorithm

With respect to equation 2.2.1 it becomes quickly obvious that first of all soft particles are added to hard particles, due to the inverse p_t weighting of the distance value $d_{i,j}$, which is for two soft particles always higher than for a combination of a soft and a hard one. Now one can assume an event with a lot of soft particles and few hard

ones. A hard particle in an environment of only soft particles will accumulate all soft particles at least within a radius of R to a conical jet through the anti-k$_t$ algorithm. The dominant hard particle often is also called seed particle.
If there's another hard particle within a distance interval of (R, 2R) there would be a set of soft particles that would come into account for both of them. But the distance value assignes the soft ones to only one of the hard particles, so that at least one of the two jets cannot be of conical shape.
If two hard particles are closer to each other than R, the defined jet axis is dominated by a pseudoparticle accordingly the equations 2.2.2, 2.2.3 and 2.2.4. Which is finally

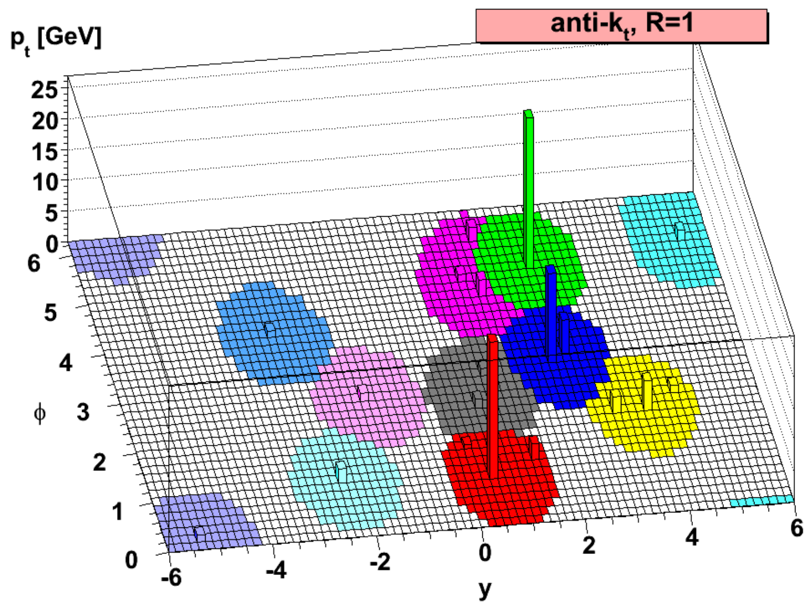

Figure 5: A sample parton-level event (generated with Herwig) illustrating the assigned areas of the resulting hard jets reconstructed by the anti-k$_t$ algorithm [Cac].

also the case like in the two mentioned cases before, with the difference that the hard particle first of all determines the jet axis since the weak soft particles have hardly influence on the hard one. In the latter case one speaks of a soft resilient jet algorithm, which is useful in case of a large background of other particles as in heavy-ion collisions.

2.3 Jet observables and jet shapes

Jets are mainly influenced by the mother particle and the traversed medium. Jet observables try to quantify the properties so that one can connect them to a cause. In this thesis morphological quantities, the jet shapes, are analyzed and so they are presented in the following subchapters.

Throughout this thesis there will be compared different jet shapes of different triggers and different jet transversal momentum ranges, so that the influence through the trigger on the shapes can be investigated.

2.3.1 Fragmentation function

The fragmentation function first of all assigns each jet constituent a number which is determined through the following equation:

$$\xi = \ln \frac{p_{T,\mathrm{Jet}}}{p_{T,\mathrm{Constituent}}}. \tag{2.3.1}$$

Here $p_{T,\mathrm{Jet}}$ is the total transversal momentum of the jet and $\mathrm{p}_{T,\mathrm{Constituent}}$ the one of single constituent belonging to the jet. So the shape and the position in the plot plane of the plotted sample gives us information wheather the jets preferably consist of few higher energetic particles or lots of particles with lower energy, cf.[CNRS17].

2.3.2 p_T dispersion

The p_T dispersion is defined as

$$p_{T\mathrm{Disp}} = \frac{\sqrt{\sum_i p_{T,i}^2}}{\sum_i p_{T,i}}. \tag{2.3.2}$$

Here the sum runs over all constituents of a single jet, which values are indexed with an i.

As the fragmentation function it depicts the soft-/hardness of jet. For fewer constituents in general it tends against one, for a lot of constituents against zero. But whereas the fragmentaion assigns every constituent a value, the p_t-dispersion does this once for the whole jet, cf.[CNRS17].

2.3.3 Radial momentum/girth

Another jet shape is the radial momentum or girth which depicts the p_t-weighted width of a jet.

$$g = \sum_i \frac{p_{T,i}}{p_{T,Jet}} \sqrt{(\eta_{\mathrm{Jet}} - \eta_i)^2 + (\phi_{\mathrm{Jet}} - \phi_i)^2} \tag{2.3.3}$$

Here the sum runs again over all constituents, whose values are indexed with an i. Jets with a high girth carry their p_t further from the jet axis compared to those of the same momentum but with a lower girth. Later one will see if higher energetic jets are statistically more collimated or broadened and how trigger conditions affect this behaviour, cf.[CNRS17].

3 Experimental access

So far there was discussed the physical background, now one can approach the experimental realization, beginning with the general experimental environment consisting of the accelerator LHC and its detectors. Then the focus will be put on the ALICE (A Large Ion Collider Experiment) detector with its transition radiation detector as one among 18 different detector types. This one is of special interest since it supports the data recording system with a trigger decision whose influence on recorded data shall be investigated in this thesis.

3.1 The Large Hadron Collider

The Large Hadron Collider (LHC) is located in the border region of France and Switzerland close to Geneva. It is a 27 km long accelerator ring which can create particle collisions up to a center of mass energie of 14 TeV by accelerating proton or lead ions in opposing directions. At each of the four crossing points of the opposing beams there is situated one of the four big experiments named A Torodial LHC Apparatus (ATLAS), Compact Muon Solenoid (CMS), Large Hadron Collider beauty (LHCb) and finally A Large Ion Collider Experiment (ALICE).

The luminosity can arise up to about $10^{34}\,\mathrm{cm}^{-2}\mathrm{s}^{-1}$. Therefore up to 2800 bunches can

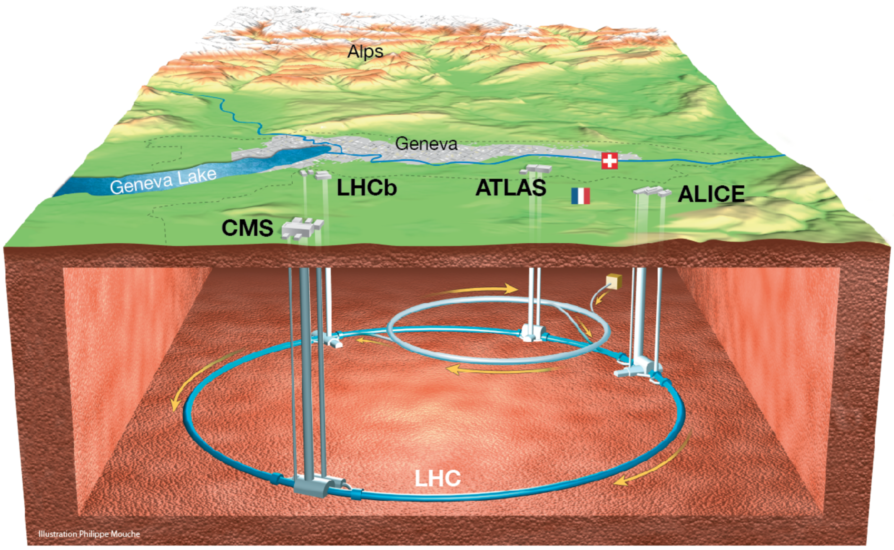

Figure 6: The scheme shows the four big experiments situted at the LHC ring in his regional environment. The pre-acceleration System is only represted by the final pre-accelerator SPS including its connection tunnnels[Mou14].

be arranged in one beam with each containing $1.15{\cdot}10^{11}$ protons. This gives a bunch

crossing rate up to 40 MHz.
On the 10th September 2008 began the comissioning of the LHC and sowith data of high energy collisions with increasing energies and luminosities was recorded. In 2009 and 2010 the accelerator provided the world with for example data of $\sqrt{s_{\text{Pb-Pb}}} = 2.76\,\text{TeV}$ and $\sqrt{s_{\text{P-P}}} = 7\,\text{TeV}$ collisions. In this thesis data of pp collision with an energy of $\sqrt{s_{\text{P-P}}} = 8\,\text{TeV}$, recorded in 2012, is investigated.

3.2 A Large Ion Collider Experiment – ALICE

The ALICE detector is the dedicated experiment for heavy-ion collisions. It is designed for excellent particle tracking over a wide momentum range from about tens of MeV/c up to around 100 GeV and highest multiplicity at midrange up to $\text{d}N/\text{d}\eta = 8000$ [ea08]. Therefore it is made of several subdetectors, each dedicated to an own region of interest. Looking at figure 7 one easily recognizes the central barrel detectors surrounded by the large L3 magnet in red and on its right side the muon arm. The relevant detectors for this thesis, the EMCal, TRD and the V0/T0 are all part of the central barrel detectors. These will be described in some more detail in the following.

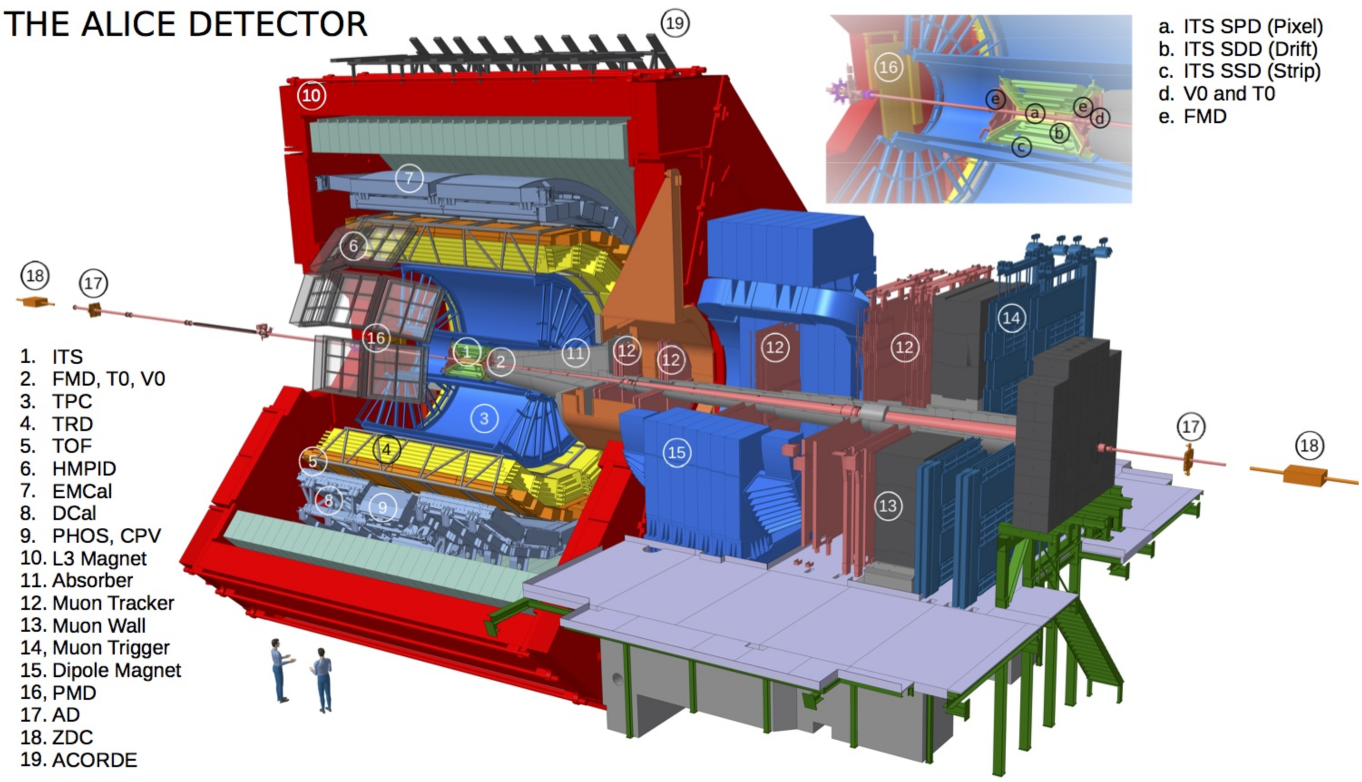

Figure 7: Schematic of ALICE with its subdetectors; In this thesis the investigated triggers are supported by the V0(2d), T0+A/+C (2e) two by EMCal(7) and TRD(16) which are surrounded by the L3 magnet(10).[Tau17].

3.2.1 The V0 and T0

The V0 detector is a scintillator in the small angle range covering -3.4< η <-1.7 and 1.7< η <5.0, very close to the beam line. There is on each side of the vertex a V0 situated, named V0A and V0C with a distance of 3.40m and 0.90m to the collision point. In the context of this thesis this detector serves as Mimimum Bias (MB) trigger. This trigger serves first of all to initiate data recording under the simplest conditions and will be described later in more detail. Due to high collision rates it might occur that the time resolution rate of the V0 is exhausted. In this case the T0 detector takes its place as MB [ea08].

The T0 detector is a Cherenkov detector consisting of 2 photomultiplier arrays, each with 12 counters, in the small angle region covering -2.9< η <-3.3 and 5< η <4.5. It has an excellent time resolution of 50 ps and a dead time of about 25 ns which should be below a bunch-crossing period. [ea08] But it is sensitive to merely half the cross section, the V0 is preferably used as MB trigger.

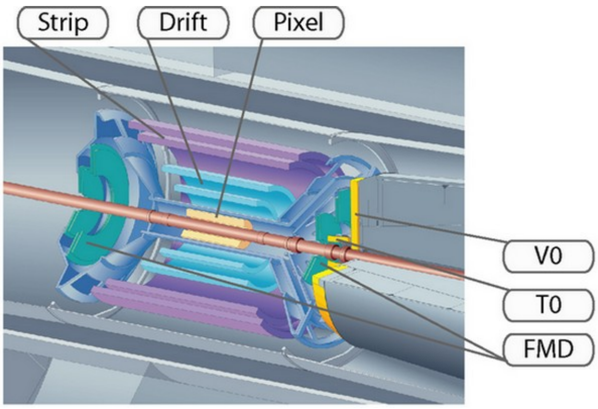

Figure 8: The schematic shows the ITS (Inner Tracking System) [Man12].

3.2.2 The electromagnetic calorimeter – EMCal

The EMCal detector is a large Pb-scintillator located adjacent to the L3 magnet. It covers $|\eta|$ <0.7 and $\Delta\phi = 107°$ with a distance of about 4.5m from the interaction point. It provides fast trigger and also is excellent for triggering jets. Further it is also able to measure neutral components of the jets. Later in this thesis EMCal triggered data is compared with TRD triggerd data.

3.3 The Transition Radiation Detector – TRD

The Transition Radiation Detector (TRD) is built for measuring charged particles with highest transversal momentum and supports an excellent electron-pion separation. It covers $|\eta| < 0.9$ in beam direction and full azimuth since 2015. For this purpose 522 multiwire proportional chambers, filled with $Xe/CO_2(85\%/15\%)$, are arranged.
Each chamber cf. 9 consists of a radiator and a drift chamber, which again can be separated in a drift and an amplification region. The electric field inside the chamber

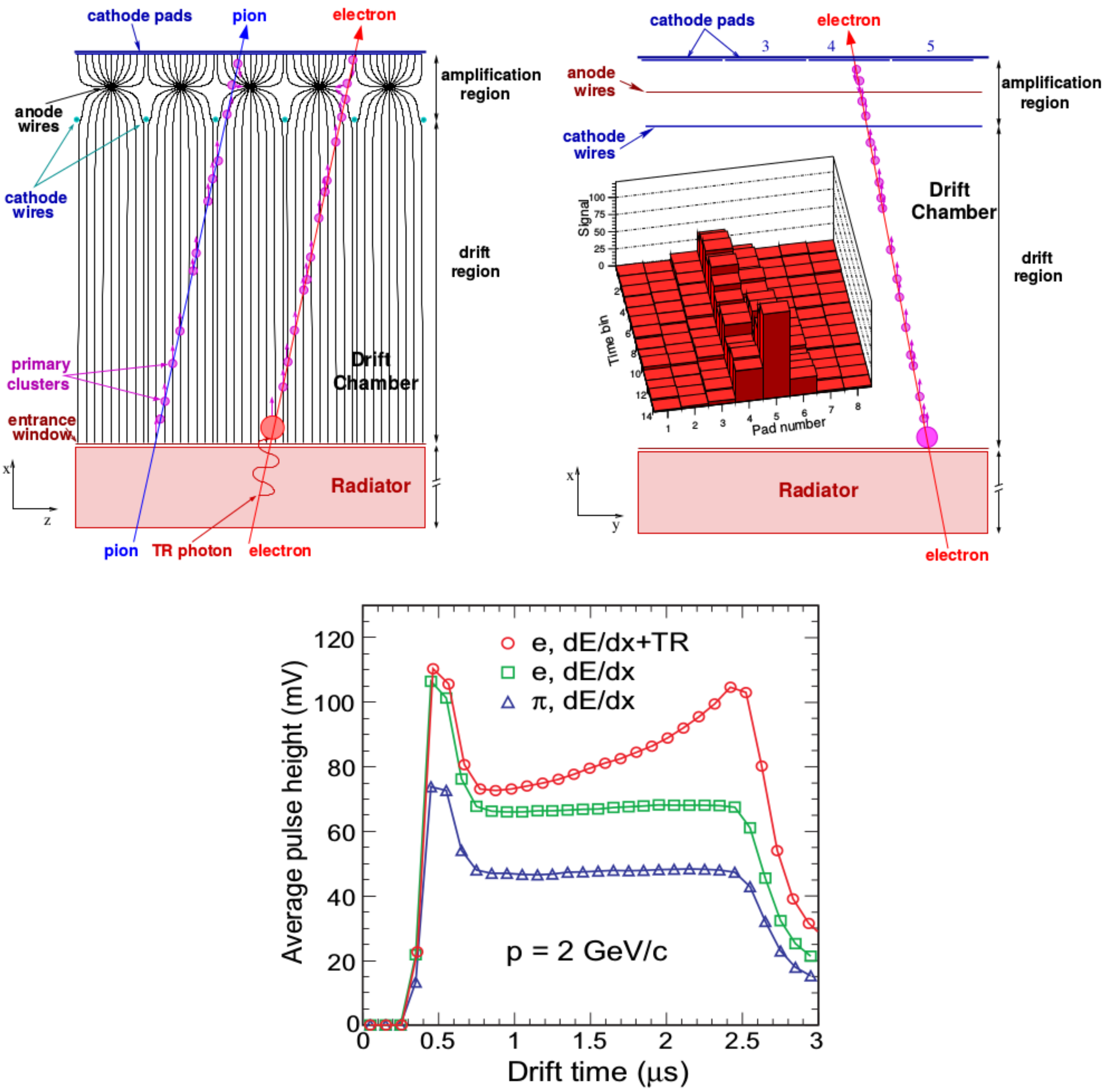

Figure 9: The top panels show a crossectional view on a drift chamber with a radiator underneath, in rz direction in the left and $r\phi$-direction on the right. The inset shows a charge deposit recorded over 14 time bins which is used for track reconstruction. The plot at the bottom shows the average pulse height as a function of drift time for pions, electrons without a radiator and electrons with a radiator for 2 GeV particles. [ea08].

is generated through an electrode directly glued upon the radiator and the cathode pads upon the drift chamber. Charged particles passing the radiator can create transition radiation for a γ-factor $\geq$1000. Charged particles passing the gas chamber then cause an avalanche of secondary electrons drifting towards the anode wires. Very close to the anode wires they are amplified and measured through mirror charge at the cathode pads.
The ALICE TRD is built first of all because of its excellent pion-electron separation. Since the γ-factor is the crucial criteria for the creation for the production of transition radiation, which is only dependent on the velocity of the particle, pions, due to their higher mass, need a much higher momentum than electrons. The transition radiation, in the case its generated, causes a tail peak in the signal, cf. figure 9.
But apart from this property the multi-wire proportional chamber can also be used for the tracking of any charged particle without particle identification.

All 522 chambers are arranged as seen in figure 10 in 18 super modules, each separated in 5 stacks with 6 layers of transition radiation chambers. On top of each chamber there is the readout electronics. It shall be mentioned that not all super modules were installed from the very beginning of the LHC operation time. Here data from 2012 is analyzed. At that time 13 super modules (00, 01, 02, 03, 06 07, 08, 09, 10, 11, 15, 16, 17) had been installed. During the long maintenance shut-down, starting end of 2014, the other modules were finally added.

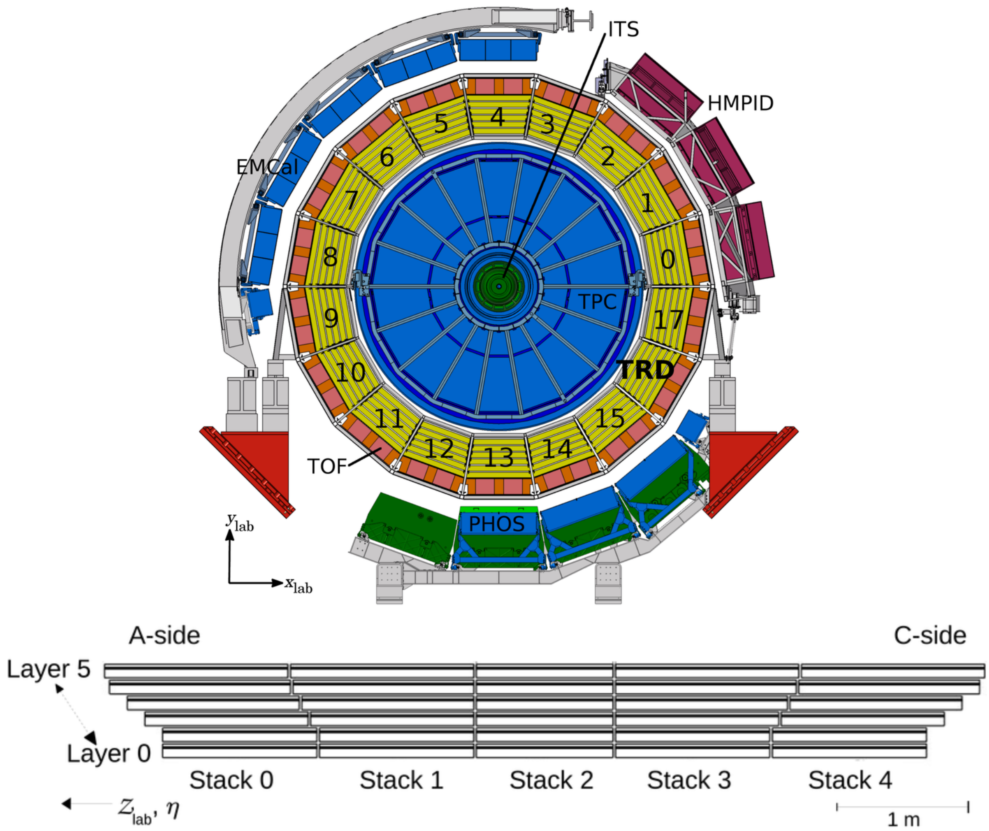

Figure 10: The schematic above shows a cross section of the ALICE detector perpendicular to the beam axis. The TRD in yellow is divided in 18 supermodules in azimuth and the six layers in radial direction are also visible. The scheme below shows a cross section of the supermodule in beam direction [A+18].

3.3.1 Signal and data processing

To fulfil the low latency requirements for trigger decisions readout electronics are mounted on top of each chamber to process the signals as fast as possible. Each of the 522 chambers is equipped with 96 or 128 Multi Chip Modul (MCM), depending on the type of chamber. In the MCM there is intergrated a Pre Amplifier and Shaper Amplifier (PASA) and a so called Tracklet Processor (TRAP) with 18 inputs each connected to one cathod pad. In the MCM the signal is amplified, converted into digits, needs to pass several filters and finally the tracklets (particle track in a single readout chamber) is calculated. Next to it the raw data is stored in an event buffer. Finally the data is sent via an network interface to one of the two Optical Readout Interface (ORI) on top of each chamber which are again linked to the Global Trigger Unit (GTU).
The GTU is located outside the L3 magnet and consists of several data processing units and a further data buffer. Here tracklets are combined to tracks. In case of a positive L2 trigger decision the data from the GTU is shipped directly to the Data Aquisition (DAQ) center, where a full event reconstruction and the final data storing takes place, cf. [Bat12], [ea08].

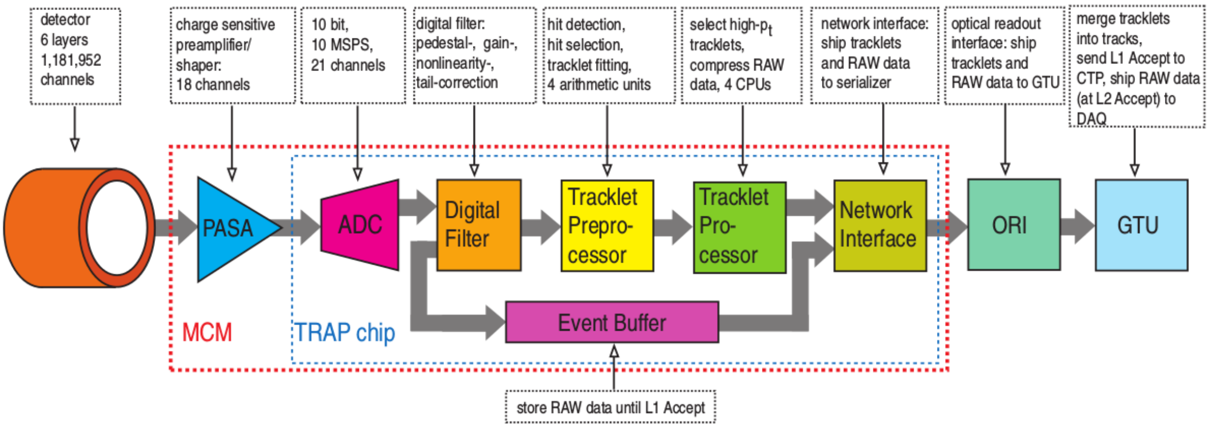

Figure 11: Schematic overview of the readout electronics of the TRD [ea08].

4 Triggering with the ALICE TRD

4.1 Trigger Systems – Motivations and Basics

By far not every collision provides an event of interest. Since the amount of data would explode in case every event would be recorded and also every event recording results in a dead time which makes the detector blind for possible interesting events, it is sensible ti to construct a mechanism which decides very quickly whether the event should be recorded or not. Thus trigger systems are added which generate such a decision mechanism.

Each trigger system is provided by a trigger detector and a Central Trigger Processor (CTP). The trigger detector can just be another detector next to the main/readout detector, which sends informations gathered through its measurements to the CTP. The CTP then decides if it sends a signal to the readout detector. The signal then can initiate two different reactions on the readout detecor. The first possible response would be that the readout detector wakes up from its resting modus and starts data recording. In case the readout detector does not need to wait for a wake up signal and is already recording data the response on the CTPs signal can cause a process which erases all data and prepares the detector for the next event or gives the order to send the recorded event data to the DAQ.

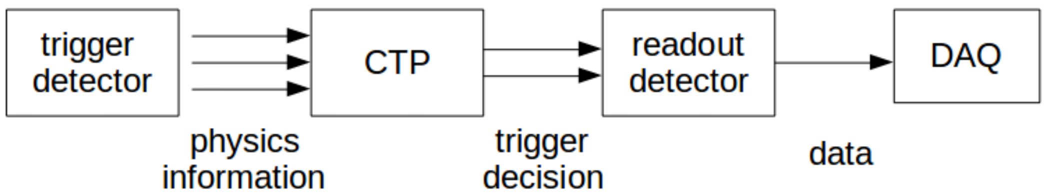

Figure 12: Scheme of a very basic trigger system.

Detector systems can consist of far more than two detectors. Data of trigger detectors can also be used for the analysis and information originating from measurements of readout detectors can again be used as trigger contributions for other readout detectors. In other words every detector can be readout and trigger detector at the same time.

4.2 ALICE TRD trigger system

As mentioned the ALICE detector is a system of subdetectors like the TRD for example, which is here first of all used as trigger detector but also can provide excellent pion-electron separation and in addition serves with its multi wire proportional chambers as a fast trigger detector. In this part a rough description about the ALICE trigger system in general and the implementation of the TRD as contributing trigger detector

shall be given.
The ALICE detector system contains several detectors. The CTP provides the trigger decision logic. It receives detector signals and returns trigger decisions based on predefined triggers. There are four trigger levels (L0, L1, L2 and the HLT) implemented in the trigger system. Each of them requires several physics information. This information needs to be at the CTP within a given time interval after the collision. Vice versa the trigger decisions are expected as well at the detectors until a certain point of time after collision, cf. figure 13. If this is not the case, the signal is rated as negative and the detectors erase their data and prepare for the next collision.

Trigger-Level	L0	L1	L2	HLT
conditions on	multiplicity, centrality, bunchcrossing	resonances, jets	pile up	writes events/regions of interest on tape
contributed by	fastest detectors like V0, T0, SPD, TOF	TRD, EMCal, ...	TPC	carries out online full event building, physics analysis
signal at CTP [μs]	0.8	7.3	94	runs after complete detector readout
at detector [μs]	1.2	7.7	∼100	
recording rate [kHz]	100	2.5	1.5	includes compression of data, maximal outstream 1.25 GB/s, 10% of readout data

Figure 13: The four trigger level of the ALICE trigger system are shown. For conditions and contributions here are only some examples given. The HLT runs after the complete detector read out and does not affect the time of measurement, cf. [Kle13].

Further it shall be mentioned that the CTP has 60 inputs (L0: 24, L1: 24, L2: 12). In the braces are the number of inputs depending on the trigger level. Not every detector has an input in each trigger level. The inputs are connected to the Local Trigger Unit (LTU)s of each detector providing the CTP with signals. There can be defined up to 50 trigger classes in the CTP. Each class is a bundle of trigger decisions. Only if all trigger decisions belonging to one class are positive the belonging detectors are read out.

The TRD trigger system contains an additional pretrigger system which provides the TRD with a Wake-Up (WU) signal within 200 ns after the collision [Bat12]. It makes the TRD preparing for data recording by waking it up from a rest mode which proved to be necessary for heat reduction. The L0 decision in this case would simply be too slow for waking up the detector. The pretrigger receives its information directly from the V0/T0 detectors and its trigger signal should mimic the L0 as good

as possible, since a negative decision of the latter causes a data erase of the temporary recorded TRD data. The crucial difference between the CTP and the pretrigger is that the pretrigger is situated inside whereas the CTP is situated outside the L3 magnet and so a shorter cable length enables a faster decision.
In addition the pretrigger system provides the busy logic which protects the TRD from starting a new trigger sequence as long as the read out is going on. Therefore the GTU upholds a busy signal to the pretrigger as long as the FEE transfers data.

As mentioned in a previous chapter the LHC support a bunch crossing rate up to about 40 MHz. ALICE favours an excellent particle tracking system rather than a quick readout for large statistics. Furthermore the Time Projection Chamber (TPC) has a drift time of up to 88 μs which, following the previous table, corresponds to the L2 trigger level of about 1.5 kHz. An interaction rate too high would lead to an inextricable pile up of events. Therefore so called satellites are pasted between the main bunches with a lower amount of protons. Due to this reason the bunch luminosity is reduced to $L = 10^{30}\mathrm{cm}^{-2}s^{-1}$. Assuming an inelastic cross section of $\sigma = 80\,\mathrm{mB}$ [Bat12] this would lead to a minimum bias interaction rate of about

$$R = L \cdot \sigma \approx 80\,\mathrm{kHz} \tag{4.2.1}$$

4.3 Trigger – aims and quantities

Now it is time to define a decent trigger, which optimizes the use of delivered data. The readout rate of the TRD is actually about 1.4 kHz whereas the minimum bias rate is about 100 kHz. A perfect jet trigger is able to distinguish between jet events and not jet events. But actually it is not possible to reconstruct the jets via a jet finder algorithm to provide one of the mentioned trigger level. So one needs to rely on more basic quantities.

4.3.1 Efficiencies and the rejection factor R_F

The basic quantities that describe a trigger are the efficiency and the rejection factor.

The efficiency of a trigger ϵ_t gives the ratio between all triggered events (T) under the condition that it is an event of interest (I) compared to all interesting event.

$$\epsilon_t = \frac{T \cap I}{I} \tag{4.3.1}$$

In the case of a jet trigger one challenge is to determine trigger conditions pointing as reliable as possible on jet events of interest. This is first of all tested in simulations i.e. with PYTHIA. Here triggers are tested on simulated events and so their efficiency is

estimated.
Now one needs to take into account that a trigger, through its conditions, might influence quantities of interest like the already introduced jet shapes. Any irregularity in the trigger efficiency of a variable introduces a bias, which will be shown later in this thesis.

The other mentioned quantity is the rejection factor R_F. For jet events the rejection factor gives the ratio of all jets per triggered event to all jets per randomly recorded event. Finally it can be probed on real data, as it will be done here later.
For the calculation of R_F then so called minimum bias data is taken as randomly recorded data. The equation for the rejection factor then is given to

$$R_F = \frac{1}{N^{HJT}_{events}} \frac{dN^{HJT}_{jet}}{dp^{T,HJT}_{jet}} \Bigg/ \frac{1}{N^{MB}_{events}} \frac{dN^{MB}_{jet}}{dp^{MB}_{T,jet}}, \tag{4.3.2}$$

where the upper index MB refers to minimum bias triggered data and the upper High Jet Trigger (HJT) to triggered data of the jet-trigger which will be presented in the following. But both of them also can be replaced by any others.
The minimum bias trigger has the simplest condition on any event. Here its signal is already positive when a coincidence signal is registered on both sides of V0 or T0 [BEJ+10],[Teab]
Now as the focus of this thesis lies on the HJT a dedicated chapter will follow.

4.3.2 HJT – a level 1 trigger

For the L1 trigger level the GTU of the ALICE already gives access to reconstructed tracks. This opens the ability to put conditions on a minimum number of tracks N_{trk}^{min} beyond a given p_T threshold $\mathrm{p}_t^{\mathrm{min}}$, which already has been investigated in the frame of several theses cf. [Bat12], [Kle14]. Figure 14 shows the number of constituent tracks exceeding 3 GeV in a jet. Here a real data set of 8 TeV pp collisions has been analyzed. One can see that only a very minor part shows less than three tracks beyond 3 GeV per track, apart from the low energy region which is anyway not of interest for triggering on high-p_t-jets. Finally a jet trigger requiring three particles exceeding 3 GeV was taking and henceforth will be labeld with HJT for high jet trigger.
In figure 15 there is a plot giving the efficiency of the HJT depending in the jet-p_t. First of all one can clearly see that the chosen $\mathrm{N}_{\mathrm{trk}}^{\mathrm{min}}$ beyond a $\mathrm{p}_t^{\mathrm{min}}$ are suppressing low p_t-jets in favour of high p_t-jets. Now if the trigger efficiency for two trigger reaches a constant value, as for example in figure 15 for the TRD, then there is also a plateau expected in the rejection factor. This will be investigated in a later chapter.

Finally there will be compared three sets of data each passing one of three triggers.

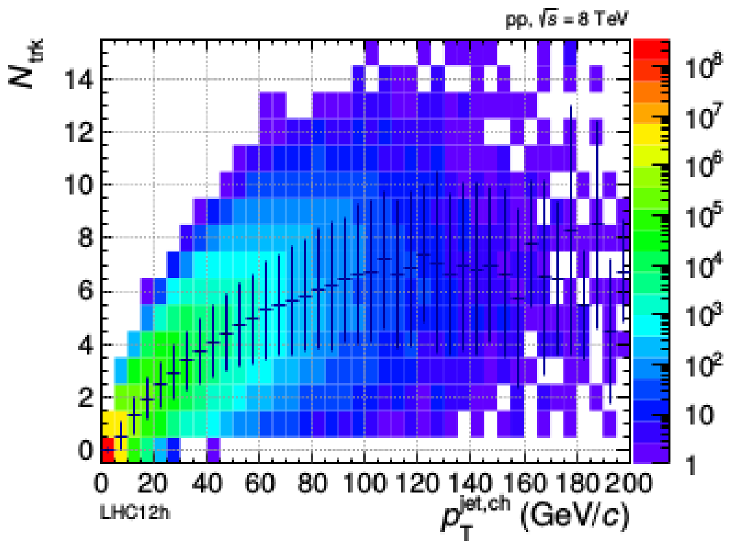

Figure 14: In this plot are shown the number of jets with N_{trk} constituents with $p_t \geq 3\,\text{GeV}$. The markers show the mean and spread in a given p_t bin.[Kle14]

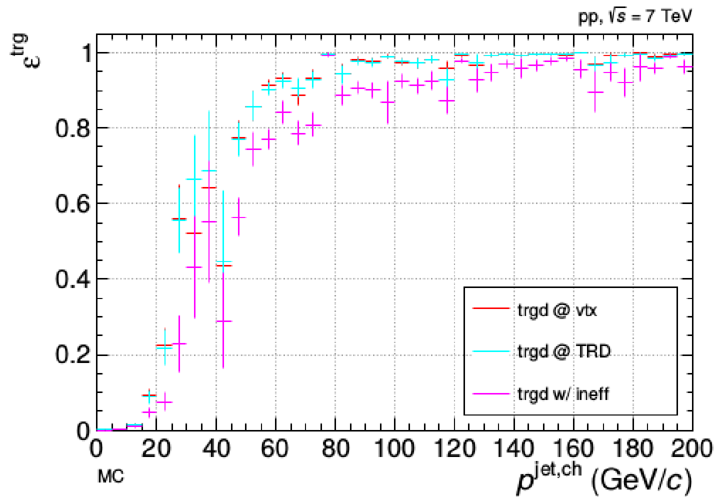

Figure 15: Pythia simulation of trigger effeciency of charged jets with three constituents with $p_t \geq 3\,\text{GeV}$ passing any window correspondending the stack size of the TRD in η-φ-plane. @vtx for tracks properties evaluated at vertex, @TRD for tracks evaluated at the inner TRD radius and w/ ineff for an assumed 80% tracking efficiency.[Kle14]

One of them is the MB trigger and the other two are jet triggers. One of the latter two is the already discussed HJT and the other one the EMCal Jet Trigger (EJE). EJE data sets will first of all serve as a comparison for high p_t-jets with the HJT since the MB trigger will not deliver sufficient statistics there, as one will see later. The EMCal Jet trigger EJE thereby sums energies within a sliding window of 32x32 EMCal towers corresponding to $\Delta\eta \times \Delta\varphi \approx 0.46 \times 0.46$, cf. [A+14].

4.4 Trigger classes

In this thesis triggered data of chosen trigger classes is analyzed. The CINT7/8 trigger conditions are representive for the used MB condition, whereas the dedicated detector for the CINT7 trigger is the V0 and the one for CINT8 trigger ist the T0, cf. chapter 3.2.1.

Since the L0 trigger arrives too late at the TRD a dedicated pretrigger system is installed inside the L3 magnet. It receives the signals directly from the V0/T0 and tries to mimic the L0 trigger condition from above as good as possible. The efficiency for the pretrigger system mimicing the L0 is beyond 97%, cf. [A+18]. In the following a positive pretrigger is labeled with WU for wake up.

Trigger classes can contain a pretty pile-up of different triggers. They are predefined. As soon as a trigger class is positive, the data readout of selected subdetectors is initiated and the read out events are labeled with the positive trigger classes. The naming scheme of the classes is so arranged that the contributing trigger can be derived. The general form of the naming scheme and an example is given in figure 16. The

$$\boxed{\text{descriptor} - \text{bunch crossing mask} - \text{past-future protection scheme} - \text{detector cluster}}$$

$$\text{CINT7WUHJT} - \text{S} - \text{NOPF} - \text{CENT}$$

Figure 16: General naming scheme of the trigger classes (framed) with an example below.

containing elements of a trigger class name are:

The descriptor is a logical function of trigger inputs. In the example of figure 16 it is CINT7WUHJT. Here three already meantioned triggers are combined:
1) the minimum bias trigger CINT7;
2) the WU for a positive wake up signal;
3) the HJT is positiv which was already discussed in more detail in chapter 4.3.2.
For the readout of only MB triggered data the WU and HJT trigger would not be of interest. A corresponding class just without WUHJT is therefore defined. Consequently every event labeled with CINT7WUHJT – S – NOPF – CENT is also labeled with CINT7 – S – NOPF – CENT. CINT7 also might be replaced by CINT8.

The bunch crossing mask is giving the type of bunch crossing. They are labeled with a letter or a series connection of letters. Possible types are:
1) B for beam-beam interaction: two filled bunches were crossing;
2) S for main-satellite: a filled bunch and a satellite, a bunch of a reduced number of protons were crossing. The satellites are fed in the ring for reducing pile-up for the ALICE detector.
3) ACE is a group of possible BC . Here A/C means a beam from A/C-Side and E for no beam from either side. Usually collisions with rest gas happen in this cases. These can be used for studying background. Here BCs of type S are analyzed.

The past-future protection scheme describes if the past future protection against pile-up is activated for the class. This is of special importance for the TPC, since an unresolvable pile-up of many collisions might make it impossible for the TPC to trace back the tracks to a certain collision. The class here is out of any importance for this analysis and henceforth is put as NOPF for no past-future protection.

The detector cluster gives a group of subdetectors which is readout for this event. The groups are relevant for this analysis are:
– ALL for all detectors
– CENT for the central barrel detectors, without i.e. the muon arm
– (any before +)NOTRD.

The latter one is of interest since any event fireing the HJT trigger also would do so with the minimum bias trigger as already said. For this thesis it is important to know that in case of a +NOTRD class there is no specific jet trigger defined, so the investigated trigger condition for the data readout here is the CINT7 condition whereas in the HJT case the for the data readout crucial condition is CINT7WUHJT, not the CINT7 condition though it is still active since it is a precondition for the TRDs data taking. One needs to take into account here that it is arranged that both trigger work on separated time intervals so that compulsory dead times or trigger conditons do not interfere in favour of one of the triggers respectively.
The here used trigger classes are:

- Minimum Bias: CINT7-S-NOPF-ALLNOTRD, CINT8-S-NOPF-ALLNOTRD
- TRD High Jet Trigger: CINT7WUHJT-S-NOPF-ALL, CINT8WUHJT-S-NOPF-ALL, CINT7WUHJT-S-NOPF-CENT, CINT8WUHJT-S-NOPF-CENT
- EMCal Jet trigger: CEMC7EJE-S-NOPF-CENTNOTRD, CEMC8EJE-S-NOPF-CENTNOTRD, CEMC7WUEJE-S-NOPF-CENT, CEMC8WUEJE-S-NOPF-CENT

Here appear two not yet mentioned acronyms. One is the EJE, a L1 jet trigger. Appearing in a trigger class it verfies a positiv EMCal jet trigger as described previously. The other ones are the CEMC7, CEMC8. They are EMCal L0-triggers together with a coincidence in the T0 or V0. Whereas again the 7 refers to the V0 and the 8 to the T0.

5 Data processing and selection

The here used analysis framework AliRoot is supported by the ALICE collaboration based on Root, a data processing computer program that is developed for big data processing, statistical analysis, visualization and data storaging [Teac]. In addition it provides libraries for PYTHIA, a simulation for particle collisions, which also was applied in the context of this thesis. Finally, for jet analyses, the jet finder "FastJet 3.2.1" which also supports the anti-kt jet-finder algorithm is implemented.
The recorded and here analyzed data usually is available as Event Summary Data (ESD) or Analysis Object Data (AOD) files. AODs are filtered ESD files with already applied track cuts and so contain less information. This data type contains all necessary information and therefore is used. For the jet analysis tracks of high quality are necessary. So those tracks which passed the so called hybrid track selection are used. Hybrid tracks contain two types of tracks:

- good global tracks with ITS refit and hit(s) in the SPD
- global constrained tracks with SPD hit(s) (without ITS refit) that can be constrained to the primary vertex

More detailed information is given on [Teaa]. In addition only tracks with $p_t^{\mathrm{track}}>0.15\,\mathrm{GeV}$ were committed to the jetfinder software.
The major data acquisition of HJT triggered data of 8 TeV proton-proton collisions was made during the LHC12f, LHC12h and LHC12i run periods. The analyzed run numbers are given in appendix A. In order to check the general quality of the data on this list an additional run number selection was applied. For this purpose the average particle p_t of each run number was calculated and compared with all others of the same run period. The first step was to discard the run numbers with an obviously too far alternating p_t from the average $\mathrm{p}_{t,av}$. This first manual selection was made to reduce its influence on the following selction algorithm, which worked as follows:

1. a straight line s(run_number)=c_{fit} was fitted to the remaing run numbers average $\mathrm{p}_{t,av}$, where $\mathrm{c}_{\mathrm{fit}}$ is a constant
2. all run numbers were discarded with $\mathrm{p}_{t,av} \notin [c_{\mathrm{fit}} - 0.05, c_{\mathrm{fit}} + 0.05]\,\mathrm{GeV}$
3. the first two steps were repeated but all run numbers with $\mathrm{p}_{t,av} \notin [c_{\mathrm{fit}} - 0.03, c_{\mathrm{fit}} + 0.03]\,\mathrm{GeV}$ were discarded

In figure 17 such an example is given. This procedure has been independently applied for events with a positive HJT, positive EJE trigger and a positive MB trigger. In the following the p_t-spectra of the run different periods of each so chosen trigger sample will be compared and differences between them will be investigated, to ensure a jet analysis as good as possible.

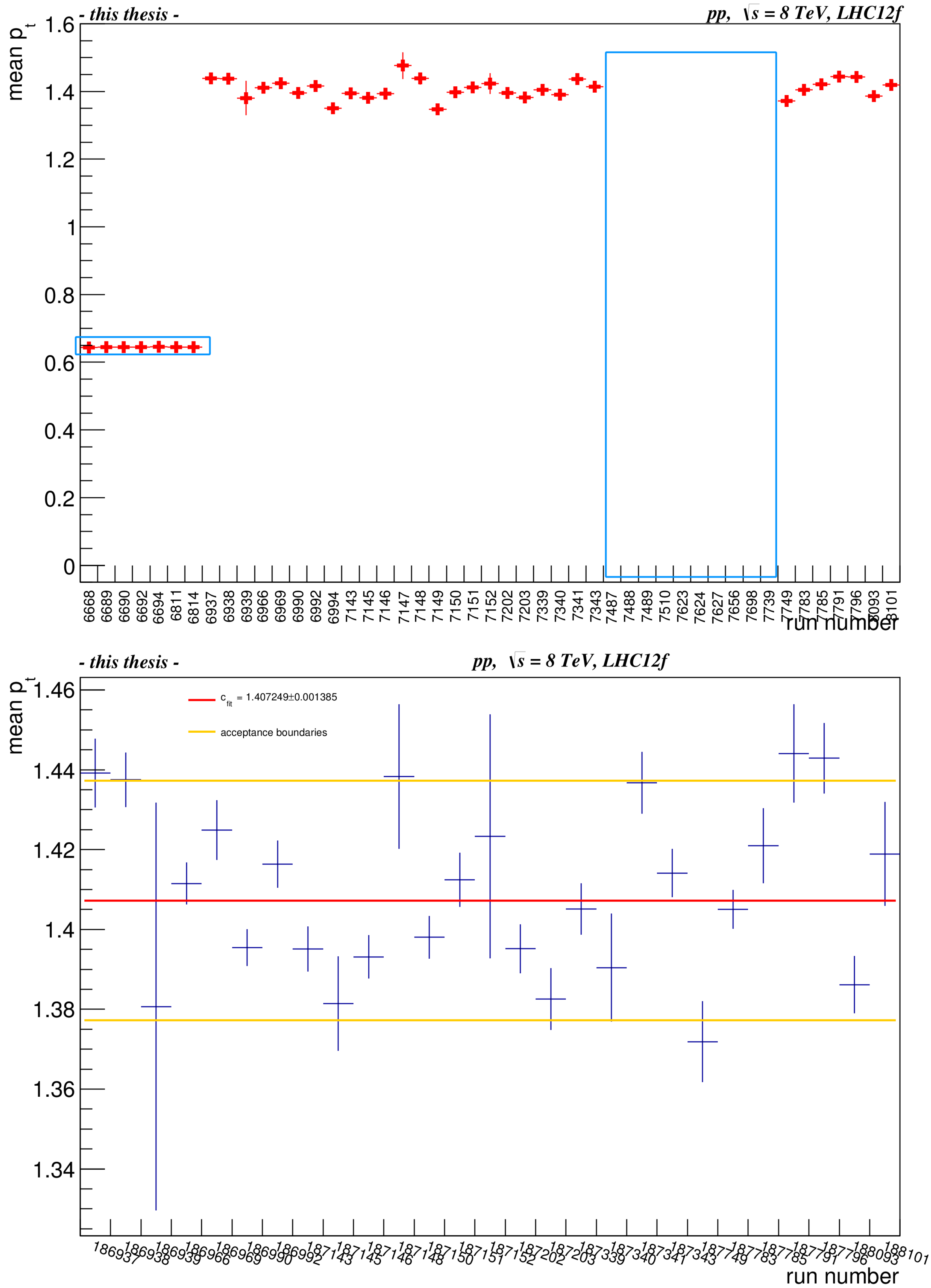

Figure 17: (top) the mean p_t for each run number after the hybrid track selection, whereas only the last four number are depicted, the first two are always 1, 8. The run numbers in the first blue box were manually discarded, since they would influence the algorithm in a way that only two number would have been left. (bottom) The run numbers that passed the selection algorithm. The red line gives the mean p_t the yellow one the correspond to the mean $p_t \pm 0.03\,\mathrm{GeV}$.

6 Trigger performances

6.1 Trigger Performance

In this chapter jet spectra shall be investigated and the rejection factor as a quantity for the trigger performance shall be calculated. Further it is important to locate a region where jet data finally does not have any more visible trigger induced biases. To ensure this it is necessary to compare triggered data with minimum bias data. From a given jet-p_t-momentum on the three investigated data sets should not show a visible difference anymore. For this purpose jets with a transverse momentum 10 GeV and more are examined. The aim of the HJT trigger is to select events with jets of highest p_t. It is important that a transition from biased TRD data to unbiased one from a given momentum on takes place.

The here investigated jets with the parameter R, which already showed up in the anti-kt algorithm (cf. 2.2.1), was chosen to R=0.4 and consequently the maximal pseudorapidity η of a jet is chosen to 0.5 since otherwise the reconstructed jet would exceed the physical borders of the detector and so influence the jet properties due to different input conditions.

In figure 18 jet-spectra for all three triggered data samples are shown period wise. The plots are showing the absolute number of jets per p_t-bin. One should consider that the number of recorded events and jets are not only depending on the trigger conditions and its underlying detectors acceptance, but also the active runtime of each trigger class.

The EMCal trigger samples contain in each p_t-bin the highest number of jets. For the TRD triggered data sample the region of about [10,25] GeV shows a strong deviation from the else typical exponential-like decrease, which here would reveal as straight line in the plots due to the logarithmic ordinate. The deviation itself can be explained with the HJT condition which requires at least three tracks of 3 GeV. This condition is not necessarily been given in events with a 10 GeV jet, whereas for higher jet-p_t this condition is fulfiled much likelier. So events with leading jets not exceeding a certain transversal momentum are stronger suppressed. This consequence will manifest visibile relicts in the jet shapes and will be investigated more intensively in the next chapter.

First to the plots on the left of figure 19: it shows the same spectra again but normalized to the number of recorded events. Here one can see that the TRD and EMCal jet trigger records jet events way more efficiently than the MB one over the whole plotted p_t-region, in all run periods.

In general the shape of the per-event-normalized spectra, for a group of certain trigger classes, should not change between the run periods since here every event is expected to have the same probability for a jet(p_t)-appearance. For clarification the ratios of the spectra between each period are shown trigger wise on the right of figure 19 and

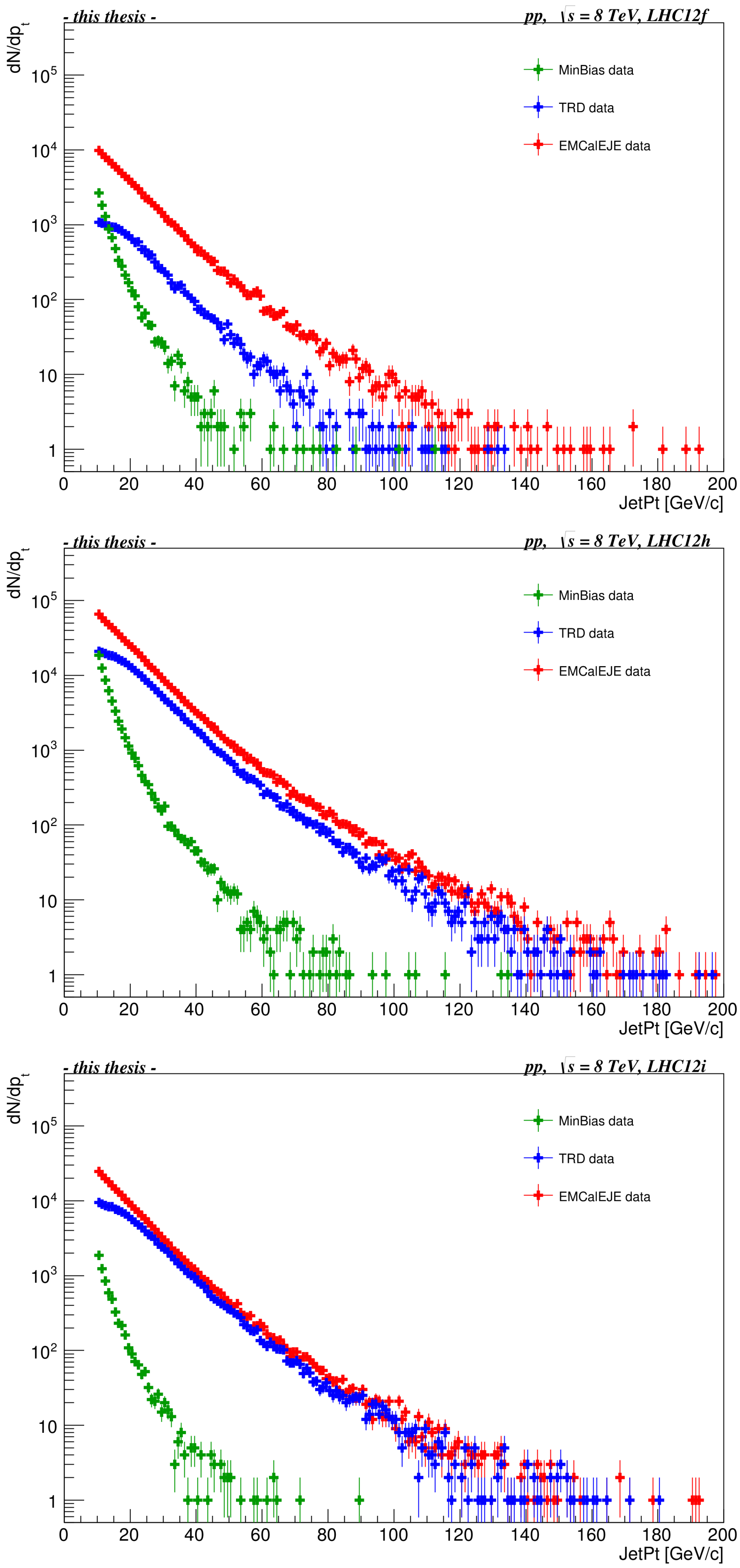

Figure 18: Jet p_t spectra/yield for each oft the three different trigger splitted into three data samples (LHC12f, LHC12h, LHC12i). Pre-defined jet properties are R=0.4, $|\eta| < 0.5$, anti-kt scheme.

their values should be one ideally.
The MB ratios evolve closely around one. Only the region between ten and up to around 15-20 GeV shows up a statistically significant deviation from one for the LHC12h/LHC12f-ratio. The LHC12f period here seems to be up to about ten percent less efficient than the LHC12h.
The ratios for the HJT trigger in the plot lying underneath show stronger deviations. The LHC12h run period seems to be around five percent more efficient than the LHC12i in the region around 10 - 30 GeV. But then the data points alternate stronger around one and soon lose its validity for further statements due to lack of statistics. The comparison of the LHC12h and LHC12f run period shows in contrast to the MB data a higher efficiency for the LHC12f between 10 and 30 GeV. The jet data of LHC12h is about 0.88 times the LHC12f here, but subsequently approaches one and again statistics are too low for further statements.
The EMCal jet trigger finally shows the weakest deviations from one. For both ratios the points seem to alternate very close around one.

In chapter 4 the rejection factor was introduced. In general it gives the ratio of two spectra of two different trigger each normalized to their respective number of triggered events. So it gives finally how much more jets one trigger per triggered event and p_t bin triggers in comparison to another one.
The rejection factors for the different trigger classes and run periods are shown in figure 22, 23 and 24 (left side). First a look on the one referring to MB data (fig. 22, 23). The TRD/MB- and EMCal/MB-rejection factors present a steep increase in the region from 10 up to about 50-60 GeV. As already mentioned in 4.3.2, since there is a plateau expected to be from a certain p_t-value on, a straight line

$$\bar{R}_F(p_t) = p_0 \tag{6.1.1}$$

wheras p_0 is a constant, was fitted to the data points. The fit intervals are given in the table of figure 20.
The upper interval boundary was made due to lack of statistics of the data points in the p_t-region beyond this boundary. The lower one was made as follows: the figures on the right to each rejection factor plot show the evolution of the p_0 value and the reduced χ^2 value for the mentioned straight line fit depending on the fits lower interval boundary. Now the plots show an increasing p_0 and decreasing χ^2/NDF. Both flatten for an increasing lower interval boundary. Finally the lower boundary was chosen to be the beginnig of the first χ^2/NDF plateau. Here the reduced χ^2 value itself proved to have an acceptable value and the p_0 has a small error and agrees with the following. The same chain of reasoning can be taken for the EMCal/MB and the TRD/MB rejection factor. The rejection factors and its errors are summed up in figure 21.

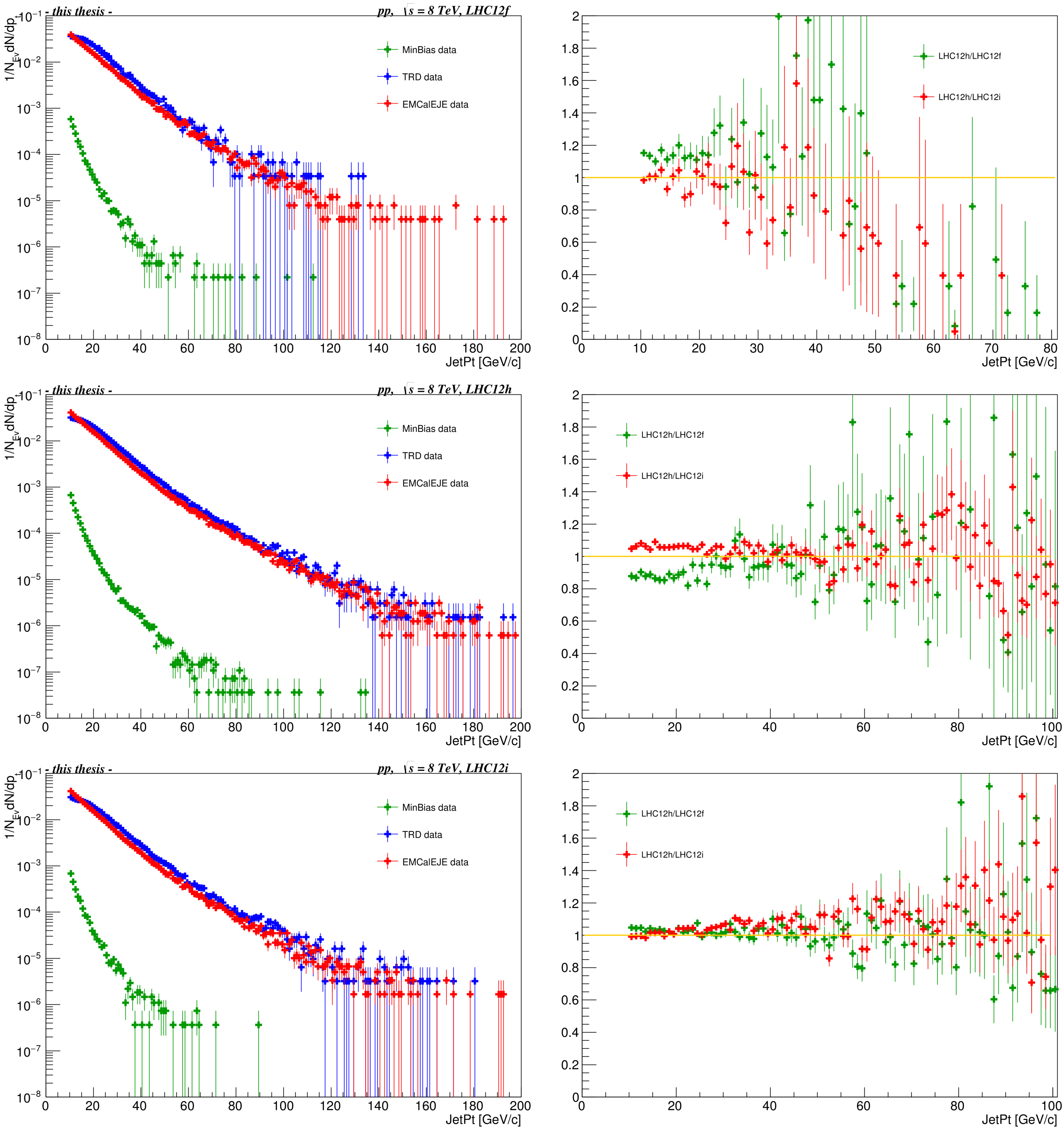

Figure 19: On the left side the jet spectra as before are plotted but normalized on the number of recorded events of each triggered sample. On the right are the ratios of two spectra of two differents runs with the same underlying trigger classes; from top down ratios of Minimum Bias, TRDHJT and EMCalEJE are shown.

	TRD/MB	EMCal/MB	TRD/EMCal
LHC12f	[30,90](1.26)	[35,90](0.41)	[50,135](1.32)
LHC12h	[45,110](0.69)	[45,110](0.57)	[25,200](2.48)
LHC12i	[30,75](1.03)	[30,75](1.04)	[30,165](1.05)

Figure 20: Interval boundaries (in GeV) for the different straight line fits of the rejection factors. The number in parentheses gives the corresponding χ/NDF value for the fit.

Now looking at the plots of figure 22 and 23 (left): the rejection factors reveal a steep increase in the region of [10,60] GeV. In a previous chapter there is shown in figure 15 a plot regarding the trigger efficiency. This one prophecies an increase of the HJT efficiency up to a jet-p_t of 60-80 GeV, which agrees with the increase of the rejection factor up to 60 GeV pretty well. Finally in the crucial region where there would be a plateau expected, the statistic shows to be too bad to make clear predictions. The same occurs in case all three run periods are merged, cf. figure 25. For the latter mentioned figure, including the rejection factor plots for the TRD/MB and EMCal/MB, the lower interval boundary was set to 60GeV, following the trigger efficiency plot and to achieve a better comparison. Also here the reduced χ^2 values are very low which points on a too larger error of the underlying data points to assure a good quality fit. Anyway, apart from the statistics a constant quality of the data recording is crucial for statements of value. For example an unbiased MB trigger cannot be fully given already because figure 19 shows up differently MB behaviours between the run periods, otherwise there would not be visible such strong deviations from one. Also the alternating behaviour between the runs of the TRD reveals uncertainties that are yet not respected in the rejection factor and from this viewpoint there cannot be made assumption for their reasons.

Now a few sentences to the TRD/EMCal rejection factor. The refering plots are in

	TRD/MB	EMCal/MB	TRD/EMCal
LHC12f	1897 ± 164	1699 ± 191	$1,102 \pm 0,068$
LHC12h	2454 ± 172	1822 ± 127	$1,364 \pm 0,012$
LHC12i	1584 ± 156	1079 ± 106	$1,463 \pm 0,013$

Figure 21: Calculated rejection factors for different trigger classses and run periods

figure 24. Here an increase in the region between 10 GeV and up to about 30 GeV is visible, which approximately corresponds to the region biased by the HJT condition. Apart from that the spectra between the EMCal and TRD triggered samples show a very parallel course. Thus the plateau is way better visible compared to the other ones. The only exception is the rejection factor of the LHC12f run period. After a rather stable plateau there occurs an unexpected dip occurs around 50-60 GeV.

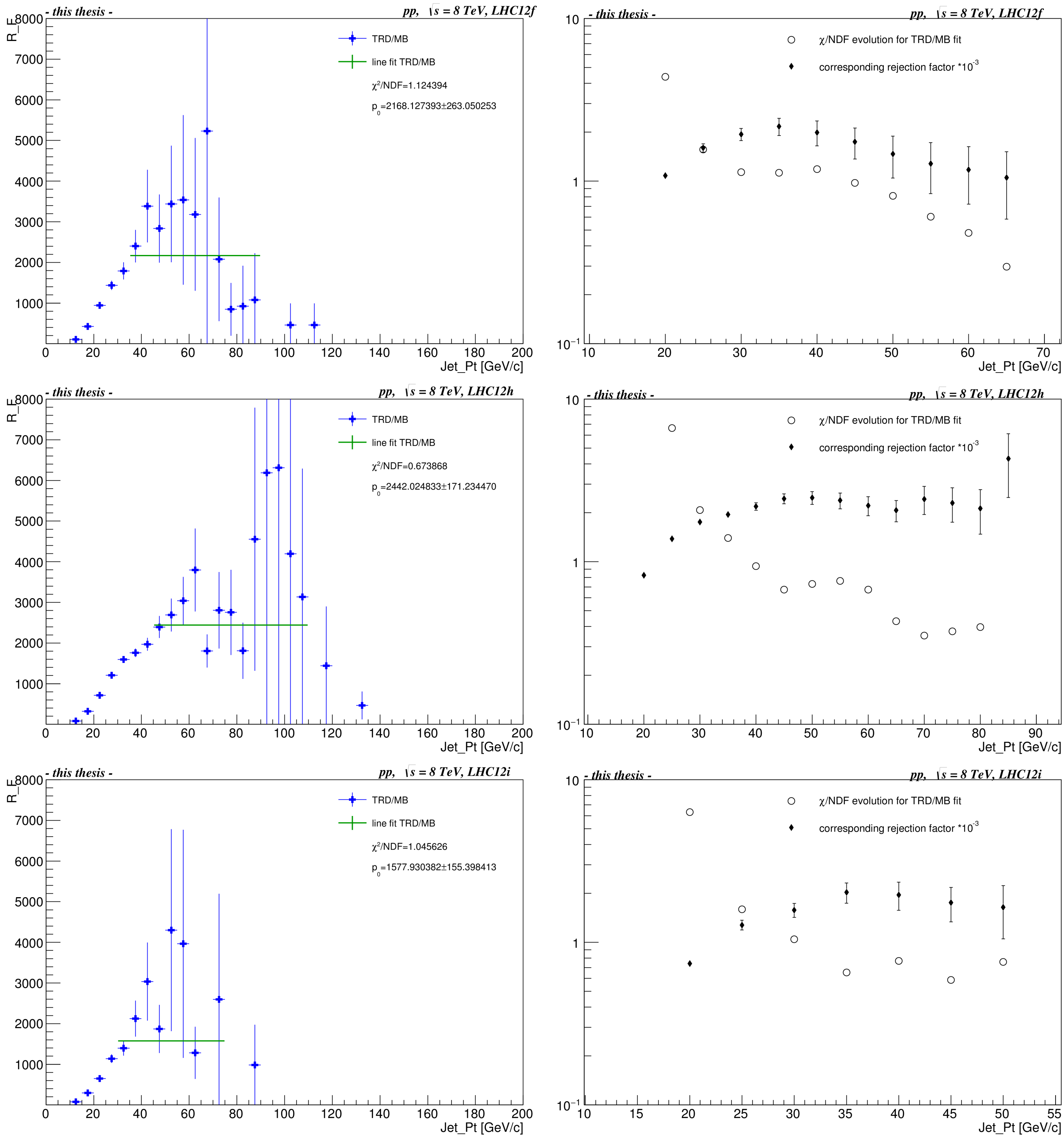

Figure 22: On the left there is the rejection factor plotted against the jet-p_t, showing the TRD jet yield per event in compariosn to the MB. The green line corresponds to a horizontal straight line fit, with the given reduced χ^2 and p_0. On the right there is the evolution of reduced χ^2 and the refering p_0-value.

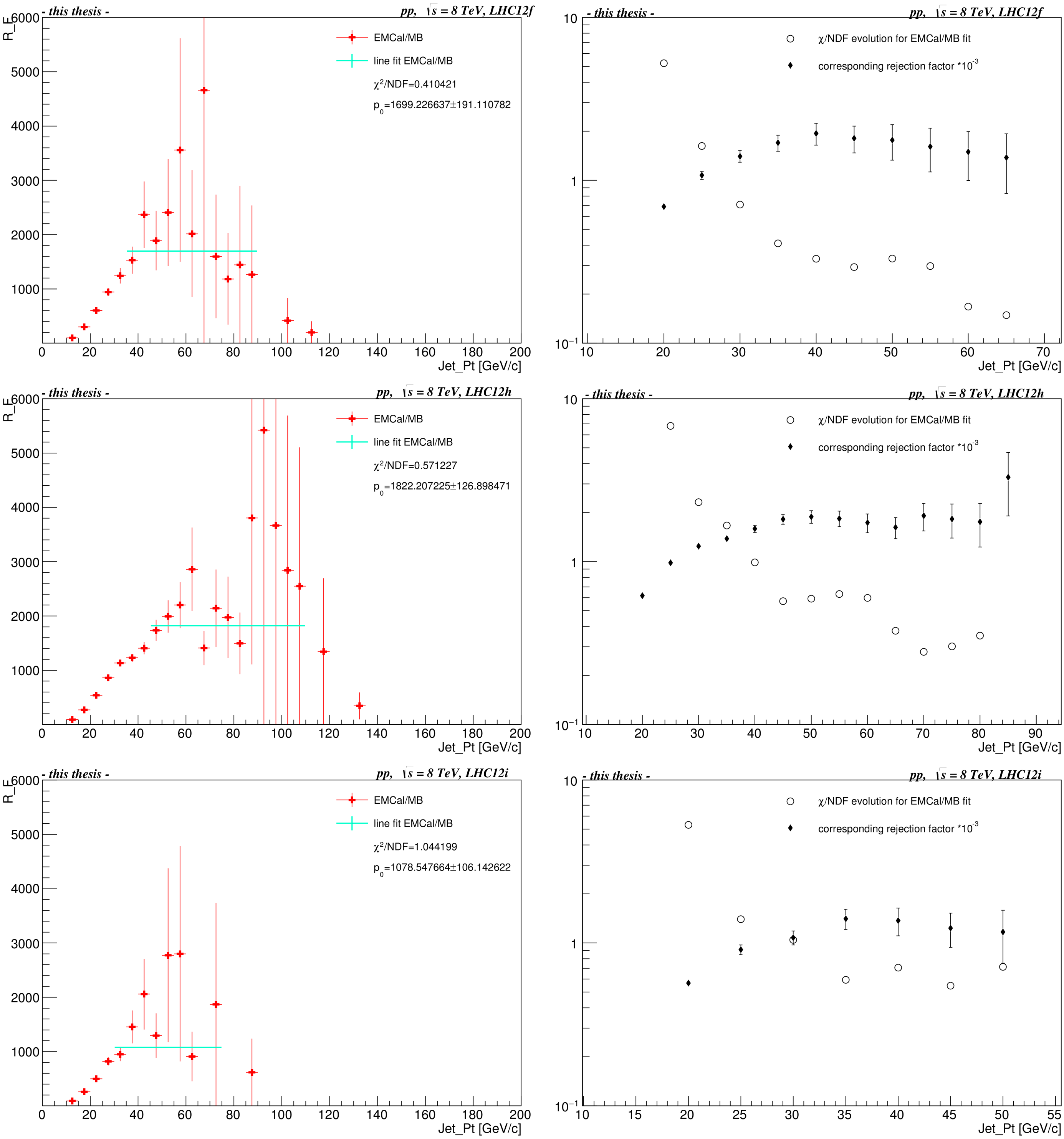

Figure 23: On the left there is the rejection factor plotted against the jet-p_t, showing the EMCal jet yield per event in compariosn to the MB. The green line corresponds to a horizontal straight line fit, with the given reduced χ^2 and p_0. On the right there is the evolution of reduced χ^2 and the refering p_0-value.

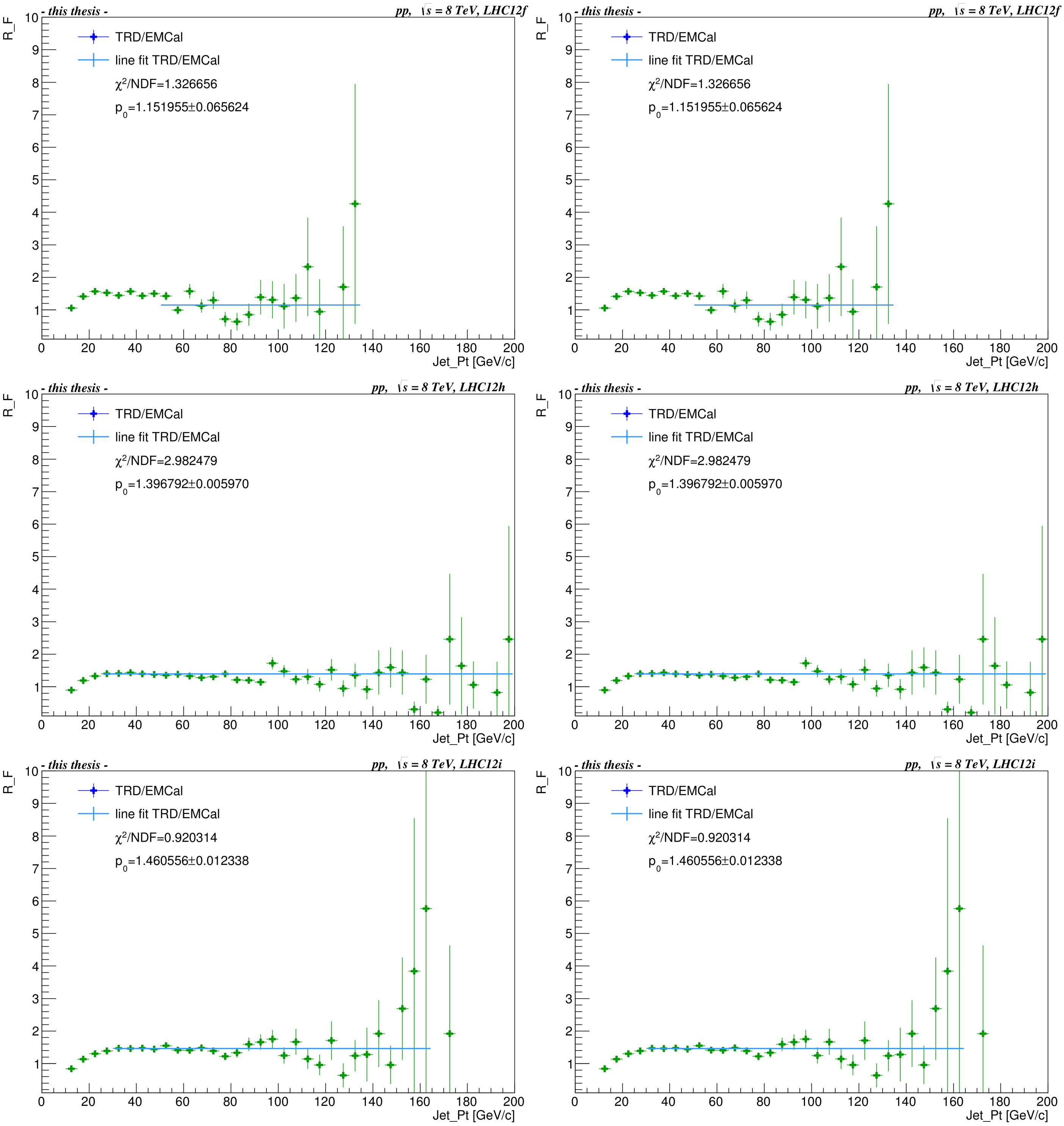

Figure 24: On the left there is the rejection factor plotted against the jet-p_t, showing the TRD jet yield per event in compariosn to the EMCal. The green line corresponds to a horizontal straight line fit, with the given reduced χ^2 and p_0. On the right there is the evolution of reduced χ^2 and the refering p_0-value.

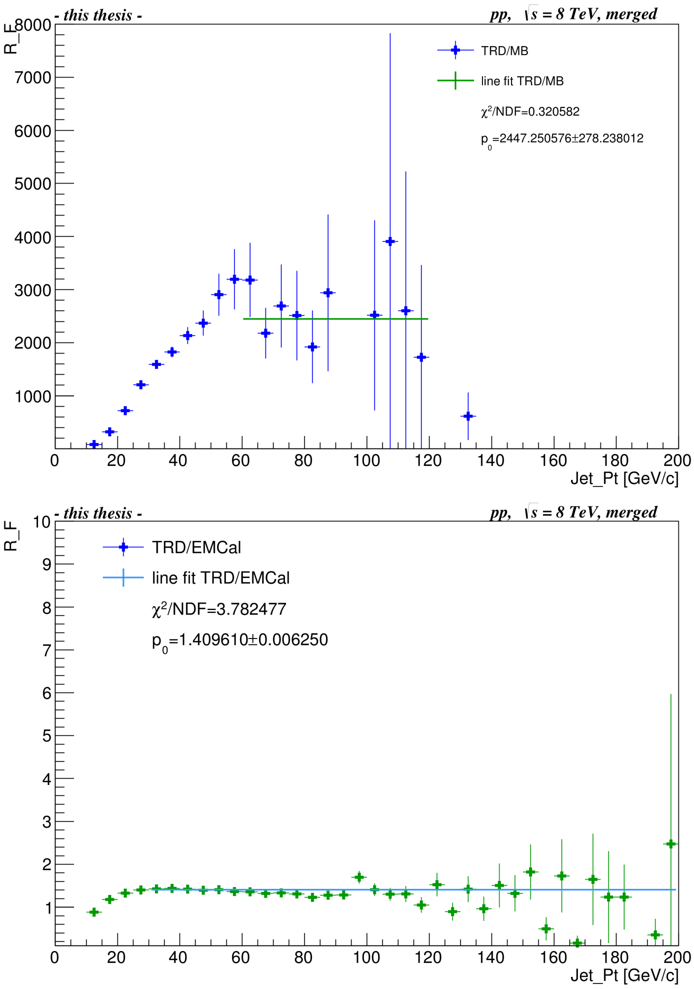

Figure 25: The rejection factor is plotted against the jet-p_t for the same three trigger combinations as before. The data are originitang all the three run periods LHC12f, h, i.

Taking the criteria regarding the χ^2-plots, where the other two R_F-plots show a plateau beginning from 25,30 GeV on, the LHC12f ones lower interval boundary was chosen to 50 GeV. In contrast the rejection factors including MB data show no clear plateau, therefore the data points distribute too much, but alse contain large errors.
Finally, considering in addition the ratios of figure 19 and the values for R_F between different run periods from the tabular in figure 21, one could say that at least further, not yet respected errors need to be considered that might come from problems in the experimental setup. But from this point of view they cannot be closer described. The HJT supported by the TRD records in all run periods the most jets per event with $p_{t,\text{jet}}$ >30 GeV. But the data show different R_F for each run period. Now for further investigation of jets it needs to be respected that the trigger might influence further jet quantities which will be presented in chapter 7. But before so called jet maps shall be investigated to detect possible weak spots in the detector system.

6.2 Jet maps

In this part jet maps, the distribution of reconstructed jets exceeding 10 GeV in the η-ϕ-plane, will be investigated. Each bin was dedicated a hit in case the jet axis was pointing on it. The maps are presented in figures 26 (Minimum Bias), 27 (TRDHJT) and 28 (EMCalEJE), sorted by the underlying trigger condition and run periods. In addition there is presented the ratios between the run periods on the right, but normalized on their respective number of triggered events. The aim is to check the detector on irregular low or high activities. Serving this purpose a map showing the distribution of all particles in the whole η-ϕ-plane would be preferable, but unfortunately hasn't been made.
The maps show as expected no visible jets for η>0.5, since all jets have been cut off here to exclude boundary effects. The only exception is the bin in the upperleft corner, which was added afterwards and represents for overview the colour corresponding the average bin content. Since the TRD and the EMCal do not cover fully in azimuth, one needs to expect in covered regions a higher jet activity. This does not cause boundary effects since the underlying particle tracks used for the reconstruction are not limited to this regions, only the refering trigger conditions are limited to the restricted regions and consequently lead here to a higher jet appearance. This should not occur for the MB trigger, already for that reason that its dedicated detectors lie outside the here plotted maps.

The MB maps (figure 26) in general show the expected statistical fluctuations. Only the LHC12f shows in the region of $0 < \phi < 1$ and $-0.5 < \eta < 0$ area of lower jet activity.

The TRDHJT maps (figure 27) show the inner structure of the TRD as well as the missing supermodules. From the five stacks in η-direction three are only visible, since the outer two are outside the jet acceptance. All thirteen of eighteen supermodules in ϕ-direction are clearly visible. The structure is visible for the reason that the trigger condition needs three particles above 3 GeV within one stack. Jets whose axis are pointing to its boundaries are suppressed, since their particles likelier distribute over more than one stack and consequently fulfil the trigger condition less likely. If assuming the case of higher energetic jets which split into more and more particles beyond 3 GeV then this effect might begin to disappear. Finally one should mention the fact that the jet radius is set to R=0.4 but each of the stacks covers approximately an area that correspondends to a jet with R=0.2. Finally one can mention that, to reduce the material in front of PHOS, the most central stacks of supermodules 13, 14, 15 are left empty. In this run periods supermodules 13 and 14 are not installed anyway, but the central one of supermodule 15 is good visibly missing.
For the ratio LHC12h/LHC12f the dedicated map reveals higher fluctuations outside the detector area. But this is no big surprise since a lower amount of jets in the regions outside cause higher fluctuations due to its larger relative error anyway. On average run period LHC12f delivered more jets per event. For the LHC12h/i ratio there appear two regions of higher activity. The uppermost visible stack of supermodule 10 and further around $2{,}0 < \phi < 2{,}6$ for $\eta < 0$ there is a second region of higher acticity.

The EMCalEJE maps (figure 28), same as the TRDHJT, clearly show a restricted area. The structures within will not be explained here. An interesting feature occuring here is that jets are often accompanied by jets in the opposing azimuth within one collision. These so called dijets cause in the here presented map a slight increase in the area opposing the EMCal detector. For the ratio LHC12h/LHCf the dedicated map reveals higher fluctuations offside the detecor area and its opposing area. An area around ϕ=1.5 and $0.1 < \eta < 0.5$ might manifest a lower activity during the LHC12h run. This area of low activity also occurs in the opposing direction. For the LHC12h/i the just mentioned areas not visible anymore but here the graphic shows a broad stripe around $2 < \phi < 3$ which affects crucial part of the EMCal detector though the ratios average bin content lies close to one.

Finally the maps reveal regions of lower or higher activity, but one cannot say from this viewpoint if these regions are responsible for the irregeularities between and within the run periods ratios and rejection factors. The ratio of the jet map between period

LHC12h and LHC12i for example shows a region of higher activity but this does not seem to influence the amount of detected jets, following the average bin content.

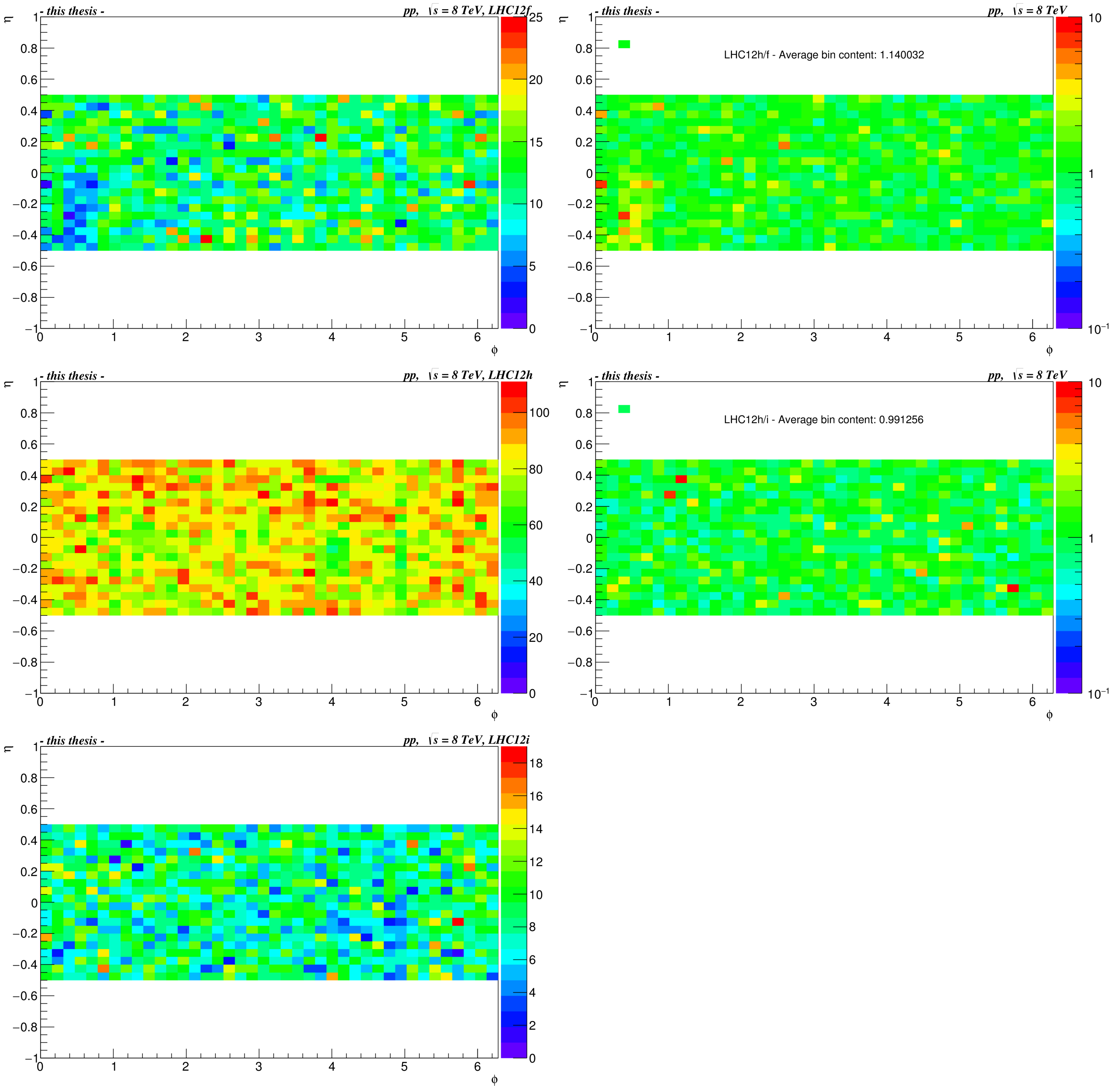

Figure 26: (left) Jet maps of the MB triggered sample. (right) Ratios of two run periods from the right but each run periods map normalized on their respective number events before.

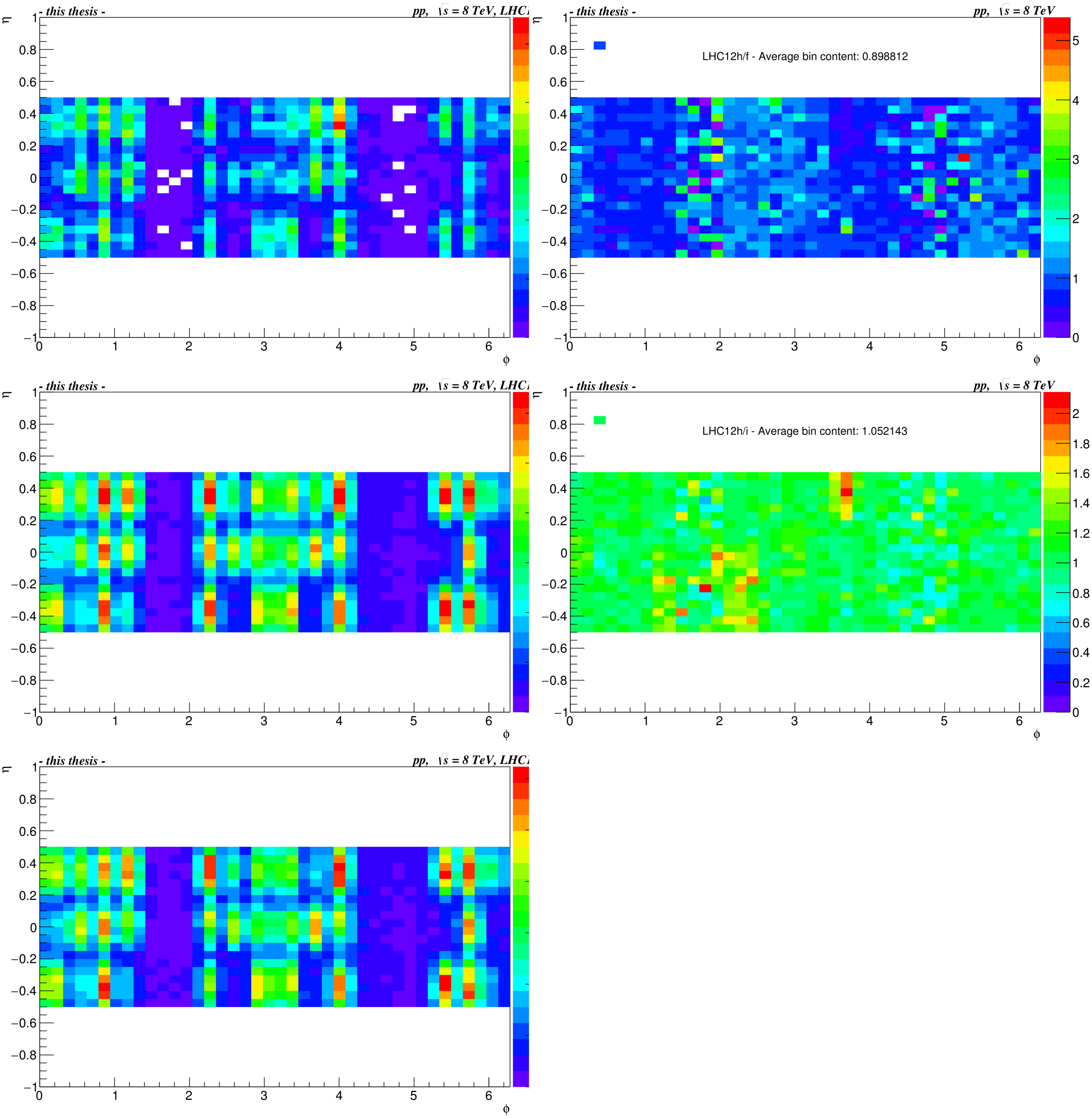

Figure 27: (left) Jet maps of the TRD triggered sample. (right) Ratios of two run periods from the right but each run periods map normalized on their respective number events before.

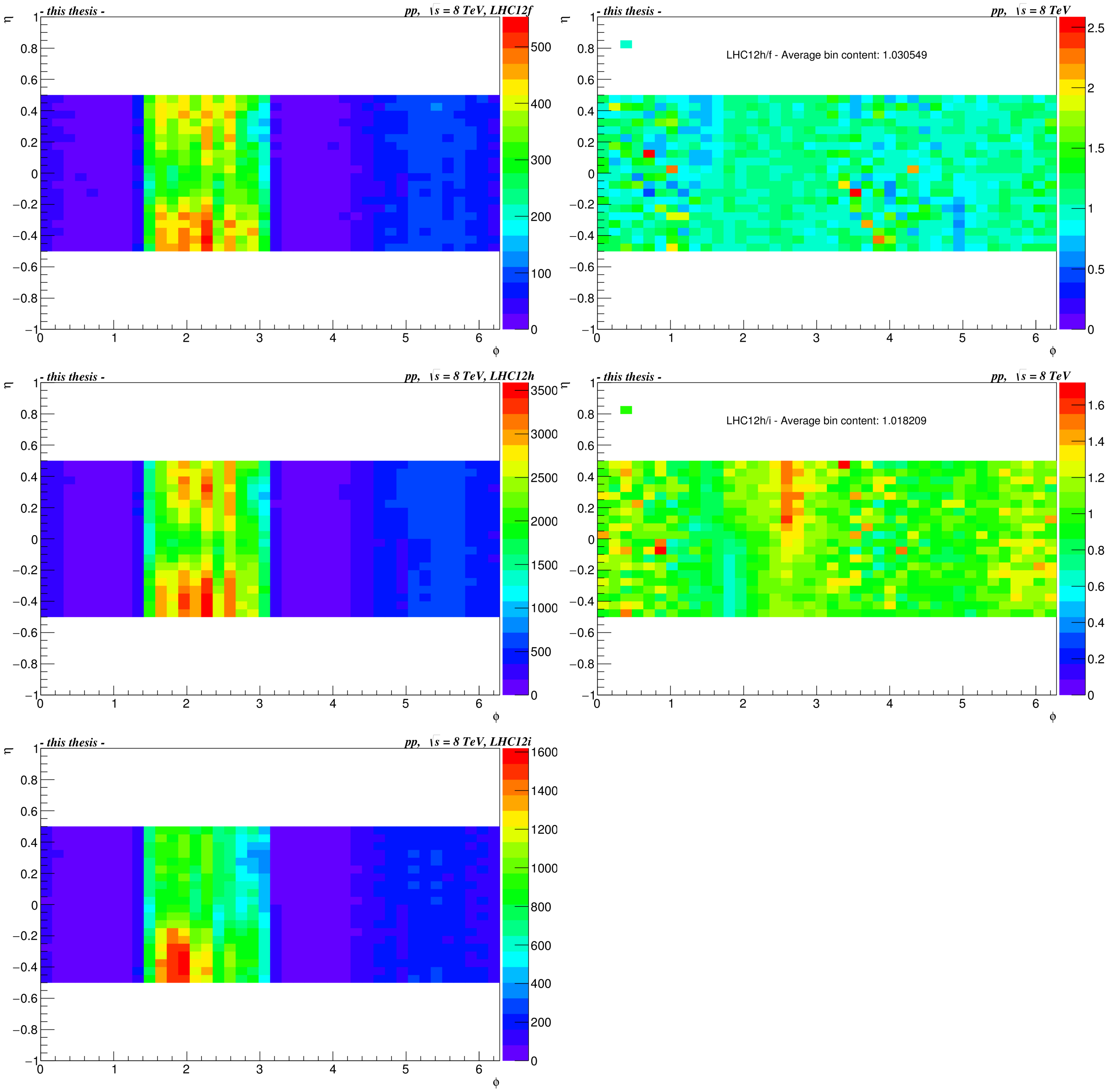

Figure 28: (left) Jet maps of the EMCal triggered sample. (right) Ratios of two run periods from the right but each run periods map normalized on their respective number events before.

7 Jet analysis with triggered events

In this chapter the jet shape analysis shall be presented and discussed. The underlying data sets are the same as before. First a comparison between the run periods of the respective shape will be made and if applicable, the jet shapes of a new dataset, which sums up all three run periods, will be presented. The aim is to identify trigger biases by comparing triggered data with MB data and following their evolution with increasing jet-p_t.

7.1 Fragmentation function

The fragmentation function was already introduced in chapter 2.3.1. Its definition through equation 2.3.1 assigns the hard jet constitutents a low value whereas to the soft constituents a high value will be assigned.
In figure 29 the fragmentation function of MB data sets is plotted period wise for two jet-p_t-windows. On the right side there are plotted their ratios in addition. For this jet shape there are no statistical differences visible between the run periods for each trigger respectively. The plots on the left reveal a gaussian-like shape for the fragmentation function. The maximum lies around ξ=2 in the upper case, which corresponds a constituent-p_t between 1.4 GeV, for a 10 GeV jet and 2.7 GeV for a jet 20 GeV jet. The upper plots data point boundaries are given to ξ=0, for a jet consisting of only one constituent and to $\xi \approx$4.9 which is the result of a constituent with p_t=0.15 GeV in a jet of p_t =20 GeV. It should be noted that constituents below that p_t are cut off. So each p_t-window has its own boundaries whereas the lower one is zero and the upper depending on the highest allowed jet p_t and the lowest allowed constituent p_t.
The ratios on the right side confirm the apparent similarity of the three shapes on each ratios left respectively. The increasing fluctuations and errors in the ratios, as one approaches the mentioned boundaries, are explainable through decreasing statistics. For higher p_t-windows, as the two given here, the statistics are too low to enable any conclusions between the run periods. So as a result there does not seem to be any reason for not merging the data sets of the three run periods to provide a better jet sample.
In figure 30 the same plots as discussed before, but for the HJT data set, is presented. The fragmentation function here shows in addition an eye-catching bulge in comparison to the MB data which was not there before. But this will be discussed later in detail. For now the focus lies on the period wise comparison. The LHCh and LHCi run periods agree very well in all three p_t windows. This is also confirmed by the ratios on the right. However in the p_t-window of [10,20) GeV there are deviations visible. In the LHC12f case the bulge is more intense and the area around ξ=2.5 is visibly suppressed, though they are rather weak, they are statistical relevant. For the following p_t-windows there

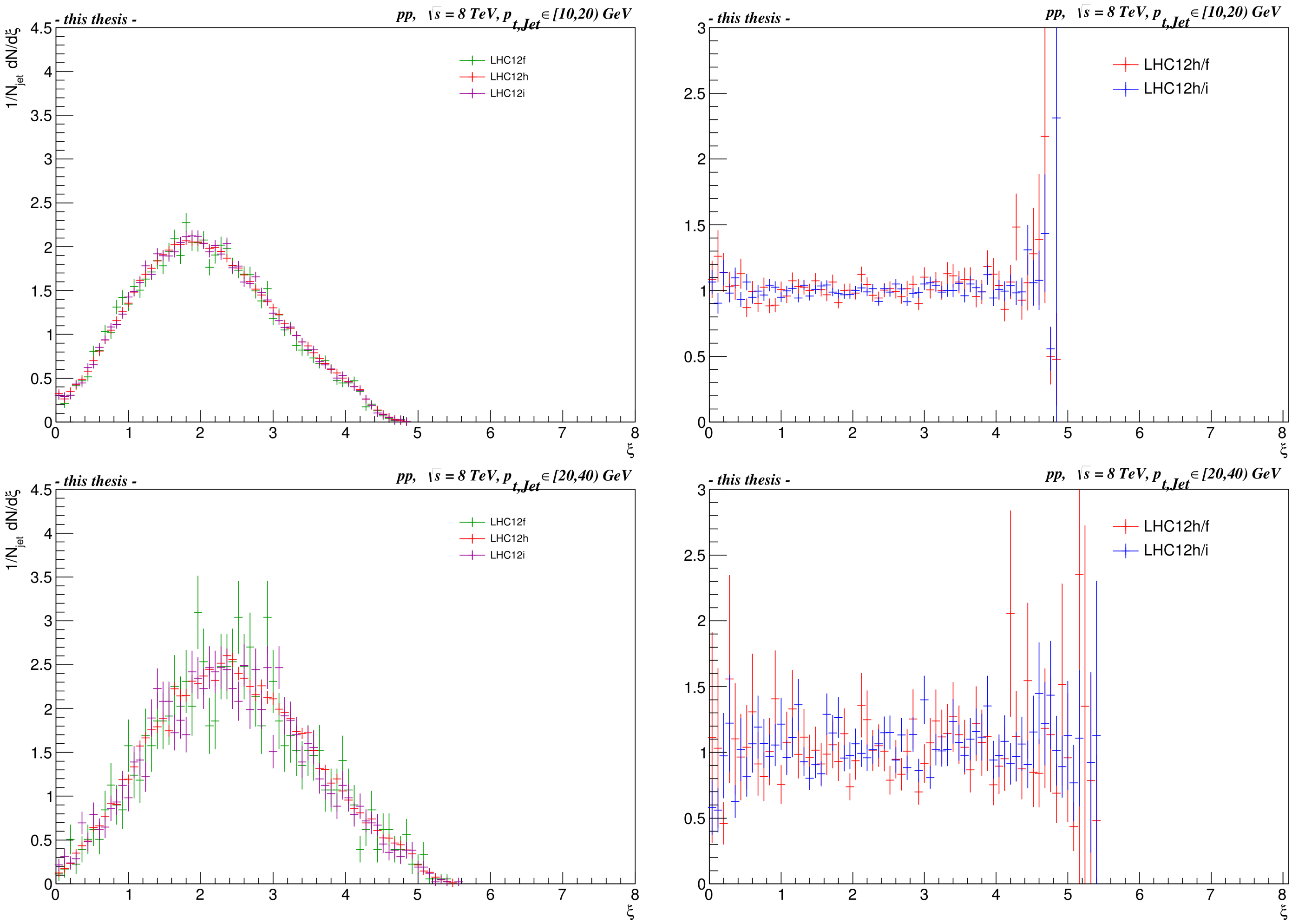

Figure 29: (left) The fragmentatios functions using MB data, drawn for all three run periods in each of the two p_t-windows. (right) The ratios of the plots from the left between two run periods.

still seems to appear relicts of this deviation, but they gradually disappear and become statistical irrelevant through its increasing error. For the following p_t-windows there are no comparisons between the periods possible for the same reason. The merged data set will be discussed in the following.

For the fragmentation function of the EMCal data set (figure 31) all three run periods in all three windows on the first sight seem to agree very well. Whereas a view on the ratios reveals deviations between the runs for the lowest p_t-window for soft jet constituents. But these deviations disappear with increasing p_t. Taking the same chain of reasoning as for the TRD data set all three runs will be merged here too.

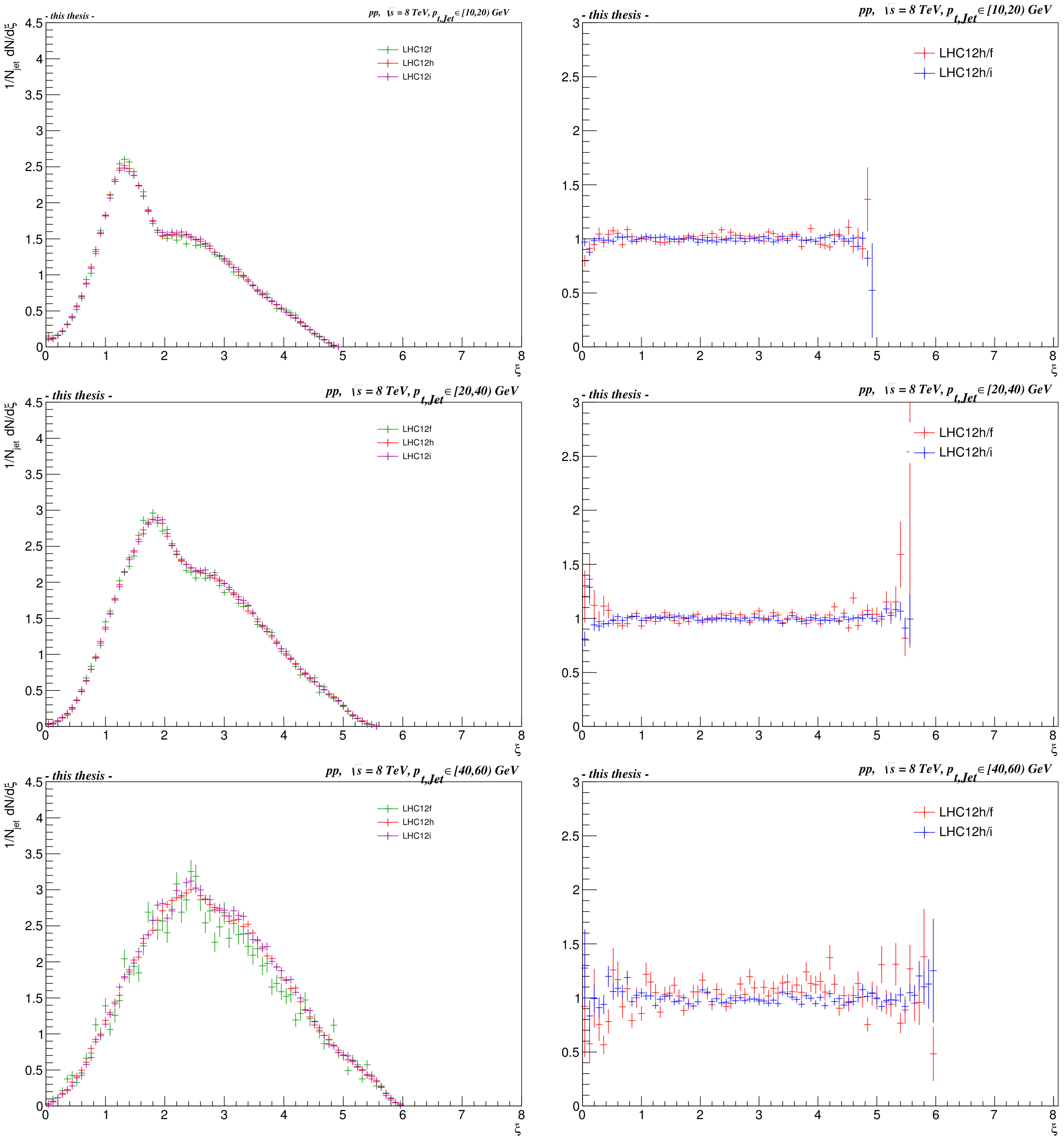

Figure 30: (left) The fragmentatios functions using TRD data, drawn for all three run periods in each of the three p_t-windows. (right) The ratios of the plots from the left between two run periods.

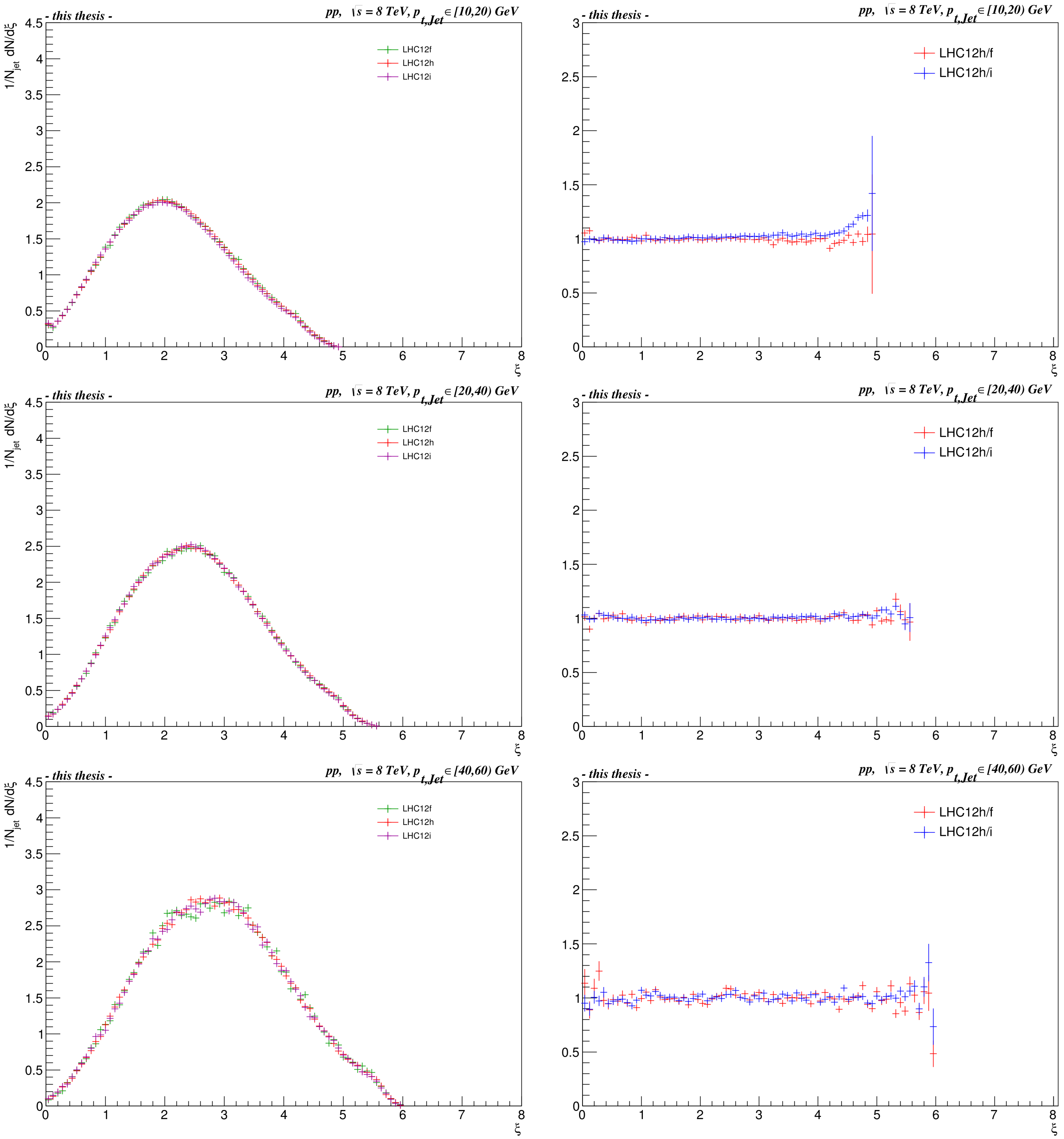

Figure 31: (left) The fragmentatios functions using EMCal data, drawn for all three run periods in each of the three p_t-windows. (right) The ratios of the plots from the left between two run periods.

Now as all three run periods have been merged, the trigger can be compared and the evolution of the fragmentation function with increasing p_t can be investigated. In figure 32 the fragmentation function is visible for the whole here observed p_t-region. Therefore it is depicted in six p_t-windows. At first remarkable regions within the shapes shall be discussed. Around ξ=4.2 there appears something that reminds of the cosmical knee. The knee here can be explained as follows: tracks below 0.15 GeV are cut off. A constituent of this momentum in a 10 GeV-jet has a ξ value of 4.20. Since this is the highest ξ-value constituents, part of a 10 GeV-jet, can have, these jets are not able to influnece the fragmentation functions plot in the region beyond anymore. So from ξ=4.2 on the amount of jets, which are part of this histogram and cannot fill the the histograms region anymore increases. Consequently a stronger decrease within the shape takes place, which starting point is given through the lowest jet-p_t and the lowest constituent p_t in any histogram and visible as a knee shape. Of course the smaller the chosen p_t-window is the less distinct the knee is.
Further there is a clear bulge in the fragmentation function, only visible for the TRD data set. Now one needs to reconsider the trigger conditon, which includes that finally three particles of a $p_t \geq 3$ GeV are required within one stack. This leads to an accumulation of constituents beyond 3 GeV. Now assuming a 3 GeV particle in a 20 GeV jet. This particle is assigned $\xi = 1.90$. This also corresponds to the end of the bulge. Constituents with higher ξ-values do not fulfil the trigger condition anymore. On the other hand there are also jet constituents that are disfavoured by the HJT condition and so derivations appearing as suppressions compared to the unbiased data in the fragmentation plot. For example, in a jet of 10 GeV firing the trigger, there are no particles beyond 4 GeV. The reason is as follows: a 10 GeV leading jet being responsible for firing the trigger cannot contain any constituent higher than 4 GeV since there need to be at least two more constituents with 3 GeV. A particle of 4 GeV in a jet of 10 GeV corresponds to $\xi \approx 0.91$. For a jet with any p_t firing the HJT the upper constituent-p_t is given through

$$p_{t,\max}^{\text{const}} \leq p_t^{\text{jet}} - 6\text{GeV}.$$

Though one needs to consider that such constituents exceeding $p_{t,\max}^{\text{const}}$ are still possible. There still might be jets not firing the trigger but though containing such constituents. But anyway the fragmentation functions plot for $p_t^{\text{jet}} \in [10, 20)$ GeV reveals a lower fraction for very hard constituents, which likely originates the not being favoured of such constituents exceeding $p_{t,\max}^{\text{const}}$ due to the just explained mechanism. A similar mechanism appears for constituents with $p_t \in (1-3)$, since they would increase the jet-p_t and so are excluded to be constituents for 10 GeV jets. A similar suppression on the right of the bulge takes place and is also visible.
Also the maps of figure 27 and 28 prompt that jets not fulfiling the trigger condition

are strongly suppressed, since they are equally distributed over the whole η-ϕ range, but outside the areas which are covered by the trigger detectors, jets hardly exist.
Now a word to the first bin. After the maximum a decrease takes place, to both sides, except for the very first bin. This bin contains all single particle jets, independent from p_t. This originates the recombination scheme applied here, which assigns every track to a jet. If there is no particle left to be recombined with or the next particle is just too distant, single particle jets are generated.
Now one can discuss the evolution from one p_t-window to another. The EMCal and the MB triggered data set agree over all p_t ranges very good. Since the analyzed data for the MB triggered data set are not sufficient in high p_t-windows the EMCal sample will be the relevant to identify further biases of the TRD data sample. It is clearly visible that the bulge disappears with increasing jet-p_t. The last p_t-window where there is a relict of the trigger condition visible is the the interval of [60,80) GeV. But here errors already start smearing the bulge in the one or other direction. For the windows beyond 80 GeV there is no bias visible anymore. The last p_t window sums up a very wide range. A more detailed analysis here requires more data.
The detailed analysis of the evolution of the fragmentation itself detached from any bias observations is not part of this thesis. But though few obvious and helpful conclusions will be presented. By looking at the plots the maximum of the fragmentation function of the EMCal triggerd sample can be estimated. It evolves from $\xi \approx 2$ (1.4 GeV) for jets with $\mathrm{p}_{t,jet} \in$[10,20) to $\xi \approx 3$ (3 Gev) for jets with $\mathrm{p}_{t,jet} \in$[60,80). The value in brackets corresponds to the constituent-p_t for a jet of the lower p_t boundary with the given ξ. The ordinate shows an increase of about one over the same p_t-interval. This says that jets with increasing p_t distribute their p_t as well on higher amount of particles as on an increasing particle-p_t. This finally would lead to the disappering of the HJT induced biases, since the trigger conditions are for very high p_t-jets, such with $p_t > 60\,\mathrm{GeV}$, are fulfiled much more likely.

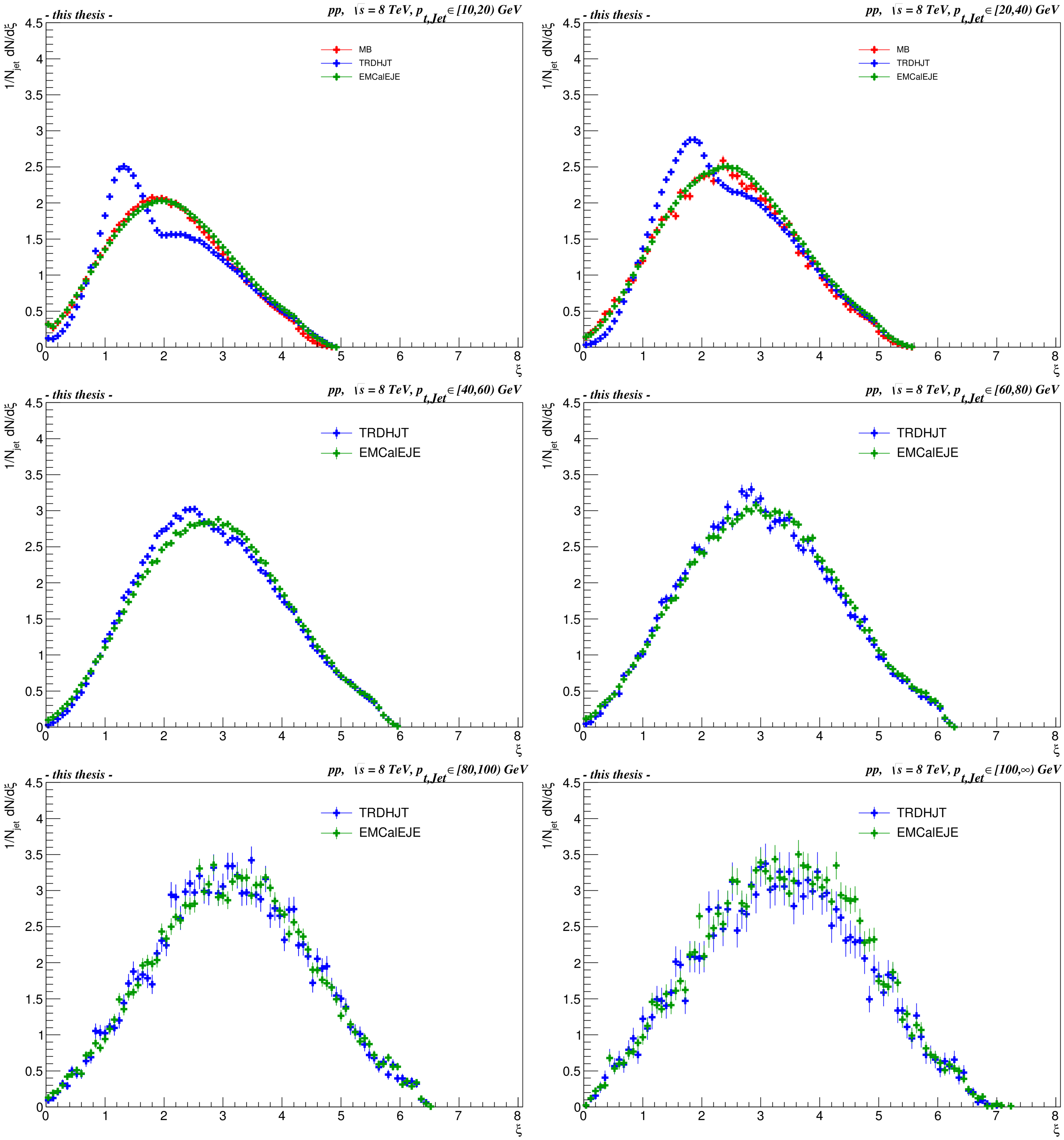

Figure 32: The fragmentation function depicted in six p_t-windows for the merged data sets separately for each trigger.

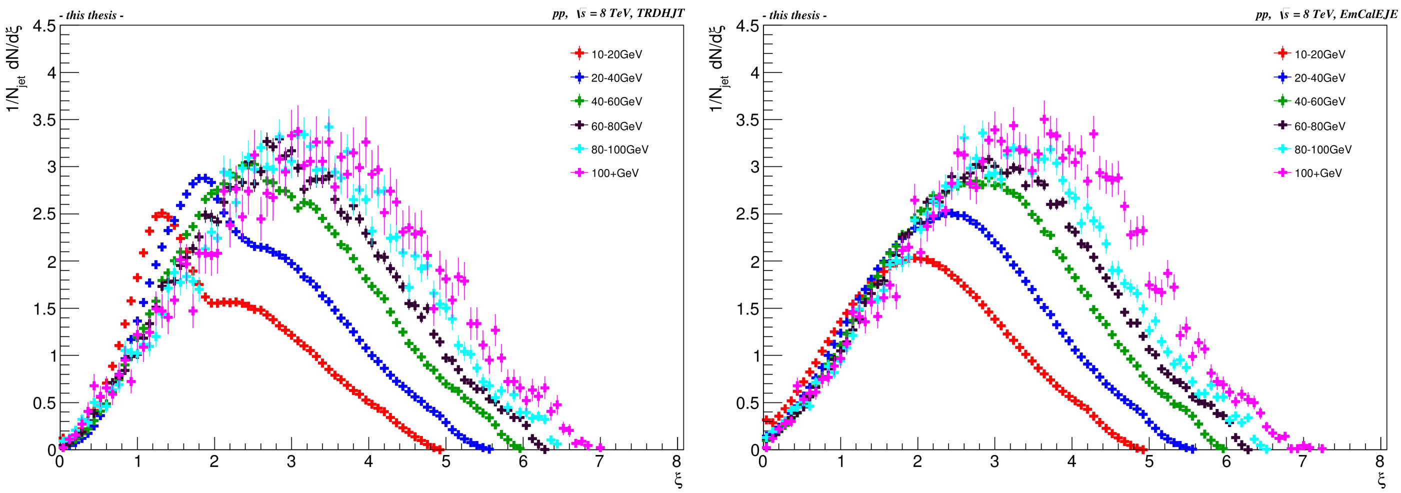

Figure 33: Evolution of the fragmentation function with increasing jet-p_t for the TRD data sample (left) and for the EMCal data sample (right).

7.2 p$_t$ dispersion

The p_t-dispersion was introduced in chapter 2.3.2 and its quantity is given through formular 2.3.2. It describes like the fragmentation function the hardness/softness of the jets fragmentation. But here every jet is assigned a value once and not each constituent. Further each graphs integral is normalized to one. Before going into detail the run wise ratios shall be contemplated again.

In figure 34 ratios and comparisons of the MB and TRD triggered samples are presented run period wise. For both trigger samples the values between the periods agree within their errors. One already notices that the underlying statistic is way poorer than in the shape discussed before and this will also appear for the girth. This is no big surprise since the values filled in the histograms are generated jet wise and not constituent wise.

In figure 35 four plots comming from the EMCal dat set are shown . For all three ratio plots the ratios of LHC12h/LHC12f begin to diverge below a value of about 0.35. Here the dispersion of the LHC12i of the region below 0.35 is increased in comparison to the other two periods and the LHC12h one in comparison to the LHC12f, though the ratio LHC12h/LHC12i approaches one for a higher becoming jet-p_t. The p_{tD} value itself decreases for an increasing number of jet constituents (as long as the added constituent-p_t does not exceed the other ones) and for a given number of jet constituents it becomes minimal if the momentum of all constituents is equal. Nine particles of the same momentum would deliver a p_{tD} value of one third, independent from their p_t. So the regions of deviations of the EMCal data sample between the run periods contain at least nine particles or more. This could mean that very soft jets, jets with a rather large amount of constituents, thus with rather low constituent-p_t are suppressed for

the LHC12f or the other way around increased for the LHC12h/LHC12i run period. So when comparing the merged data set of all three run periods one needs to consider that for the region below p_{tD}=0.35 the EMCal data is not a good comparison for the mentioned region and since the integral over all p_{tD} bins is one and an overpopulation in one region causes a decrease for the rest the whole plot proves so far not to be unbiased.
In figure 36 therefore finally the dispersion is plotted for all run periods of the EMCal data set and the merged MB sample for two p_t-windows. The LHC12f period shows up to agree best with the MB data. From this point of view the LHC12h and LHC12i run periods might be overpopulated in the questionable region.

Now since here were discussed the period wise differences for the p_{tD}-dispersion one can go ahead with the trigger wise comparison of the merged data sets. For this purpose in figure 37 all six p_t-windows are plotted comparing the different behaviour of the trigger. Again the first one shall be discussed in detail.
In theory the possible p_{tD}-interval that can be populated by jets of a given jet-p_t-window is given through 1 as upper interval boundary and corresponds to single particle jets. The lower interval boundary depends on the highest allowed jet-p_t and the lowest allowed constituent-p_t. This gives the highest number of constituents a jet in a window can have and so the lowest possible p_{tD}-value. For the first p_t-window a jet of 20 GeV can have maximal 133 times a 0.15 GeV constituent and would so be assigned with $p_{tD} = 0.09$. But this is rather unlikely. In all p_t-windows the lower interval is $(\approx 0.2, 1]$, whereas the lower interval boundary of $p_{tD} = 0.2$ agrees to jets of at least 25 constituents.
The global maximum in the [10,20) GeV window is populated around $p_{tD} \gtrsim 0.5$ for all three triggered sets. A value of 0.5 corresponds to a jet with four constituents of equal p_t. Whereas the MB and the EMCal data sets correspond over the whole range very good, the TRD set shows a more distinctive maximum but flattens way faster going in direction to the outer boundaries. Apart from the discussed maximum three further peaks appear. The last data point contains all single particle jets. This phenomenon already appeared in the fragmentation function. Apart from this peak there appear two further agreeing to jets splitting its p_t on exactly two constitutent ($\hat{=} p_{tD} = 0.71$) and on exactly three constituents ($\hat{=} p_{tD} = 0.58$). It is discussable if that one in case of a jet of four constituents with the same p_t is also visible. But it would mingle pretty strong with the maximum. An explanation for these peaks could be that below any mentioned peak, jets with the according number of constituents are not possible anymore. Jets of n constituents only can populate the region

$$p_{tD}^{Jet}(n) \in \left[\frac{1}{\sqrt{n}}, 1\right) .$$

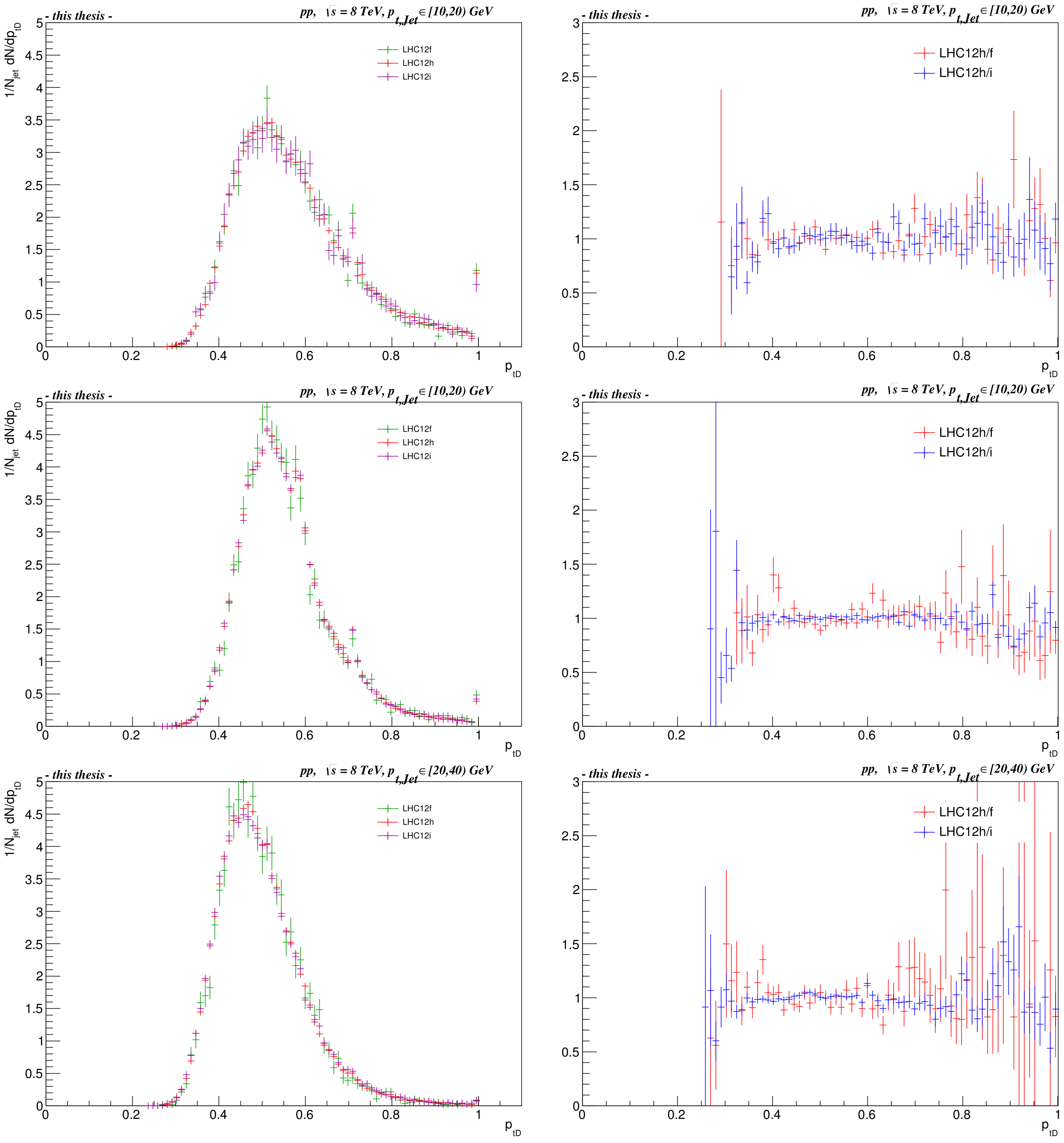

Figure 34: (left) p_t-dispersion plots resulting MB data (top) and TRD data (center, bottom) drawn for all three run periods in each of the tow p_t-windows. (right) The ratios of the plots from the left between two run periods.

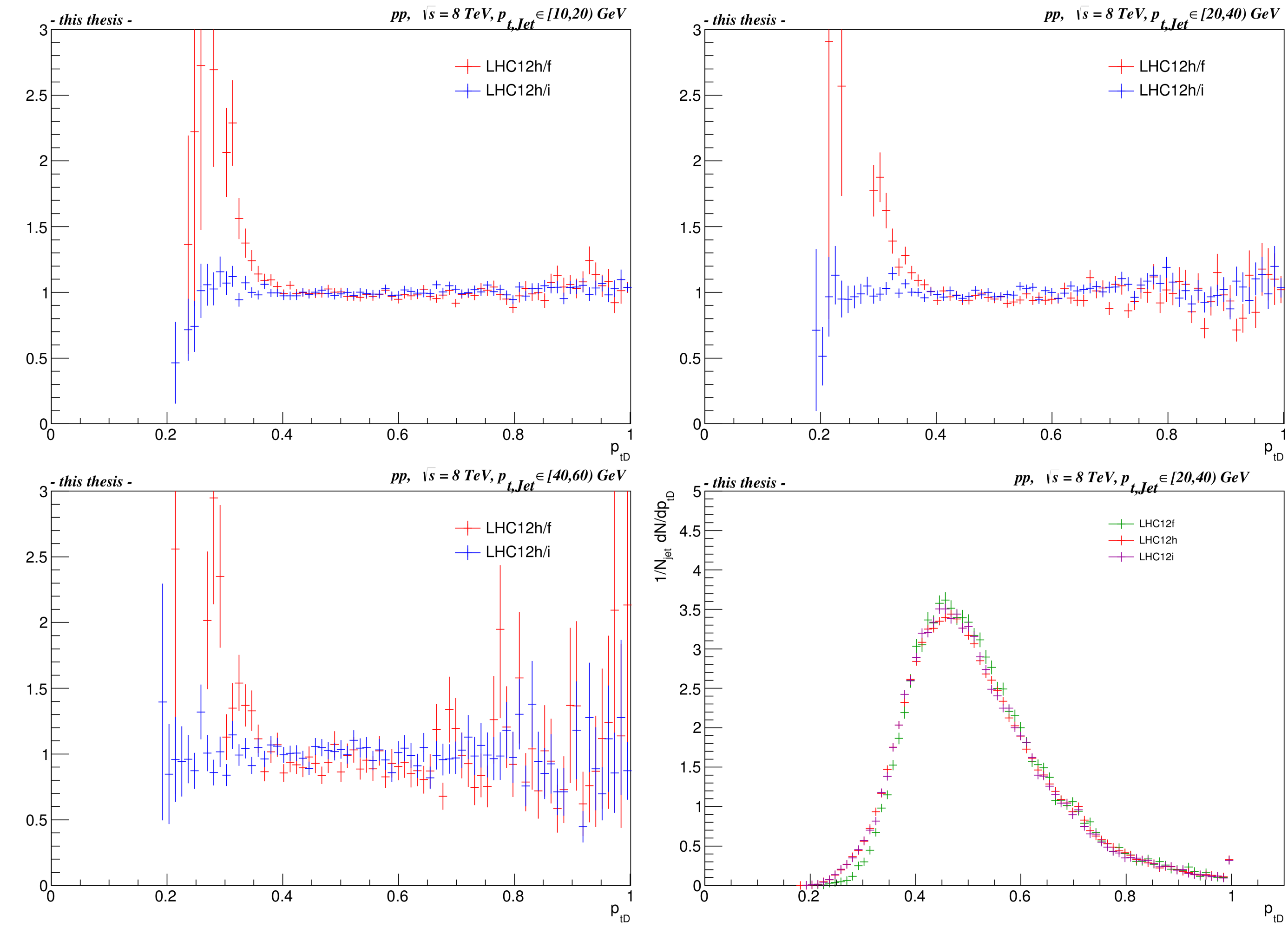

Figure 35: (bottom right) The p_t-dispersion resulting EMCal data drawn for all three run periods. (rest) The ratios of the plots of three p_t-windows, analgous to those ones before.

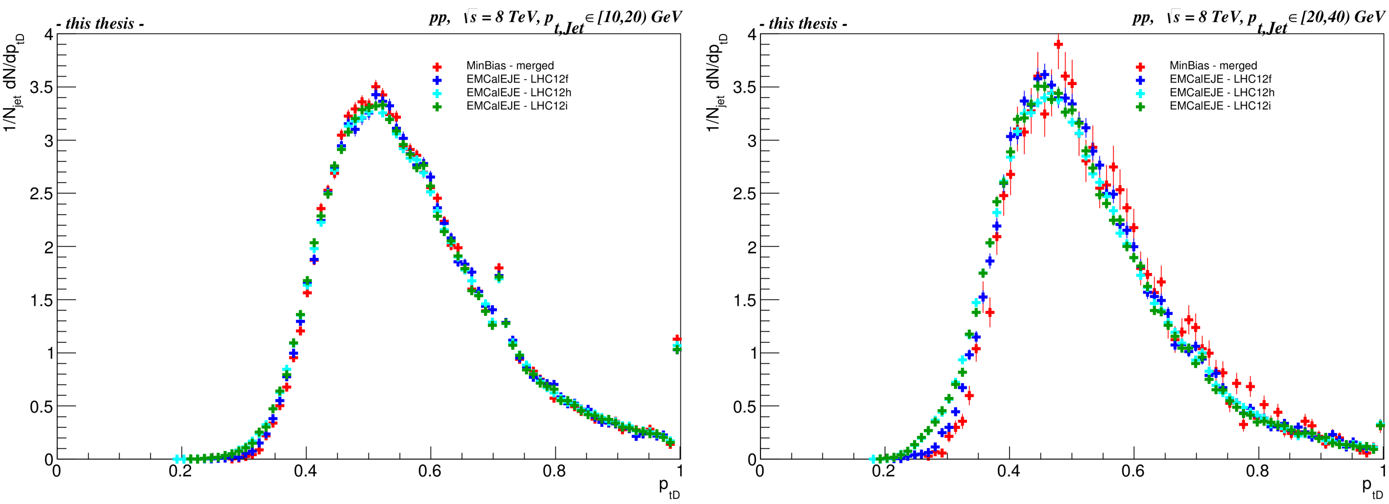

Figure 36: Comparison of the p_t-dispersion plot for MB triggered data (all three run periods merged) vs. EMCal triggered data separate for each run period.

So below the lower boundary, due to lack of jets with less than n constituents, jet possibilities disappear and a sudden decrease in the dispersion is visible.
The peak for three constituents of the same p_t is more remarkable for the TRD sample than for the other two trigger samples, since it requires 3 particles of at least 3 GeV in one stack. A 10 GeV jet fulfiling the HJT condition is rarely dominated by the through the condition necessary particles. For the other two trigger this peak almost disappears in the distribution and is only visible as a small bump.
For increasing jet-p_t it is likelier that the jet contains more constituents, which already was observed for the fragmentation function. So one can expected that the mentioned peaks disappear and the maximum shifts to the left where softer jets are populated. This is indeed visible in the evolution of this shape. The mentioned peaks almost disappeared completly, only slight relicts remain for jets with a $p_t \in [20, 40)$. The only peak that also remains in higher p_t windows is that one including single particle jets. The maximum also shifts slowly to lower p_{tD}-values and so revealing jets with an increasing number of constituents.
The main biases introduced by the HJT are the stronger peak for jets with three particles of similar p_t and the more distinct maximum with the consequently more to the maximum centered shape. The peak already practically disappeared in the [20,40) GeV window. The more distinct maximum on the other side stays more remarkable compared to the other trigger samples also for the following of [40-60) GeV. But the statistics of the minimum bias here is already so bad that a detailed comparison is impossible. Therefore one can take the EMCal data set as comparison which agrees as well with the MB data set though one needs to consider that here a comparative overpopulation in the very soft region was ascertained and so leeds to a overall bias through it normalization. Consequently and considering the larger becoming errors no statements regarding biases can be made for jet windows exceeding 40 GeV. Only the overall shape in general seems to fit.

7.3 girth

The girth was introduced in chapter 2.3.3 and its quantity is given through equation 2.3.3. It assigns every jet a value depending on its p_t weighted width. Before the comparison of the different periods and the discussion of the analysis it shall be mentioned that there was made a mistake in the analysis. The maximal possible distance in azimuth two objects can have is π. One needs to consider here that this value can easily be exceeded by just taking the difference of two objects φ values., e.g. $|\varphi_1 - \varphi_2| = 4.9\pi - 0.5\pi = 4.4\pi$. In the case the difference d_φ exceeds a value of π, the distance e_φ is calculated to $e_\varphi = 2\pi - d_\varphi$. Unfortunately this was not taken into account during the analysis and instead repeating it once more, a PYTHIA analysis

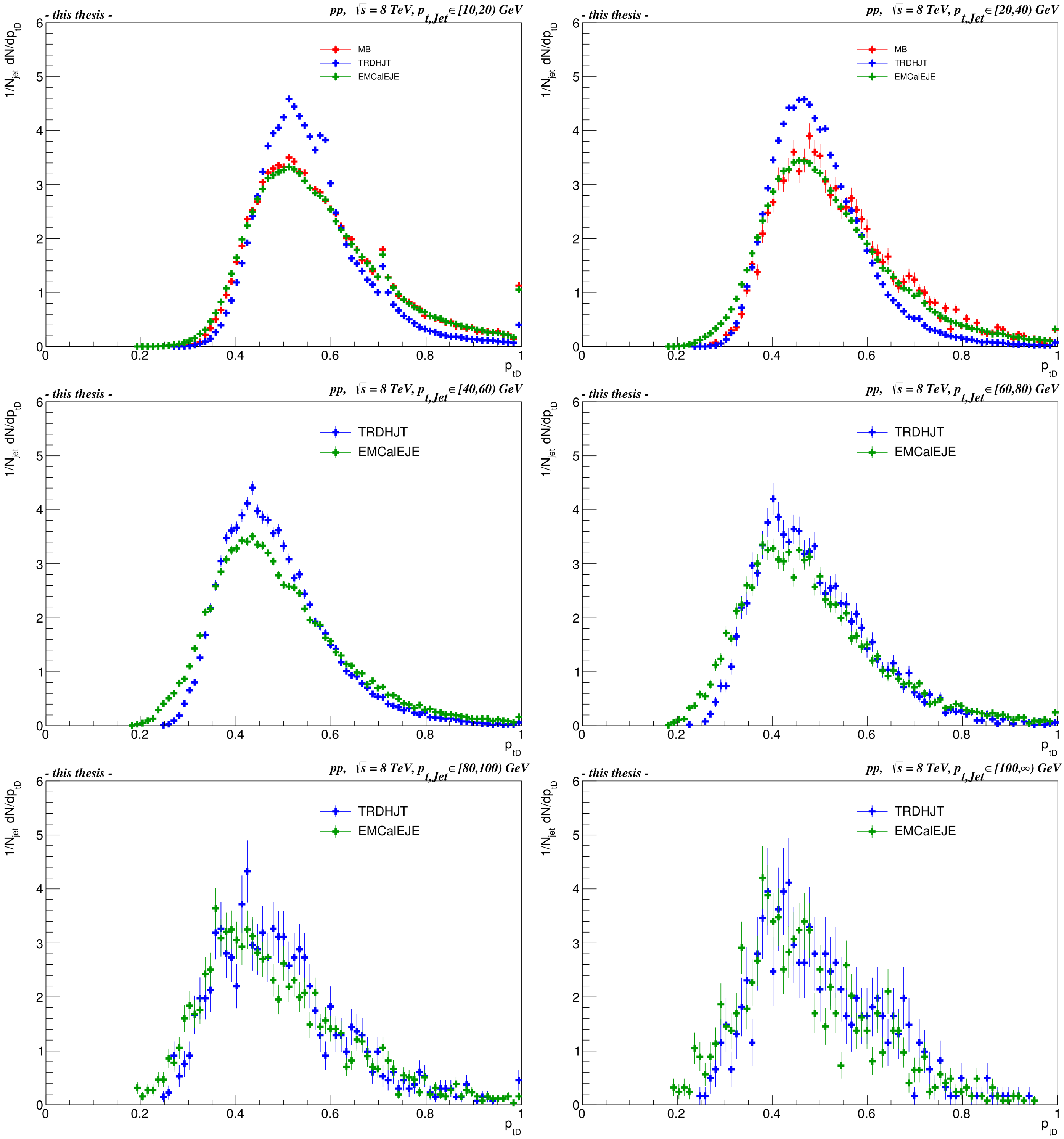

Figure 37: The p_t-dispersion depicted in six p_t-windows for the merged data sets separately for each trigger.

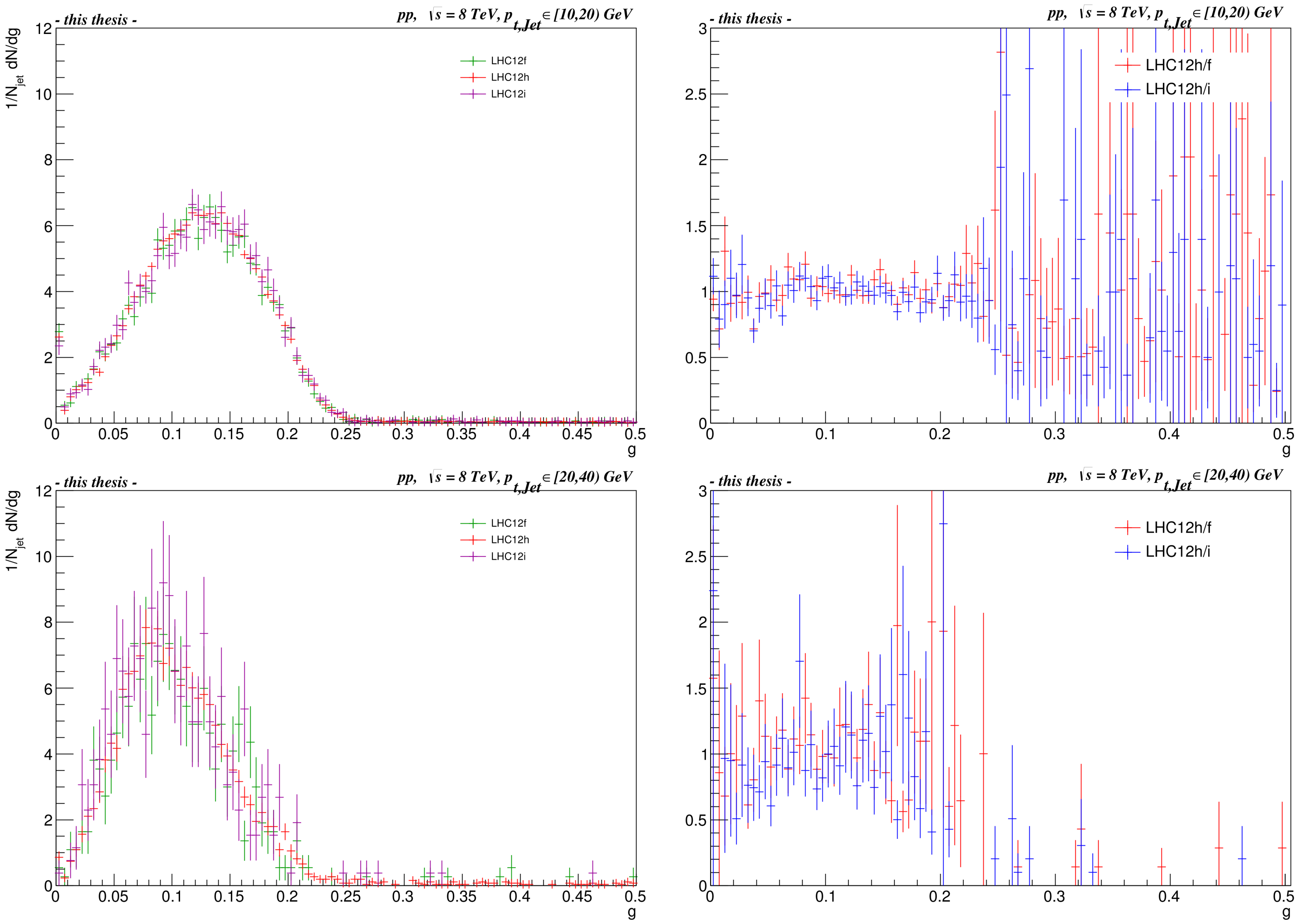

Figure 38: (left) Girth plots resulting MB data, drawn for all three run periods in each of the two p_t-windows. (right) The ratios of the plot from the left between two run periods.

was made to show that this error only has a negligible effect on the analysis. But for now that error will be neglected, the analysis will be discussed as in the chapters before and then in the following chapter the PYTHIA results will be discussed.

Now again the period wise investigation shall be made. In figures 38, 39 and 40 the already well known line-up of plots is presented again. Here, for the MB and TRD triggered data sets, all data coincide very well. The MB data sets again show with increasing p_t-windows an increasing error of the data points. For the EMCal data sets the ratios seem to increase for the LHC12h/LHC12f ratio for a higher girth, but neither the statistic allow a very good estimation on the bias nor the corresponding plots on the right reveal any clear visible bias. So from this point of view one can continue the analysis of the merged data sets.

In figure 41 the trigger wise comparison is splitted in six different p_t-windows is constituted as usual. The girths interval that each window represents is set to [0, 0.5].

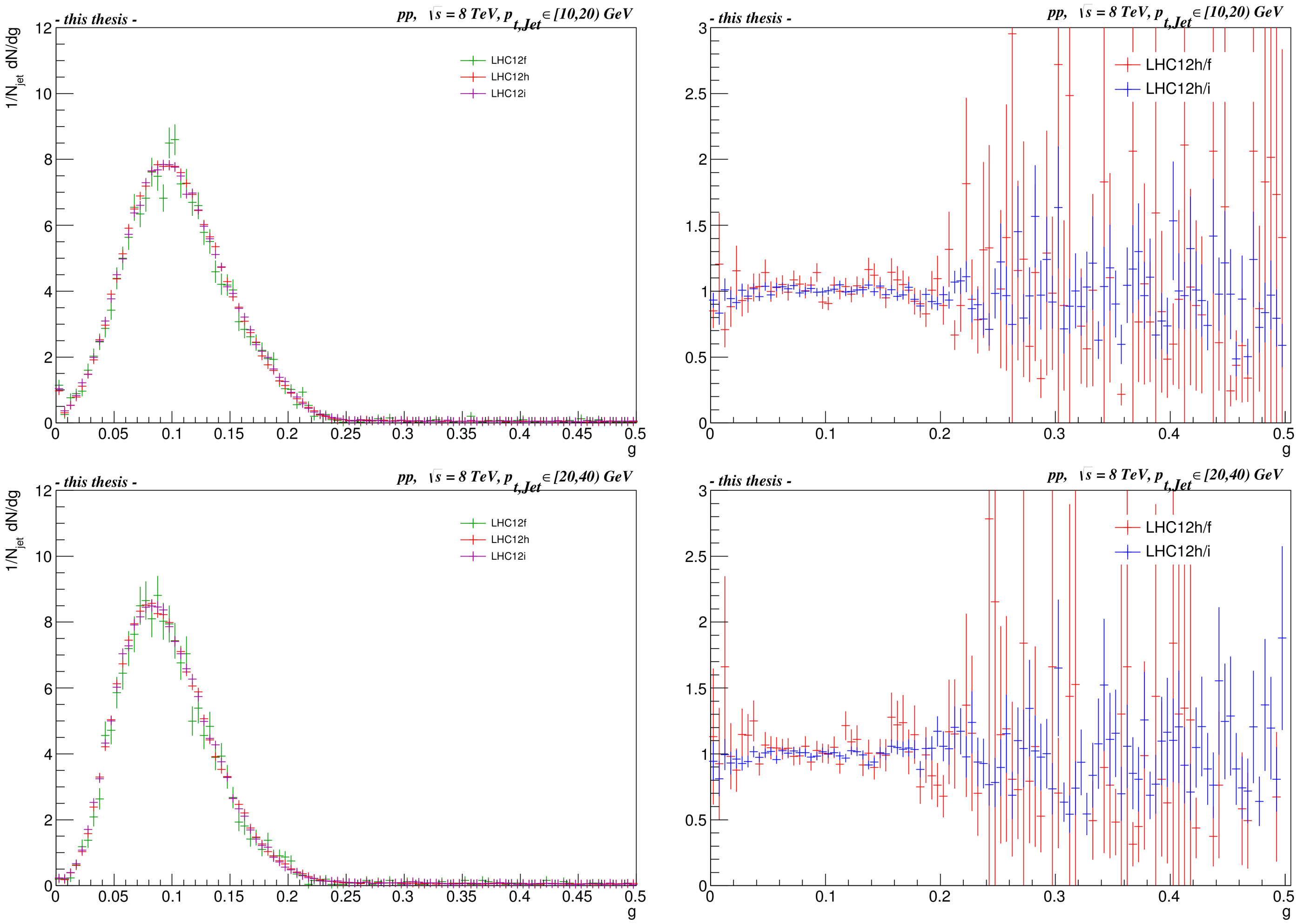

Figure 39: (left) Girth plots resulting TRD data, drawn for all three run periods in each of the two the p_t-windows. (right) The ratios of the plot from the left between two run periods.

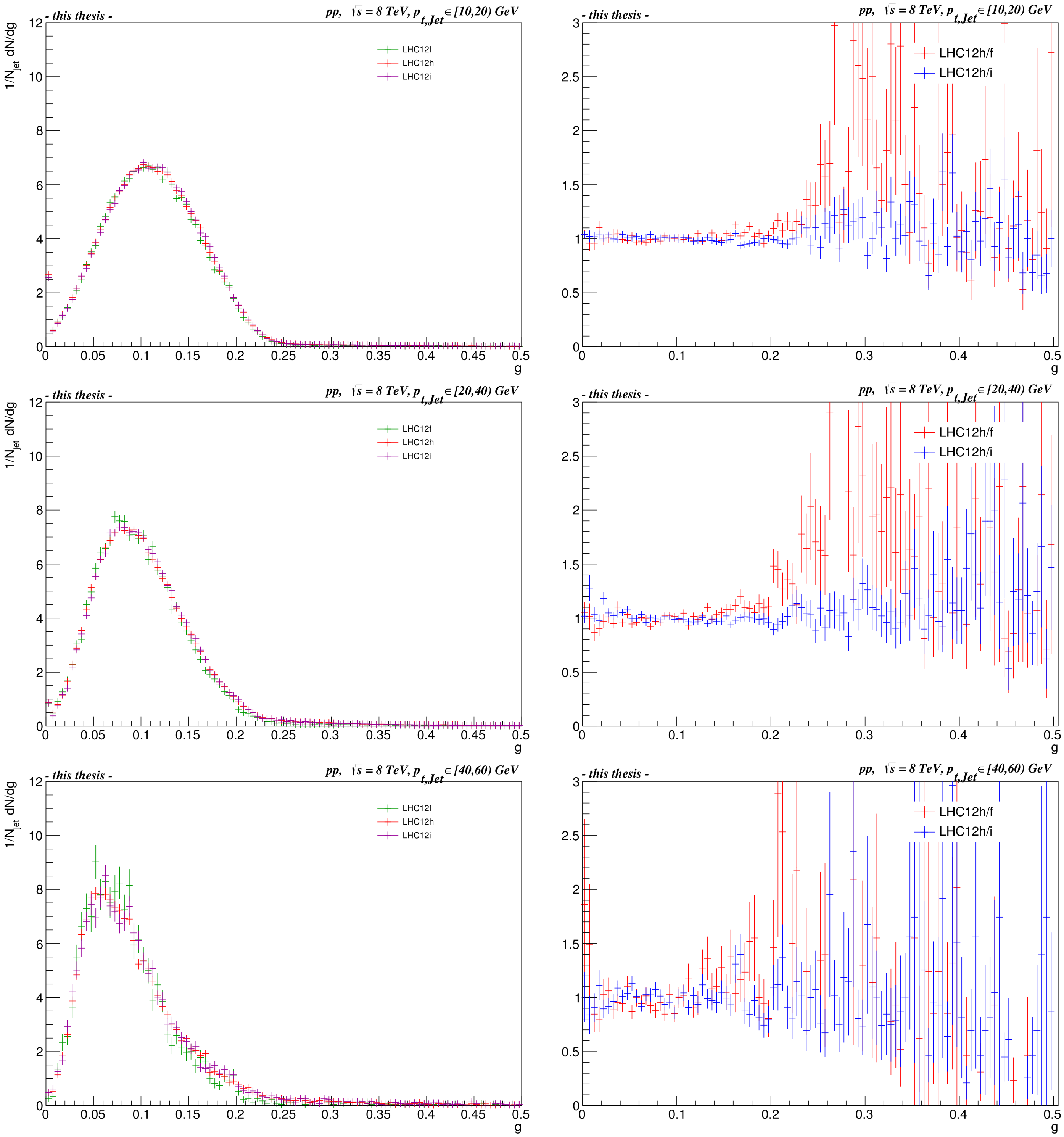

Figure 40: (left) Girth plots resulting EMCal data, drawn for all three run periods separately in each of the three p_t-windows. (right) The ratios of the plot from the right between two run periods.

Though one needs to consider that the girth itself cannot exceed the in the jet-finder algorithm preseted jet radius. This value was set to 0.4. But obviously in the plots exist bins with entries for $g > 0.4$. This is a consequence of the error mentioned at the beginning of this subchapter. Further the plots show a shape that reminds of a Maxwell-Boltzman distribution for each triggered data sample. Next to the maximum one can find an increase in the first bin. Here one can find again all single constituent jets, since the constituents track corresponds to the jet axis. The distance is consequently zero and so its girth too.

An eye on the first plot manifests for all three trigger samples a different maximum. The MB sample shows to have the less collimated jets, whereas the TRD sample has the most collimated ones. The trigger condition for the TRD is due to technical reasons restricted on one stack, which has an area comparetive to a jet of radius $R = 0.2$, where per definition three particles with 3 GeV are located. So HJT triggered jets already carry their main p_t-weight on an area significantly lower than the here analyzed total jet area. This influences the jets girth more the lower its p_t is, since one can expect that particles with a higher p_t are more collimated and the jets are expected to contain more particles for higher $p - t$-jets.

The further comparison between the triggered data samples shows that the shapes are aproaching for increasing jet-p_t. Whereas in the first p_t-window all three shapes differ, in the second one the EMCal and the MB coincide very well. Though one needs to take the rising error into account. For the following p_t-windows there is no comparison with the MB triggered data set possible anymore. For jets with its p_t between 40 GeV and 60 GeV there is a clearly higher maximum for the HJT sample visible, whereas of higher p_t-windows their shapes are according very well but the decreasing statistig makes it impossible to identify any biases.

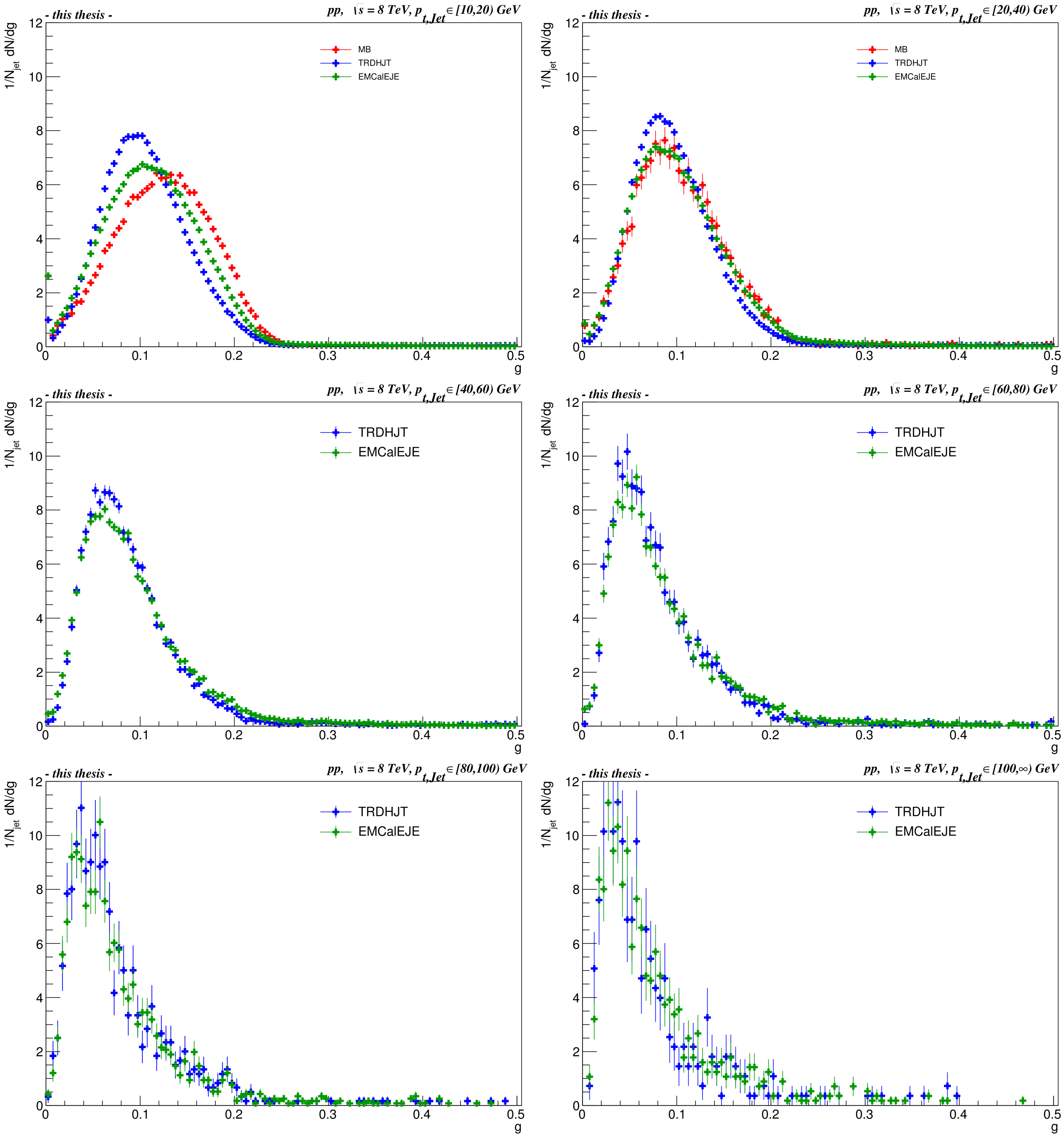

Figure 41: The girth depicted in six p_t-windows for the merged data sets separately for each trigger.

7.4 Experimental data vs. PYTHIA analysis

Finally the experimental data shall be compared with a simple PYTHIA analysis. PYTHIA is an event generator of high energetic collisions [SAC+15] which became a standard tool in particle physic research. PYTHIA first of all helps to interprete data and also enables the study of some detector aspects like accaptance and efficiency. The for this analysis required hard processes that give rise to jets are indicated in PYTHIA as well. In the here shown PYTHIA analysis 8 TeV proton-proton collision corresponding to the collisions of the data sets are simulated. Charged particles exceeding 0.15 GeV and with $|\eta| < 0.9$ are passed to the FastJet jet finder and a jet analysis as described before is made. Considering that in PYTHIA there is no loss of particle tracks due to efficiency problems, particle tracks had been discarded according to the following random principle: a random number z, uniformly distributed with z$\in$ [0,1], was generated with the help of the class TRandom3 for each final particle. The particle tracks then are

$$\text{discarded if} \begin{cases} z > \dfrac{0.4}{0.85} \cdot p_t^{\text{track}} + 0.429 & \text{for } p_t^{\text{track}} < 1\,\text{GeV}. \\ z > 0.9 & \text{for } p_t^{\text{track}} > 1\,\text{GeV}. \end{cases}$$

This simulates a linear increase of the tracking efficiency from 50% to 90% for particles between 0.15 GeV and 1 GeV, and from there on stays constantly by 90%. This simple approximation is based on information corresponding [A+12].

The aim of the PYTHIA analysis is to show the biases introduced by the HJT condition and to investigate the influence of the error made in the girths analysis, see 7.3. In the ideal case the shape of each jet shapes plot corresponds to the already discussed ones in the data analysis part.

To simulate the HJT condition the investigated area was restricted in the η-ϕ-plane by $|\eta| < 0.9$. Then following the design the of the TRD, as given in figure 7, the restricted area was divided in 18 equal sectors in ϕ-direction and once more in 5 equal sectors in η-direction. Each so defined rectangle shall accord to a TRD stacks area and so can be assigned in a way that it corresponds to a TRD-supermodule and stack. Finally the rectangles were discarded which correspond to the missing supermodules or the PHOS-hole. Now if in any of the left rectangles were three particles beyond 3 GeV registered, the HJT condition was set to positive and the in this event reconstructed jets filled plots dedicated to a positive HJT condition for each presented jet shape separately.

In the simulation there were neglected hard scatterings with low momentum transfer. Collisions with a minimum momentum transfer of 8 GeV between two partons were simulated. Possible multiparton interactions during a collision did not influence the observed observables significantly. As well there were probed collisions with an introduced p_t uncertainty due to detector resolutions following [Lip12], but this effect did

not influence the results significantly as well.
Now there shall be compared the results of the PYTHIA analysis with the experimental data by going through the jet shapes and investigating also their behaviour for increasing p_t-windows. For this purpose the results of the PYTHIA simulation is plotted together with the results of the data analysis. Finally four types of data points appear in each plot. The red points correspond to the data of the PYTHIA simulation passing the HJT-condition whose underlying simulation shall mimic the TRDHJTs data represented by the green data points. The blue data points then correspond to the PYTHIA simulations data without any additional condition which shall mimic the MB data. The cyan data points originate from MB data for the p_t windows of jets with [10,20) GeV and [20,40) GeV. Since the statistics rapidly decrease for the MB data for increasing jet-p_t for the windows of jets with [40,60) GeV and [60,80) GeV EMCal triggered data was taken. The EMCal in general corresponds the MB data very well, as it was already discussed, so that this comparision seems to be reasonable. There were some exceptions which in case will be mentioned.

The fragmentation functions plots are shown in figure 42. First a look on the jets with the lowest p_t. The HJT-condition in the PYTHIA simulation causes a remarkable bulge as it was already observed in the analysis of the experimental data, but way stronger. PYTHIA shows especially for the HJT data a way stronger midrange centered profile than all other data samples. A remarkable difference between simulated and experimental data shows up for soft constituents. The shape of the simulated decreases way faster here. Also the knee around ξ=4.2 is not visible anymore. But this is anyway harder to observe due to a smaller fraction of constituents appearing in this region for the PYTHIA data. The same chain of reasoning can be applied here for the single-constituent-jets peak. But that still might occur in the following jet shapes.
For increasing p_t-windows the forms of the jet shape are approaching each other. The bulge caused by the HJT condition is in both cases, for the experimental and simulated data set, at least visible up to the [40-60) GeV window. Then also due to statistics they are not distinctly visible anymore. A final remarkable difference between the experimental and simulated data sample remains. In all p_t-windows the experimental data reveal much more soft constituents. Also, but much more slightly, this seems to occur for very hard constituents. In coherence to this the simulated data shows a higher amount of constituents in the mid-range. Finally the shapes of the triggered and untriggered data sample coincide in the PYTHIA and in the experimental data analysis.

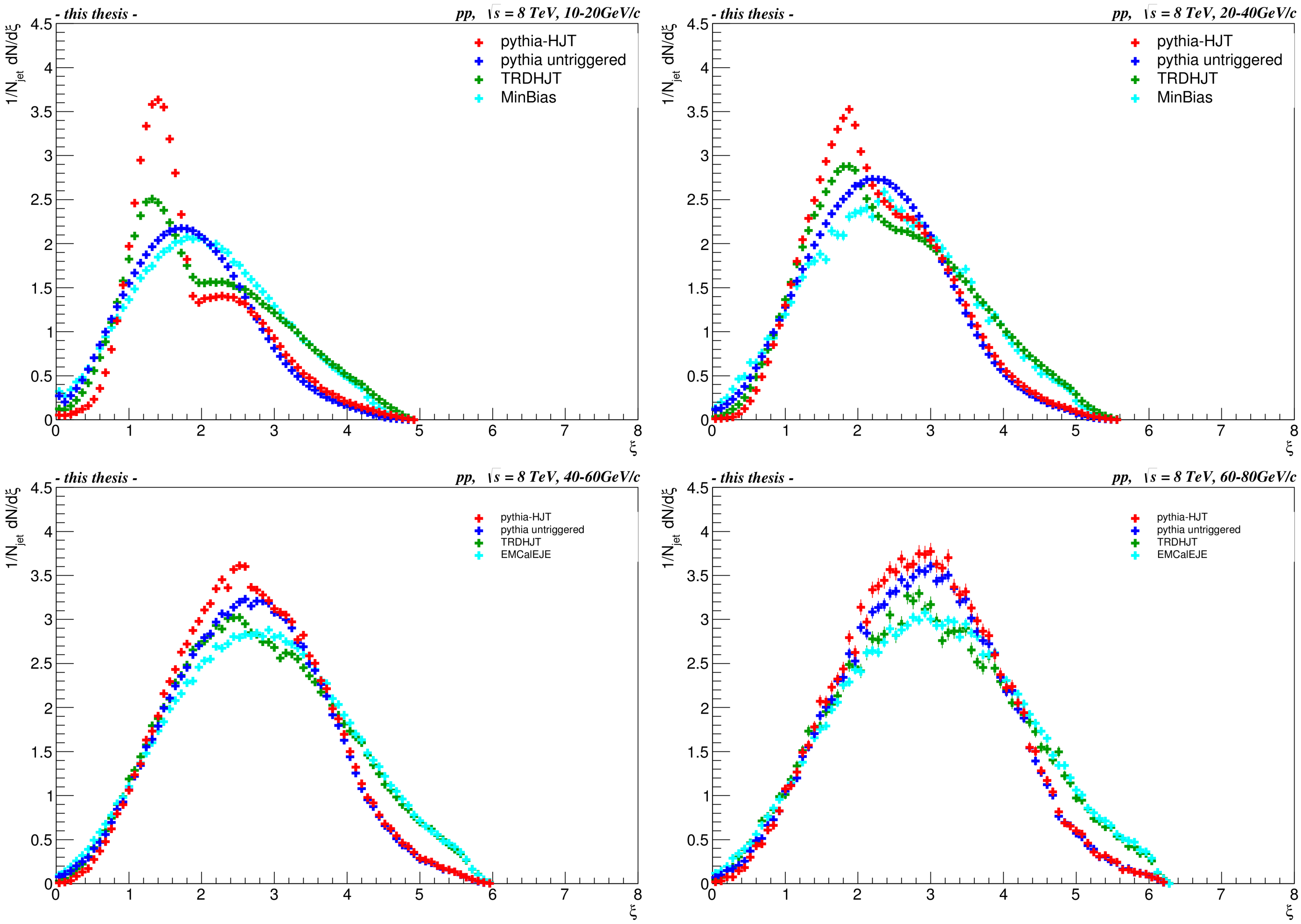

Figure 42: Fragmentatios function plots resulting TRD & MB data and from PYTHIA simulations, untriggered and with HJT condition, drawn for all three run periods in each of the four p_t-windows.

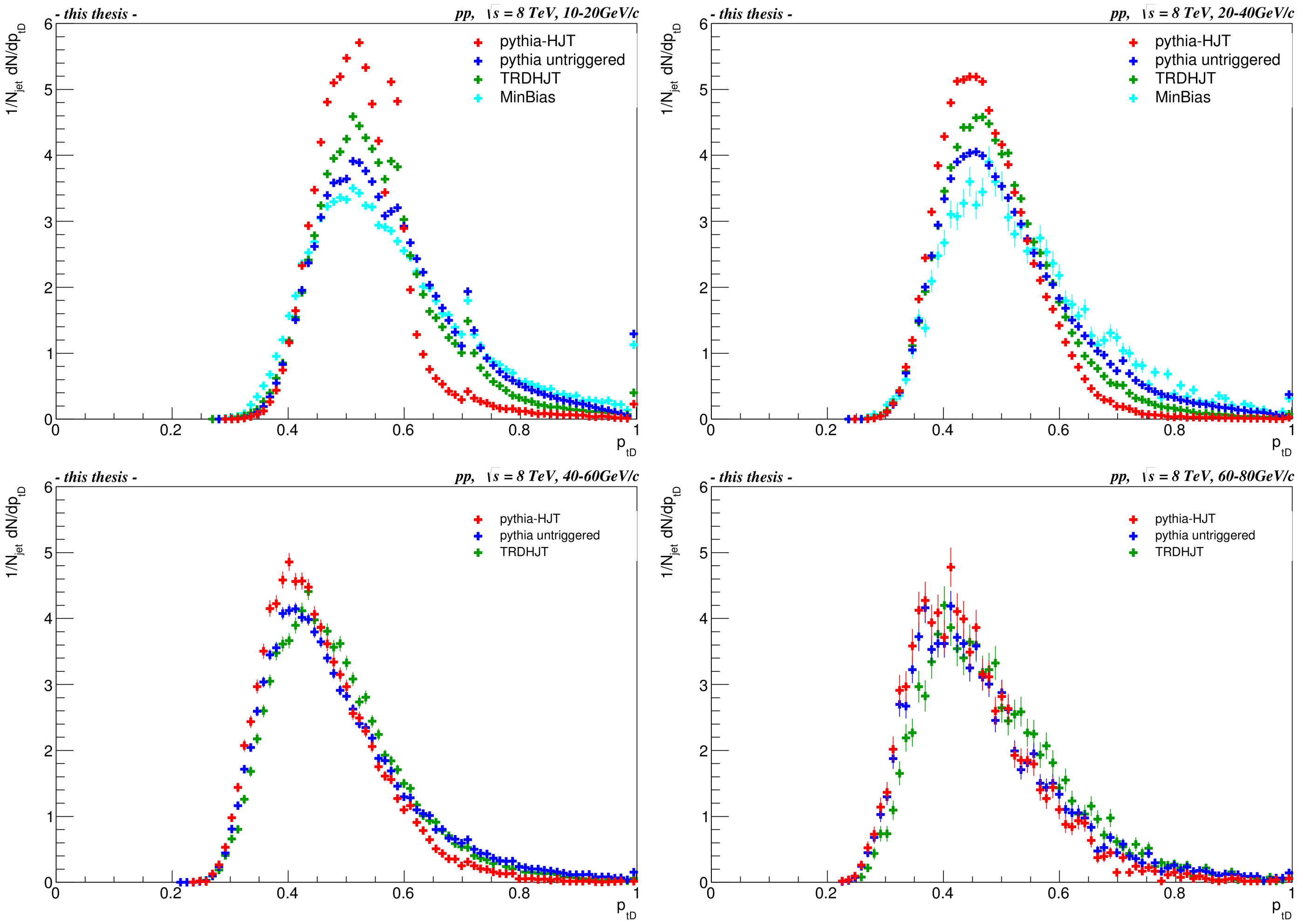

Figure 43: p_t-dispersion plots resulting TRD & MB data and from PYTHIA simulations, untriggered and with HJT condition, drawn for all three run periods in each of the four p_t-windows.

The pt-Dispersions plots are shown in figure 43. Considering the first plot, one can see the previously mentioned characteristical peaks in every of the four graphs, wheras one after another disappears until one cannot see any of them anymore in the last plot. The PYTHIA-HJT simulation shows the strongest maximum, but especially on the flank to higher p_{tD} values it decreases way stronger. The shapes itself approach for increasing jet-p_t. For jets with $\mathrm{p}_t^{\mathrm{jet}} \in [60, 80)$ GeV. The EMCal trigger sample was not plotted here due to mentioned deviations in the very soft area and so does not proof to be a good comparison to the untriggered PYTHIA results.

The Girths plots are shown in figure 44. Thereby was the same mistake applied as in the experimental analysis before and already discussed in chapter 7.3. For the lowest p_t-window the positions of the maxima for the two HJT graphs coincides as

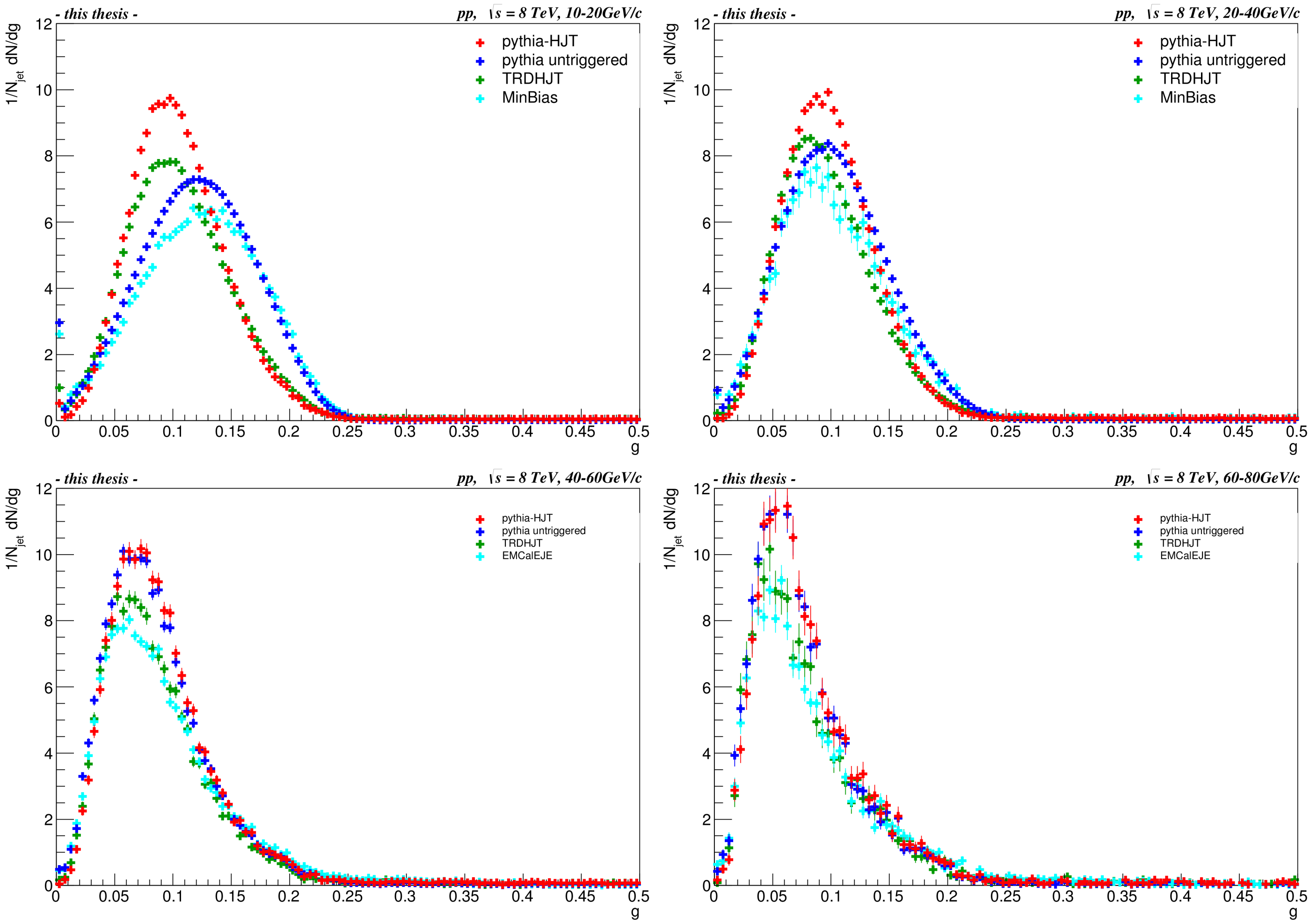

Figure 44: Girth plots resulting TRD & MB data and from PYTHIA simulations, untriggered and with HJT condition, drawn for all three run periods in each of the four p_t-windows.

well as the two MB/untriggered graphs, though that ones originating the PYTHIA analysis are a bit higher. The graphs approch each other for higher jet-p_t until their maximums positions are covering. Finally only the height between the PYTHIA and the experimental data graphs differs. Now there shall be investigated the mentioned mistake that was made and described in chapter 44. For investigation there was set each girth histogram for the untriggered and HJT simulation twice, one containing the committed error and one the correct version. The results are visible in figure 45. For the ratios on each girth-plots left there were always the wrong versions divided by the correct ones. In all p_t-windows the girths data points evolve rather synchronous between the correct and the uncorrect version. One can see clearly that for the region before $g \approx 0.2$ the correct version has less entries wheras afterwards, especially visible in the ratios, the wrong version has much more entries in comparison. All in all since the ratios around the maximum, in all p_t-windows, are pretty constant and so their positions do not move significantly and the position of the maximum delivers the only visible statement for trigger biases, here the conclusion is that the made errors does not change the results significantly and can be neglected.

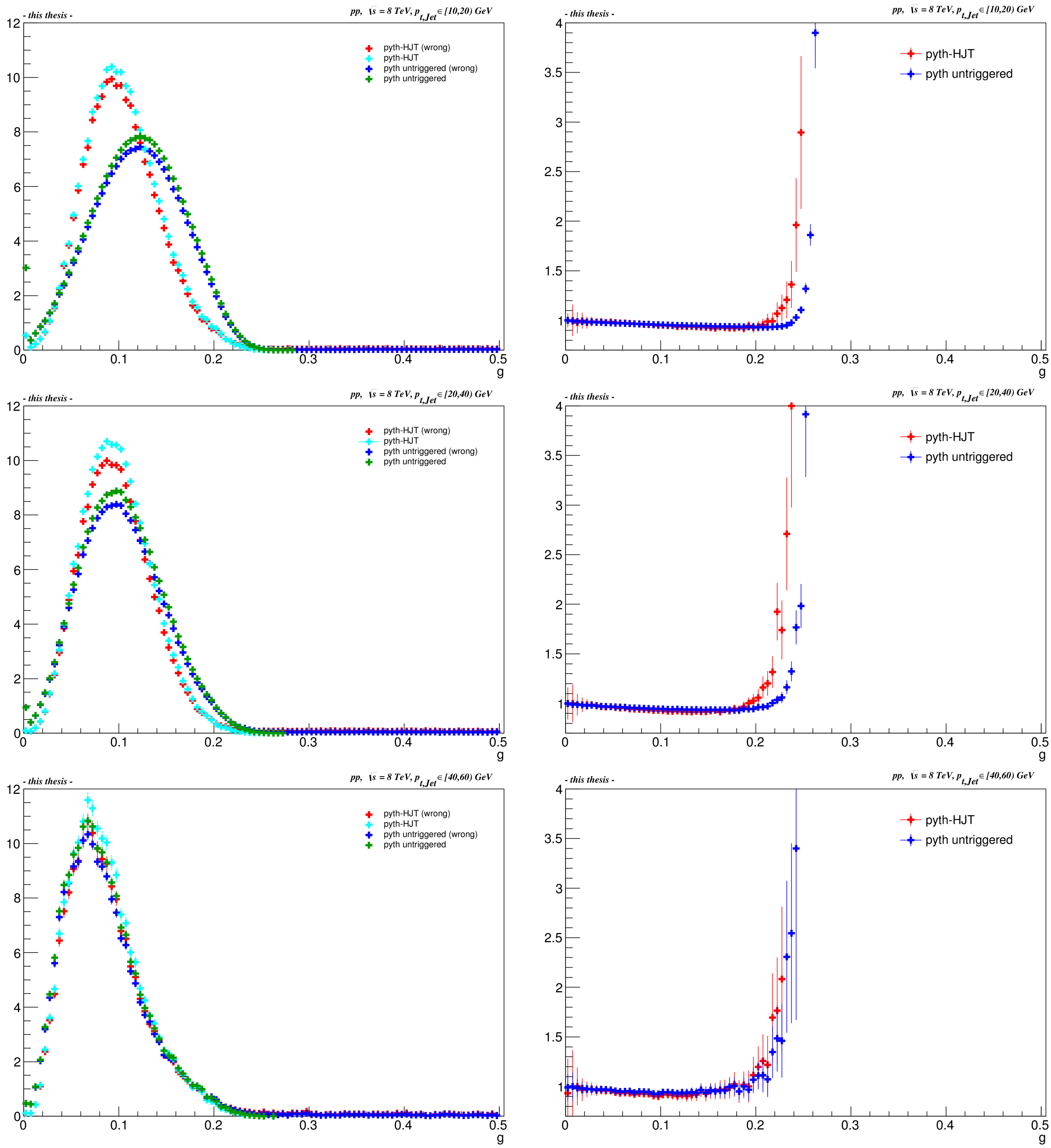

Figure 45: (left) Girth plots originating PYTHIA simulations for untriggered jets and for those fulfiling the HJT condition. Each again was plotted with the correct calculated girth value and again with the wrong calculated girth value as explained. (right) The ratios of the right and the belonging wrong version from the left.

8 Summary, conclusions and outlook

In this thesis there were investigated two important issues in $\sqrt{s} = 8\,\text{TeV}$ proton-proton collisions, biases on three different jet shapes through trigger conditions and the rejections factor for three trigger combinations. The underlying data origins the LHC12f, LHC12h and LHC12i run periods. The rejection factor R_F is a quantity on how much more efficient a chosen trigger is than in comparison to another one. Thereby one can expect that with the increase of the transversal momentum R_F increases and finally reaches a plateau, so the theory. In this thesis there were calculated and plotted rejection factors between three samples of trigger classes, the TRD, the EMCal and the MB sample. To investigate errors through measurements the results for the rejection factor were first investigated for each run period separately. In figure 21 the results are summed up. Though through the experimental set-up the R_F should agree within their mistakes. But the final results reveal large differences between the run periods with the largest R_F and that one with the lowest R_F. But therefore it is also necessary to consider that the interval boundaries for the straight line fits to the hypothetical plateau were set differently due to the applied method of setting the lower interval boundary. Following figure 15 this is not a big suprise, since the here simulated trigger efficiencies of the HJT increases up to 60-80 GeV, so consequently there is an increase in the rejection factor with increasing lower interval boundary for the fit. For the EMCal/MB-R_F there occurs a similar behaviour. But in any case, for the TRD/MB-R_F and for EMCal/MB-R_F for a good comparison between the run periods and a reasonable fit to the hypothetical plateau there is more data required. A distinct plateau is in none of the both cases visible which is finally also a result of the large underlying error of the data points.

The TRD as well as the EMCal record more data in the high p_t-region, so a comparison here seems senseful. A plateau here is good visible, cf. 24. Also the rejection factor values for the LHC12h and for the LHC12i run are pretty close and only differ by a factor of about 1.05, though the R_F-values do not agree within their errors, the results seem to agree. The LHCf runs rejection is a bit lower. But the ratios of figure 19 already show an unexpected dip in the ratio for the LHCf compared to the LHC12h of the TRD triggered data sample. So from that point of view a lower R_F is not surprising, also the lower interval boundary is set to 50 GeV for the LHC12f instead to 25-30 GeV.

For the sake of completeness all three runperiods had been merged and the rejection factor was calculated for the three merged data sets. The according plots are presented in figure 25. The lower interval boundary this time was set to 60 GeV corresponding the earliest possible beginning of the expected plateau following figure 15. For the TRD/MB and EMCal/MB rejection factor the straight line fit to the plateau reveals

as rather uncertain due to the large errors of the referring data point. This is as well confirmed by the low χ^2/NDF-values. The other way arround it appears for the TRD/EMCal rejection factor. Here a plateau is good visible, but the high χ^2/NDF-value reveals a bad fit assumption or an underestimated error. The latter one indeed should be taken strongly in consideration, since the ratios of the p_t-spectra between the run periods revealed repeatedetly deviations and only statistical errors were here regarded. All in all the the TRDHJT proved to trigger jets exceeding 60 GeV about 2500 times more efficiently than the MB, whereas the EMCal did it about 1900 time more efficiently.
For further investigations the rejection factor is a crucial quantity when it comes to cross sections σ and luminosities L. The number of recorded events by the minimum bias $N^{\mathrm{MB}}_{\mathrm{events}}$ is given to

$$N^{\mathrm{events}}_{\mathrm{MB}} = L \cdot \sigma_{\mathrm{MB}}. \tag{8.0.1}$$

Here the MB indexed quantities refer to the same trigger and L is the bunch luminosity. Now considering that for example the TRD/MB-rejection factor gives how much more events the TRD records in comparison to the MB one receives

$$\underbrace{N^{\mathrm{events}}_{\mathrm{MB}} R_F}_{=N^{\mathrm{events}}_{\mathrm{TRD}}} = L \cdot \underbrace{\sigma_{\mathrm{MB}} R_F}_{=\sigma_{\mathrm{TRD}}}. \tag{8.0.2}$$

The second main issue, the jet shapes, was analysed in chapter 7. The aim of the shape analysis was to investigate biases caused through the HJT in particular and to estimate a p_t-region from where on the shapes show unbiased forms. As primary tool there was used the comparison to unbiased data. The unbiased data was represented by the MB data set for the low p_T-region, and from a jet-p_t of 40 GeV on there was used the EMCal data set, which jet shapes results proved mostly to be unbiased in comparison to the MB ones.
The HJT condition thereby causes derivations from the unbiased shapes. The most eyecatching relict was the bulge that appeared on the fragmentation function shapes. Another one was the stronger peak for jets with three particles of the same p_t showing up in the p_t-dispersion. Apart from this a deforming of the else normal form of the shapes can also be observed. Further for the fragmentation function there can be observed a drop for hard constituents, since there are constituents-p_t–jet-p_t–connections that are categorially excluded. The other two jet shapes are normalized so that their integral is consequently one. So a relict in one region causes automatically a drop for the rest of the shape. So reveals the p_t-dispersion a more narrow peak pointing to HJT-jets in the mid-range in favour of very low or hard jets. The bias on the girth

only reveals a shift and narrower maximum for the TRD compared to the other two and points on more collimated jets. This is a consequence of the restriction of the HJT condition on one stack which corresponds approximately to a jet of a cone radius of $R_{cone} = 0.2$.

A similar influence through the HJT was shown in the here discribed PYTHIA simulation. Though the forms of the shapes of the data analysis differ from the simulated ones, also when viewing on the unbiased and triggered data sets separately. But finally the same relicts and deformations appeared on the shapes for the simulated HJT, though in the simulation the biases are more distinctive.

All the discussed biases disappear with increasing jet-p_t. The trigger conditions so seem to become part of the jet. In the jet-p_t-window of 40-60 GeV the biases are still clearly visible whereas in the following jet-p_t-window of 60-80 Gev jets they are hardly visible. Unfortunately increasing errors begin to hamper the identification of biases as well. For further jet-p_t there are no biases visible anymore, but finally the errors are already too large to locate trigger biases as slight as in the two windows before.

But anyway the disappearing of the biases seems to agree with the expected trigger efficiency as it was depicted in figure 15. As a result one can say that the trigger biases tend to disappear for a jet-$p_t > 80$ GeV. More confident statements are desireable but for this purpose more data is required.

Anyway as it was written in the first chapter of this thesis, the jet shapes are an excellent indicator for the quark-gluon plasma due to jet quenching, if applied to heavy-ion collisions. But this should influence the unbiased shapes as well as the from triggered data received shapes. It first of all is important for the jet theories to attain jet shapes detached from any influence through experimental issues .

A run numbers

run numbers LHC12f

186668 186689 186690 186692 186694 186811 186814 186937 186938 186939
186966 186969 186990 186992 186994 187143 187145 187146 187147 187148
187149 187150 187151 187152 187202 187203 187339 187340 187341 187343
187487 187488 187489 187510 187623 187624 187627 187656 187698 187739
187749 187783 187785 187791 187796 188093 188101

run numbers LHC12h

189122 189146 189147 189183 189228 189229 189231 189306 189310 189315
189316 189350 189351 189352 189353 189397 189400 189407 189409 189410
189411 189473 189474 189522 189523 189526 189577 189578 189602 189603
189605 189610 189611 189612 189616 189621 189623 189647 189648 189650
189654 189656 189658 189659 189696 189697 189698 189734 189735 189736
189737 190150 190209 190210 190212 190213 190214 190215 190216 190240
190303 190305 190307 190335 190337 190338 190340 190341 190342 190344
190386 190388 190389 190390 190392 190393 190416 190417 190418 190419
190421 190422 190424 190425 190895 190898 190903 190904 190968 190970
190974 190975 190979 190981 190983 190984 191129 191227 191229 191230
191231 191232 191234 191242 191244 191245 191247 191248 191450 191451
192004 192072 192073 192075 192095 192128 192136 192140 192141 192172
192174 192177 192194 192197 192199 192200 192201 192202 192205 192246
192344 192415 192417 192453 192461 192468 192471 192492 192499 192505
192510 192535 192542 192548 192551 192732

run numbers LHC12i

192772 192775 192778 192779 192820 192822 192824 193004 193005 193007
193008 193010 193011 193014 193047 193049 193051 193092 193093 193094
193148 193150 193151 193152 193155 193156 193184 193187 193188 193189
193192 193194

B Acronyms & References

ADC Analog Digital Converter

AOD Analysis Object Data

ALICE A Large Ion Collider Experiment

ATLAS A Torodial LHC Apparatus

BC Bunch Crossing Mask

CERN European Organization for Nuclear Research

CMS Compact Muon Solenoid

CTP Central Trigger Processor

DAQ Data Aquisition

ESD Event Summary Data

EJE EMCal Jet Trigger

GTU Global Trigger Unit

HJT High Jet Trigger

LHC Large Hadron Collider

LHCb Large Hadron Collider beauty

LTU Local Trigger Unit

MB Minum Bias

MCM Multi Chip Modul

ORI Optical Readout Interface

PASA Pre Amplifier and Shaper Amplifier

QCD Quantum Chormodynamics

QGP Quark-Gluon Plasma

SM Standard Model

TPC Time Projection Chamber

TRAP Tracklet Processor

TRD Transition Radiation Detector

WU Wake Up

References

[A^+12] Betty Abelev et al. Measurement of Event Background Fluctuations for Charged Particle Jet Reconstruction in Pb-Pb collisions at $\sqrt{s_{NN}} = 2.76$ TeV. *JHEP*, 03:053, 2012.

[A^+14] Betty Bezverkhny Abelev et al. Performance of the ALICE Experiment at the CERN LHC. *Int. J. Mod. Phys.*, A29:1430044, 2014.

[A^+18] Shreyasi Acharya et al. The ALICE Transition Radiation Detector: construction, operation, and performance. *Nucl. Instrum. Meth.*, A881:88–127, 2018.

[Bat12] Bastian Bathen. *Jet Measurements and Reconstruction Biases in Proton–Proton and Pb–Pb Collisions with ALICE at the LHC*. PhD thesis, Westfälische Wilhelms-Universität Münster, 2012.

[Bea04] Bearden et al. Nuclear Stopping in Au+Au Collisions at ($\sqrt{s_{NN}} = 200\,\mathrm{GeV}$. *Physical Review Letters*, 93(10):102301, August 2004.

[BEJ^+10] A. Bhasin, D. Evans, G. T. Jones, P. Jovanović, A. Jusko, R. Kour, M. Krivda, C. Lazzeroni, R. Lietava, Z. L. Matthews, S. Navin, R. J. Platt, H. Snow, J. D. Tapia Takaki, O. Villalobos Baillie, and for the ALICE collaboration. Minimum bias trigger for pp physics with alice. *Indian Journal of Physics*, 84(12):1733–1738, Dec 2010.

[Cac] Matteo et al. Cacciari. *http://inspirehep.net/record/779080/plots*. accessed: 2018-03-27.

[CNRS17] M. Connors, C. Nattrass, R. Reed, and S. Salur. Review of Jet Measurements in Heavy Ion Collisions. *ArXiv e-prints*, May 2017.

[ea08] The ALICE Collaboration et al. The alice experiment at the cern lhc. *Journal of Instrumentation*, 3(08):S08002, 2008.

[Gri10] David Griffiths. *Introduction to Elementary Particles*. WILEY-VCH Verlag GmbH & Co. KGaA, Weinheim, 2010.

[Kle13] Jochen Klein. Triggering with the ALICE TRD. *Nucl. Instrum. Meth.*, A706:23–28, 2013.

[Kle14] Jochen Klein. *Jet Physics with A Large Ion Collider Experiment at the Large Hadron Collider*. PhD thesis, Combined Faculties for the Natural Science and for Mathematics of the Ruperto-Carola University of Heidelberg, 2014.

[Lip12] Christian Lippmann. Performance of the ALICE Time Projection Chamber. *Physics Procedia*, 37:434–441, 2012.

[Man12] Vito Manzari. ITS Schematics. General Photo, December 2012.

[Mou14] Philippe Mouche. Overall view of the LHC. Vue d'ensemble du LHC. Jun 2014. General Photo.

[PŠ17] R. Pasechnik and M. Šumbera. Phenomenological Review on Quark-Gluon Plasma: Concepts vs. Observations. *Universe*, 3:7, January 2017.

[SAC+15] Torbjörn Sjöstrand, Stefan Ask, Jesper R. Christiansen, Richard Corke, Nishita Desai, Philip Ilten, Stephen Mrenna, Stefan Prestel, Christine O. Rasmussen, and Peter Z. Skands. An Introduction to PYTHIA 8.2. *Comput. Phys. Commun.*, 191:159–177, 2015.

[Sle95] Sander Slegt. *Space-time evolution in relavistic heavy-ion collissions*. PhD thesis, 1995. date_submitted:1995 Rights: University of Groningen.

[Tau17] Arturo Tauro. ALICE Schematics. General Photo, May 2017.

[Teaa] ALICE Team. *https://twiki.cern.ch/twiki/bin/view/Main/QA:ChargedTracks*. accessed: 2018-10-17.

[Teab] CERN Team. *https://indico.cern.ch/event/246374/contributions/542902/attachments/422980/587265/Roman.pdf*. accessed: 2018-10-17.

[Teac] CERN Team. *https://root.cern.ch/*. accessed: 2018-06-05.

[Tiw] Swatantra Kumari Tiwari. *https://www.researchgate.net/figure/A-schematic-diagram-of-space-time-evolution-of-ultrarelativistic-heavy-ion-collisions_fig14_237842993*. Indian Institute of Technology Indore. accessed: 2018-06-05.

[Won94] Cheuk-Yin Wong. *Introduction to High-Energy Heavy-Ion Collisions*. World Scientific Publishing Co. Pte. Ltd., 1994.

[YHM05] Kohsuke Yagi, Tetsuo Hatsuda, and Yasuo Miake. *Quark-Gluon Plasma*. Cambridge University Press, 2005.

Schlusserklärung

Ich versichere, dass ich die vorliegende Masterarbeit über "Jet Measurements at the LHC with the TRD-Trigger in ALICE" selbstständig verfasst habe und keine anderen als die angegebenen Quellen und Hilfsmittel benutzt habe. Alle Stellen der Arbeit, die anderen Werken dem Wortlaut oder Sinn nach entnommen wurden, habe ich in jedem Fall unter Angabe der Quelle als Entlehnung kenntlich gemacht. Das Gleiche gilt auch für die Zeichnungen, Grafiken und Abbildungen.

Münster, den 20.12.2018

(Christopher Rittmeier)

Ich erkläre mich mit einem Abgleich der Arbeit mit anderen Texten zwecks Auffindung von Übereinstimmungen sowie mit einer zu diesem Zweck vorzunehmenden Speicherung der Arbeit in einer Datenbank einverstanden.

Münster, den 20.12.2018

(Christopher Rittmeier)